Sorbent Nanotechnologies for Water Cleaning

A Dissertation

SUBMITTED TO THE FACULTY OF
UNIVERSITY OF MINNESOTA
BY

Snober Ahmed

IN PARTIAL FULFILLMENT OF THE REQUIREMENTS

FOR THE DEGREE OF

DOCTOR OF PHILOSOPHY

Advisor: Dr. Abdennour Abbas

July 2017

Acknowledgements

I would like to express the gratitude to my advisor, Dr. Abdennour Abbas, for his guidance, constructive criticism, untiring help, moral support and enlightened supervision. I would also like to take this opportunity to thank my committee members Dr. Jonathan Schilling, Dr. William Tai Yin Tze and Dr. Devi Patnayak for sharing their valuable experience in their respective fields.

Funding for the projects was provided by grants from the MnDrive Global Food Ventures, the Midwest Dairy Association as well as the generous support of the Schwan Food Company's fellowship.

I owe a great debt to my lab fellows John Brockgreitens, Ke Xu (a.k.a. cookie), Yan Wu, Renu Singh, Fatemeh Haidary and Phoung Bui for their friendly and helpful behavior. Thanks to Lucas Stolp for being there for innumerable times when I needed advice on safety issues and for smooth installation of various equipment☺. Coming to the U of M had been a great unforgettable experience, which not only gave me tremendous opportunities to excel in my career but also connect with great friends like Nu Wang, John Brockgreitens and Tabinda Hassan.

A special thanks to all the staff members especially Lisa. K. Wiley who has always been there to extend her support and help whenever needed.

Humans have the power to express their feelings but there are some emotions where words always fall short. I would like to thank my parents (Jamil Ahmad & Rehana Jamil) for their unlimited efforts for my well-being and siblings especially Rameez Ahmad who has always been there to help me. In addition to this, very dear friends of mine in Pakistan (esp. Mehwish) who never made me feel like I was alone here and showed their constant support, patience and love.

Dedication

I dedicate this the dissertation to my parents and my late grandmother (whom I lost over that journey)

Abstract

Despite decades of regulatory efforts to mitigate water pollution, many chemicals, particularly heavy metals, still present risks to human health. In addition to direct exposure, certain metals such as mercury threaten public health due to its persistence, bioaccumulation and bioamplification throughout the food chain. A number of U.S. Federal and State regulations have been established to reduce the levels of mercury in water. The Great Lakes Initiative (GLI) requires wastewater dischargers in the Lake Superior basin to meet a mercury water quality standard of 1.3 ng/L, while the rest of Minnesota lakes have a chronic standard of 6.9 ng/L.

Activated carbon (AC) has been widely explored for the removal of mercury. However, AC suffers from many limitations inherent to its chemical properties, and it becomes increasingly challenging to meet current and future regulations by simply modifying AC to enhance its performance. Such limitations include pH dependent sorption, background ion interference and re-emission of the captured pollutants. Novel sorbent materials with higher affinity and chemical specificity would overcome these limitations. Recently, the performance of nanosorbents have been studied in order to removal pollutants. Nanosorbents utilize the ultra-high reactive surface of nanoparticles for rapid, effective and even permanent sequestration of heavy metals from water and air, thus showed promising results as compared to AC.

The goal of this thesis research is to develop nanomaterial-based sorbents for the removal of mercury from water. It describes the development of a new solid support-assisted growth of selenium nanoparticles, their use for water remediation, and the development of a new nanoselenium-based sorbent sponge for fast and efficient mercury removal. The nanoselenium sorbent not only shows irreversible interaction with mercury but also exhibits remarkable properties by overcoming the

limitations of activated carbon. The nanoselenium sponge was shown to remove mercury to undetectable levels within one minute. This new sponge technology would have an impact on inspiring new stringent regulations and lowering costs as compared to AC to help industries meet regulatory requirements, which will ultimately help improve air and water quality, aquatic life and public health.

Table of Contents

List of Tables

List of Figures

Chapter 1: Introduction

1.1 Water pollution

Clean water is one of the vital elements for the sustainability of life. According to a report, globally one in three people are unable to meet their daily needs for water. The problem of having sufficient clean water is even getting bigger as the population is growing (Tansel, 2008). Based on the availability and quality, currently only 1% of water is available to fulfill human consumption around the world (Grey et al., 2013). Besides the domestic use, the increase in industrial and agricultural activities has not only depleted the resource but has also introduced additional problems, including global pollution (Richard Helmer, 1997). Water has been contaminated with heavy metal pollutants such as mercury, lead and arsenic, as well as synthetic organic and pharmaceutical wastes such as pesticides and antibiotics (Rossner et al., 2009). All these pollutants, especially heavy metals, have been found to pose a significant risk to human health (Bolong et al., 2009; Järup, 2003).

It has been a challenge for researchers all over the world to solve this problem. Over the last decade, different techniques such as filtration, flocculation, chemical and biological treatments have been introduced to clean water. But they have not shown promising futures because of certain limitations such as their inefficiency in completely removing pollutants, their cost and the long times needed for cleanup (Adeleye et al., 2016). Absorbent materials such as activated carbon have been successfully used over many years for cleaning water. Although these materials have been able to overcome the problems posed by conventional methods, they still have certain shortcomings, which will be discussed in other sections (Bhatnagar and

Sillanpää, 2011; Crini, 2005). Nanotechnology is one of the growing areas in which researchers are working to improve the performance of absorbent-based materials.

1.2 Application of Nanomaterials in Water Remediation

Nanotechnology has attracted researchers all over the world because of extensive applications of nanomaterials in the various fields of science. Materials that have at least one dimension in range of 1-100 nm ($1nm=10^{-9}$ m) are referred as nanomaterials, these include nanoparticles, nanofilms and nanowires (Sanchez and Sobolev, 2010). Among these applications, the use of nanotechnology in the environmental field has become very important. It ranges from developing nanotechnology-based sensors for environmental contaminants to facilitating environmental remediation of toxic pollutants (Ariga et al., 2012). For the past decade, researchers have been using metal nanoparticles such as iron to remove organic waste solvents. Particularly, zero valent iron nanoparticles have been shown to transform the contaminant tetrachloroethylene to an environment friendly form (Zhang, 2003). Iron nanoparticles have also shown to possess reducing properties. This property has been explored by the researchers to convert harmful organic and inorganic pollutants to less toxic chemical forms by a reduction process (Nam and Tratnyek, 2000; Orth and Gillham, 1996; Siantar et al., 1996). Iron nanoparticles showed promising results but the inability to recover the particles from the water was the major hurdle to its success.

Carbon-based nanomaterials are another class of nanomaterials that have been widely studied for their use in environmental remediation. In general, these nanomaterials include carbon nanotubes and graphene. Carbon nanotubes and graphene oxide have been shown to successfully remove Zn^{+2}, Cu^{+2}, Pb^{+2} and Cd^{+2} from water (Lu et al., 2006; Lu et al., 2008; Lu and Su, 2007). The main problem with

these nanomaterials is the cost and pH dependent efficiency. Other nanoparticles that have been used to remove heavy metals include cupric oxide, alumina, zinc oxide and titanium dioxide (Lata and Samadder, 2016).

Scientists are actively trying to develop solutions for oil spills and nuclear wastes. In a recent study, amphiphilic amino acids were used to clean oil spills in oceans. The solution becomes a gel upon contact with oil and hence provides more ease in cleaning (Mukherjee et al., 2014). Similarly, some studies have been proposed to overcome nuclear plant accidents using nanotechnology based approaches and different materials have been shown to capture radioactive elements such as uranium, strontium and plutonium (Griffith and Luca, 2004; Veeck et al., 2004).

Over the past 20 years, a new class of nanomaterial called metal organic frameworks (MOFs) has been introduced. Briefly, they are composed of metal ions arranged in a framework by the crosslinking organic linkers (Qiu et al., 2014). Their adaptable pore size, high porosity and ease of using various ligands has attracted researchers to explore them for environmental remediation. Reports showed that, MOFs can be used for the catalysis of reactions and also for the adsorption of pollutants from gaseous phase (Ma et al., 2005; Suh et al., 2012).

To increase the number of available adsorption sites and enhance the loading capacity of mercury, many research groups converge towards the use of nanomaterials such as graphene-based composites (Kabiri et al., 2015), mesoporous organosilica adsorbents (Walcarius and Mercier, 2010), silica–titania composites (Byrne and Mazyck, 2009) and functionalized metal organic frameworks (MOFs) (Li et al., 2014; Liu et al., 2014; Yee et al., 2013). Although some recently developed sulfur-functionalized MOFs can reach a removal rate up to 99.997% bringing mercury levels down from 10 ppm to 0.4 ppb (Li et al., 2014), the high cost of the material and the

long contact time needed for mercury removal (6-12 hours under stirring conditions) present serious limitations for large scale implementation.

1.3 The Mercury Problem

The urgent need for cost-effective and sustainable mercury removal solutions is clearly justified by the growing global threat that mercury ca es to human health and the environment. In Minnesota alone, two thirds of the waters on Minnesota's 2004 Impaired Waters List are impaired because of mercury contamination that ranges from 0.27 to 12.43 ng/L (the U.S.-EPA limit is 2 ng/L) (Monson and Heiskary, 2008). Mercury contamination of waters results in mercury accumulation in fish and along the food chain, thus representing a serious health risk and food security issue. Annually, mercury deposition and concentration in Food and Agriculture Organization (FAO) fishing areas is depicted in the **Figure 1**. As shown in the figure, Northwest Pacific has both the highest fish production and mercury deposition. Thus the consumption of fish mainly from these areas increases the risk of health issues.In

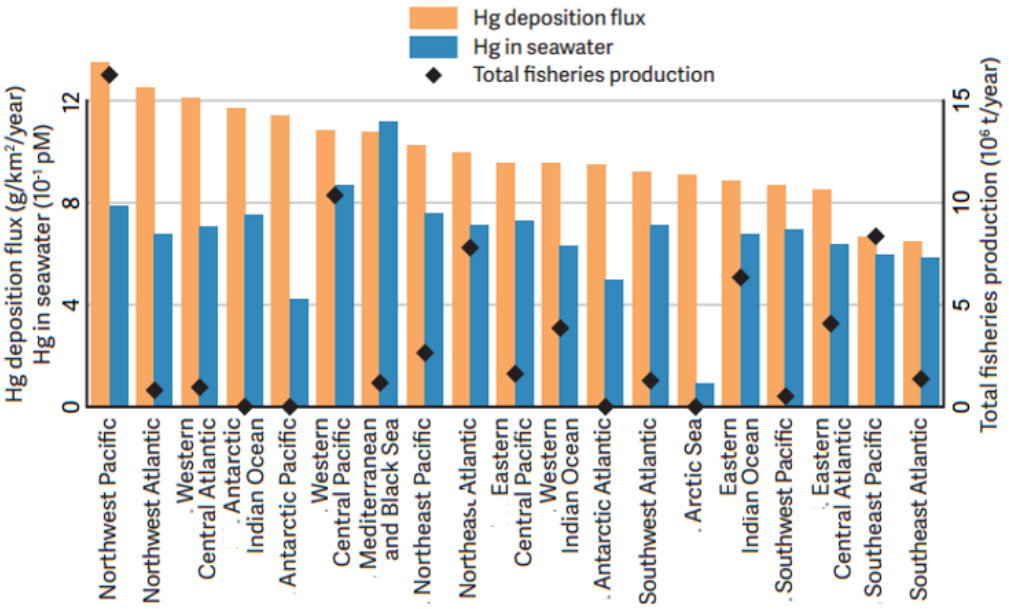

Figure 1: Average annual mercury deposition and total mercury concentration in the UN Food and Agriculture Organization (FAO) Major Fishing Areas in 2013.
Source: Global Mercury Modelling: Update of Modelling Results in the Global Mercury Assessment 2013.

spite of decades of technological and regulatory efforts to reduce mercury contamination, low levels of mercury are continuously released into the environment, causing mercury concentrations in water bodies to reach values between 0.01 to 12 ng/L (ppt) approximately (Stone et al., 2003). Even at such minute concentrations, mercury represents a serious and persistent threat to the public health due to its cycling, bioaccumulation and bioamplification throughout the food chain (Bellanger et al., 2013; Crump and Trudeau, 2009; Lamborg et al., 2014) triggering public agencies worldwide to issue fish eating guidelines and establish stringent regulations on industrial effluents (UNEP, 2013). The recent spotlights on large scale poisoning in the Peruvian Amazon and Indonesia highlight the global nature and urgency of the mercury problem (Fraser, 2016). The severity of the issue is compounded because mercury is persistent and cycles globally though wind and ocean currents as shown in **Figure 2**.

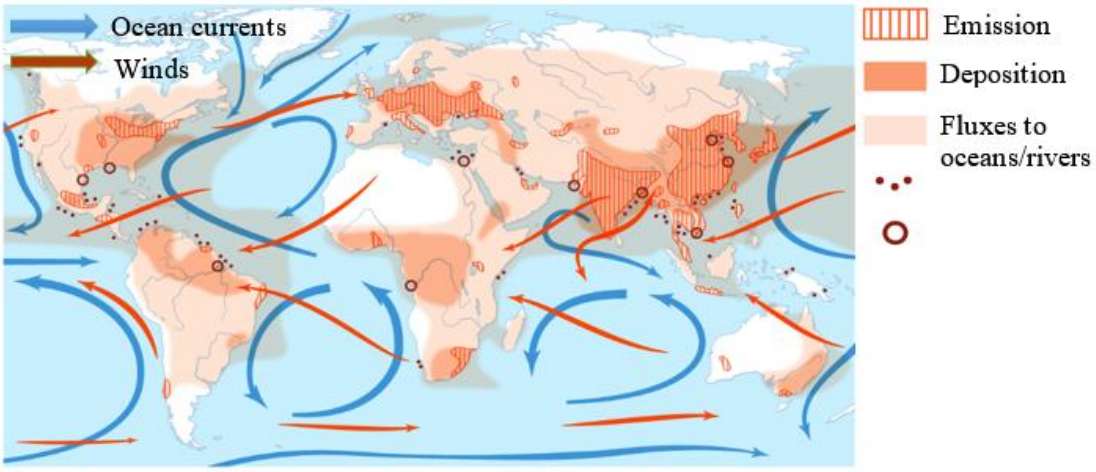

Figure 2: Mercury persistence and global cycling.
Source: AMAP/UNEP 2008, Technical Background Report to the Global Atmospheric Mercury Assessment; UNEP, Global Mercury Assessment 2013: Sources, Emissions, Releases and Environmental Transport, 2013. Designed by Zoï Environment Network / GRID-Arendal, Dec. 2012

1.3.1 Sources of Mercury Contamination

According to the United Nations Environmental Program (UNEP), mercury found in the top 100 meters of the world's oceans has doubled and concentrations in waters deeper than that have increased by 25% over the last century, mainly caused by the industrial activity (UNEP, 2013). According to Artic Monitoring and Assessment Program (AMAP)/UNEP report, the primary source of anthropogenic mercury is mining, principally as a byproduct of mining ores such as coal, iron and other metals. Artisanal and small-scale gold mining (ASGM) has been reported as the largest source of mercury release in environment, producing an estimated 650-1000 tons of mercury annually.

The secondary sources of mercury release include industrial processing, dental activities and research activities. For example, mercury chloride is used in vinyl chloride monomer production. Countries like China are the major hub of this industry and this country alone releases 610 tons of mercury annually. This number is

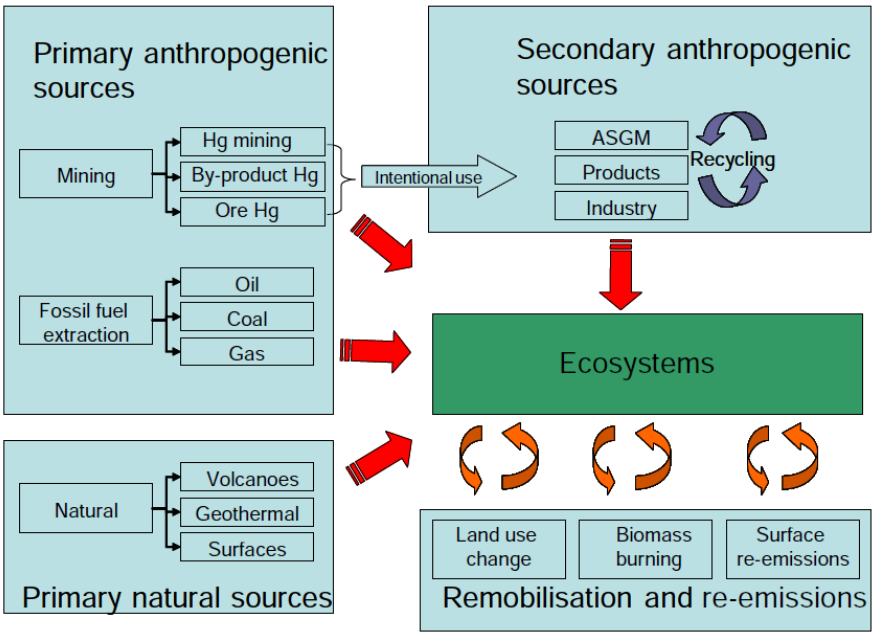

Figure 3: Sources of mercury and mobilization.
Source: AMAP/UNEP 2008, Technical Background Report to the Global Atmospheric Mercury Assessment; Arctic Monitoring and Assessment Program/UNEP chemicals branch. 159 pp.

estimated to increase annually by 25-30%. Another industry, which is the third largest contributor to the mercury problem is the chlor-alkali industry. Minor contributions are from mercury containing batteries, dental amalgams and mercury containing florescent lamps (Jozef M. Pacyna, 2008).

1.3.2 Pathways of Mercury Toxicity

Mercury exhibits different ionic species. Among them metallic/elemental mercury (Hg^0), mercurous (Hg^{1+}), mercuric (Hg^{2+}) and organic (CH_3Hg) forms are important in causing toxicity. Mercuric ions, being the most reactive species, pose the severe effect to human health. Elemental mercury has poor adsorption abilities and hence poses less toxicity; however, if inhaled in vapor phase then it is rapidly diffused and adsorbed by the lungs. Elemental mercury also has the ability to cross the blood brain barrier (BBB) and placental barrier (Fernandes Azevedo et al., 2012). Once it reaches the bloodstream, it is metabolized to Hg^{2+} and Hg^{1+}.

The metabolized ionic forms of mercury are more biologically reactive than other form. These forms of mercury are known to interact with thiol-containing enzymes such as glutathione, thioredoxin and other metalloproteins. This enzyme-Hg complex renders the enzyme inactive and imparts subsequent toxicities related to mercury (Gardner and Nyland, 2016). In another study, it was shown that Hg^{2+} significantly decreased the activity of the catalase enzymes present in the liver. This class of enzymes is recognized as the body's first defense against foreign oxidative species (Chen et al., 2015). The neurotoxic effects of mercury was studied by Al-Saleh et al and gave evidence for the relationship between a mother's mercury level and oxidative neurodegenerative stress in infants (Al-Saleh et al., 2016).

In some cases, when this divalent mercury forms complexes with one or two carbon chains it becomes organic mercury (methyl or ethyl mercury). It is this organic

mercury which deposits in the body and bio-accumulates in the food chain. When fish contaminated with methyl mercury is consumed, this compound is readily absorbed in gastrointestinal tract. From there, it travels through the bloodstream and can cross the blood brain and placental barriers. Once it reaches the target site it starts accumulating. Usually it accumulates in the hair scalp which has a higher ratio of amino acids. Although methyl mercury is removed from the body though fecal excretion, this compound still manages to accumulate in tissues. A study on rats has shown that methyl/ethyl mercury forms complexes with thiol containing amino acids and enzymes such as L-cysteine, methionine and glutathione. Thus, this complex also helps the mercury to pass the BBB. When it enters the liver, the complex is broken up into methyl mercury and the constituent amino acids. The former is reabsorbed and enters the bloodstream. This process of evading the liver's excretory system is known as a enterohepatic cycle (Clarkson et al., 2007). **Figure 4** summarizes the routes of different forms of mercury in human body.

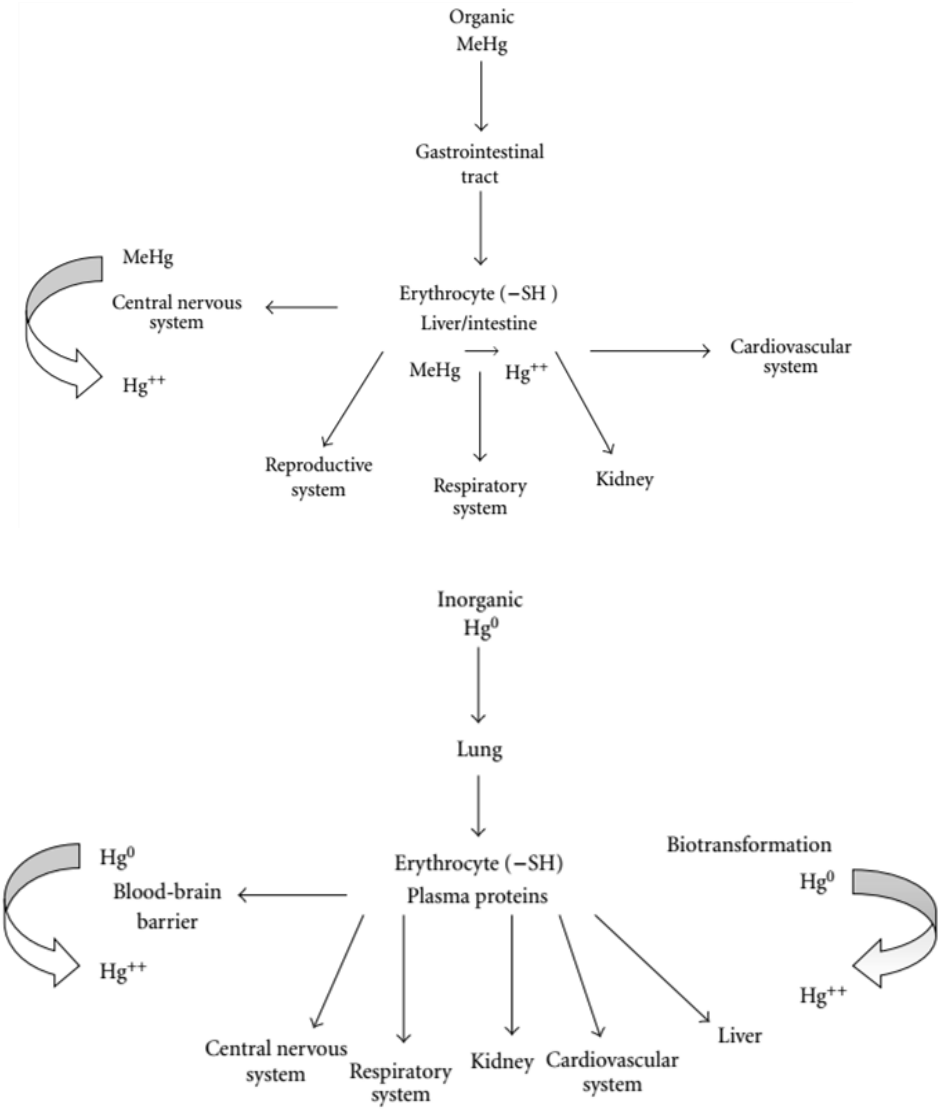

Figure 4: Route of different forms of mercury in body and their distribution. (Clarkson et al., 2007)

1.3.3 State of the Art in Mercury Removal Technologies

A remarkable number of materials and methods have been developed for mercury removal from water (Atwood and Zaman, 2006). Among those, adsorption has so far been the most widely used method, and activated carbon is the commercially leading material with the ability to remove aqueous mercury to less than 0.2 μg/L (Faulconer et al., 2012). Most adsorbents rely on the functionalization of different materials with sulfur, halogens, amine moieties (Roberts and Rowland, 1973) or other cations. Some commercially available technologies based on sulfur-

impregnated activated carbon claim to capture mercury from industrial wastewater to levels below 0.1 ppb. However, to achieve such a result, the influent flow needs to be pretreated and the flow rate reduced to increase the adsorption contact time to 90 min (Tonini et al., 2003). Currently there are numerous companies such as DOW Water and Process Solutions, Neopure and Solenis LLC who are using different conventional methods (activated carbon, ion exchange based) to remove mercury from water (**Table 1**).

Table 1. Companies offering mercury removal from water

Company name	Product name	Method used to remove mercury from drinking water
Selective Adsorption Associates, Inc (SAA)	Mersorb®	Activated carbon
Neopure	AntiMerCure™	Activated carbon
Frontier water systems	Custom Reactor system	Bioreactor having engineered microorganisms to reduce toxic elements
evoQUA water technologies	Pironox™	Chemical reduction
DOW water and process solution	DOWEX™ XUS 43604	Ion-exchange

1.3.4 Shortcomings of Current Technologies

Besides the contact time, which is paramount in determining the efficiency and influent flow rate required, the mercury removal rate is important to meet the regulatory requirements as well as enabling new applications. While currently available technologies are useful for reducing mercury in industrial wastewater where

the concentration ranges from 10 ppt to 50 ppb, they are unable to completely clean the waters, and small amounts of mercury are still discharged into the environment. Moreover, these technologies are not suitable for cleaning rain and surface waters where mercury concentrations range from 0.01 to 100 ppt and where acceptable standard limits can be extremely low (eg. 1.3 ng/L in the Lake Superior Basin) (Monson and Heiskary, 2008). In addition to the performance, the hazardous nature of the sorbent waste determines the method and cost of disposal and the sustainability of the technology. This is particularly important for the widely-used sulfur-functionalized sorbents. Despite very high binding constants (10^{15}–10^{17}) of sulfur-mercury (S-Hg) complexes, the S-Hg interaction is reversible under certain conditions and can undergo ligand exchange reactions in aqueous solutions or biological systems (Karatza et al., 2000) which presents a health risk if the sorbent waste is released into the environment.

1.4 Selenium

Selenium has attracted researchers because of its interesting physical and chemical properties (M. Schmidt, 1973). It has been widely explored as a photoconductor (Mayers et al., 2003; Shah et al., 2007). Selenium is also considered to be one of the important nutrients for the human body as different selenoenzymes such as glutathione peroxidase require selenium as a cofactor for their proper functioning (Xiang et al., 2009).

1.4.1 Selenium Nanomaterials

In recent years, selenium nanoparticles (SeNP) or nanospheres (SeNS) have gained increasing attention due to their versatile biological activity and lower toxicity as compared to other forms of selenium (Forootanfar et al., 2014; Malhotra et al., 2015; Ramos and Webster, 2012; Wang et al., 2007; Zhang et al., 2005). In addition,

many recent reports reveal their remarkable, growing number of applications. Since selenium is a good photoconducting material, SeNP have been integrated in high-power batteries, solar cells and electronics.(Chaudhary, 2014; Dong et al., 2014; Luo et al., 2013; Peng et al., 2015). The major focus of SeNP applications has been around their biological activity. Besides their antimicrobial properties, which include the prevention of biofilm formation (Phong et al., 2016; Sonkusre and Singh Cameotra, 2015; Tran and Webster, 2011; Wang et al., 2015), antioxidant abilities (Yu et al., 2016b) and anti-inflammatory effects (Malhotra et al., 2015), SeNP also make cancer cells susceptible to drugs, thereby acting as a good anti-tumoral and a chemopreventive agent (Bao et al., 2015; Stolzoff and Webster, 2016; Tran et al., 2009; Yu et al., 2016a). SeNP are also used in a variety of chemical and analytical processes including controlling crystal growth (Zhong et al., 2015), sensing (Chaudhary, 2014; Dwivedi et al., 2013; Prasad et al., 2015), biocatalysis and cellular imaging applications due to their intrinsic fluorescence and enzyme-like properties (Guo et al., 2016; Khalid et al., 2016).

With the proven applications and importance of SeNP, researchers have proposed different ways to synthesize SeNP. Many challenges are faced for the synthesis of SeNP. First, the ability to control the size within a wide range. Size control is important not only because it allows tuning the optical properties of the nanospheres but also because the biological activity of the SeNP can be dependent on their size (Peng et al., 2007). Other difficulties include the production of single nanoparticles (and not aggregates) with minimal use of stabilizing agents, and long-term stability of the synthesized nanoparticles.

1.4.2 Synthesis of Selenium Nanomaterials

Currently, selenium nanoparticles are produced using several methods. Many reports have used microbes, such as *Pseudomonas alcaliphila*, with metabolic systems that can reduce selenium sources to elemental selenium (Oremland et al., 2004; Shirsat et al., 2015). Although the microbial route of selenium nanospheres (SeNS) synthesis is eco-friendly, the synthesis requires several hours to several days for cell growth, yields polydisperse particles ranging from 50 nm to 500 nm, and the nanoparticles are produced with a natural coating of extracellular polymeric substances (Jain et al., 2015). This coating, while it helps stabilize the particles, may also hinder the activity of the particles and limit their use in certain applications, like mercury capture, where the surface of the nanoparticles needs to be accessible (Johnson et al., 2008). Chemical reduction of selenous acid is another method used to prepare SeNP in the presence of a reducing reagent (e.g. hydrazine, hydroquinone, glucose, glutamic acid, and cysteine) (Chen et al., 2009; Gates et al., 2002; Jeong and Xia, 2005; Kumar et al., 2014; Nie et al., 2016) and different stabilizing agents such as polyvinyl alcohol, polyethylene glycol, sodium dodecyl sulfate (SDS) and monosaccharides/polysaccharides (Shah et al., 2007; Shin et al., 2007; Stroyuk et al., 2008; Zhang et al., 2010). The reported sizes range from 5 nm to 300 nm.

Other less common methods include hydrothermal and microwave-assisted syntheses (Shin et al., 2007; Yu et al., 2016b). Other attempts to use SeNPs-based sorbents rely on first synthesizing and then adsorbing SeNPs on solid supports by soaking (Huang et al., 2015; Johnson et al., 2008; Lee, 2012; Sawyer, 2012). This process results in anisotropic aggregates, poor surface coverage and increased risk of leaching under acidic conditions, which could cause secondary pollution at high Se concentrations.

1.4.3 Selenium and Mercury Removal

Selenium is known to capture mercury with exceptionally high binding affinity with a constant of 10^{-45} one-million-fold higher than the binding affinity between mercury and sulfur (Khan and Wang, 2009). As a result, the interaction between Se and Hg yields biologically stable Se-Hg precipitates, with extremely low solubility (10^{-58} to 10^{-65}) as compared to that of S-Hg precipitates (10^{-52}). The strong electrostatic interaction between them contributes towards the high affinity between Se and Hg. As shown in **Figure 5**, the density of Se electron cloud is higher than the Hg, which favors dipolar interactions (Ralston, 2008b). The first use of selenium for mercury capture was reported in the 1970s (Habashi, 1978). Ceramic grains impregnated with metallic selenium have been developed and commercially used in Sweden to reduce elemental mercury emissions in flue gas, with 90% removal efficiency (Martha H. et al., 1997). The technology has not developed further due to limited removal capacity and rapid saturation of the sorbent.

Hurt et al. revived the idea of using selenium by showing that selenium nanoparticles exhibit up to 100 times higher mercury removal efficiency of gaseous mercury than conventional selenium or commercially available sorbents including activated carbon (Johnson et al., 2008; Ralston, 2008b). Despite the superior performance, only 7% of the potential mercury removal capacity of selenium nanoparticles was achieved by Hurt et al., and the need to use nanoparticle aggregates instead of single nanoparticles further reduces the surface area and removal rate (Hurt et al., 2013; Johnson et al., 2008).

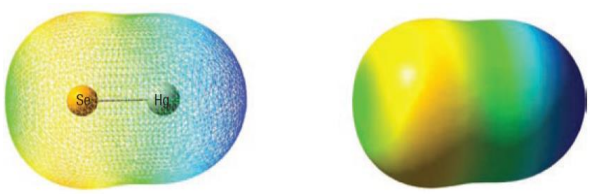

Figure 5: Se-Hg electrostatic potential surface interaction (blue: positive charge; yellow: negative charge)(Ralston, 2008a).

2. Research Objectives

The overall goal of the thesis is to use nanotechnology to develop a more efficient and cost-effective mercury sorbent that overcomes the limitations of currently available technologies. Specific research objectives include:

1. Development of a new method for the synthesis of selenium (Se) nanomaterials on solid support. As discussed earlier, selenium has been found best match for mercury because of its high binding constant and irreversible interaction. This property led us to start exploring the use of Se for developing sorbent for mercury removal. Selenium nanoparticles were chosen because they have enhanced surface area, which leads to maximum adsorption capacity. The methods which are already available for synthesis of SeNP in solution usually use stabilizers to prevent particles from aggregation. The use of stabilizers lead to unreactive Se surface for mercury. Secondly, SeNP in solution cannot be used because it will be difficult to remove the particles from solution after treating with mercury. Because of these limitations, we thought to grow SeNP on a solid support. Thus, to achieve first step, the process of synthesis of SeNP was modified to make it suitable for solid supports.

2. Selection of solid supports and study of the efficiency of Se nanoparticles in mercury removal. After modifying the process for the synthesis of SeNP, it was tested on different solid supports and sponge based solid supports were selected. The advantage of 3D and porous matrix of sponge made it best candidate for the support. In addition to this, the idea to develop sorbent for water cleaning, can be achieved by using water absorption and expulsion capabilities of a sponge. Objectives 1 and 2 are discussed in chapter 3.

3. **Characterization of the new nanoselenium-based sorbent and application of the technology to real world samples.** Among all the sponges tested (discussed in chapter 3), the polyurethane sponge showed the best results in terms of thermal, physical and chemical stability. Selenium nanoparticles were grown on polyurethane sponge. The characterization of the nanoSe sponge was done to understand the mode of mercury adsorption. Adsorption kinetics and isotherms were analyzed for that purpose. To demonstrate the safety of nanoSe sponge, safety evaluation studies were also done. Then finally, the application of nanoSe sponge on real world samples such as lake and industrial water was shown to validate the preferential removal of mercury in a complex water systems. This objective is discussed in chapter 4.

Chapter 3: Sponge-Supported Synthesis of Colloidal Selenium Nanospheres (SeNS)

3.1 Summary

With increasing biomedical and engineering applications of selenium nanospheres (SeNS), new efficient methods are needed for the synthesis and long-term preservation of these nanomaterials. Currently, SeNS are mostly produced through the biosynthesis route using microorganisms or by using wet chemical reduction, both of which have several limitations in terms of nanoparticle size, yield, production time and long-term stability of the nanoparticles. Here, we introduce a novel approach for rapid synthesis and long-term preservation of selenium nanospheres on a solid microporous support by combining a mild hydrothermal process with chemical reduction. By using a natural sponge as a solid 3-dimensional matrix for nanoparticle growth, we have synthesized highly monodisperse spherical nanoparticles. Nanoparticles of wide range of size (10 nm-1000 nm) can be produced and extremely high yield in a relatively short period (1 h). Additionally, the synthesized SeNS can be stored and retrieved whenever needed by simply washing the sponge in water. Keeping the nanospheres in the support offers remarkable long-term stability as particles left on the sponge preserve their morphological and colloidal characteristics even after 8 months of storage. Furthermore, this work reveals that selenium nanospheres can be used for efficient mercury capture from contaminated waters with a record-breaking mercury removal capacity of 1900 mg/g.

3.2 Materials and Methods

All chemicals including selenous acid (98%), sucrose (>99.5%), lactose (>99%), fructose (>99%), glucose (>99.5%) and hydroquinone (99%) were purchased from Sigma Aldrich (St. Louis, MO, USA). Natural, unbleached honeycomb sponges

(5-6 in), polyvinyl alcohol sponges, polyurethane (PU) and natural silk sponges were purchased from various online suppliers. All aqueous solutions were prepared in nanopure water.

3.2.1 Characterization of natural honeycomb sponge

The natural sea sponge was characterized using scanning electron microscopy (JEOL 6500, 6700 SEM) and Fourier transform infrared spectroscopy (Nicollet Series II Magna IR-System FTIR). Average surface roughness and microscopic contact angle were measured using a KLA-Tencor P-7 and an MCA-3 (Kyowa Interface Science Co (Japan)) respectively. Absorption capacity was estimated via water uptake in sponges of uniform size.

3.2.2 Synthesis of Selenium nanospheres on natural honeycomb sponge

The natural sea sponge was first soaked in 25% sucrose in nanopure water for 15min. The sponge was then submerged in a selenous acid solution (1.4 M) for 25 min. After removal of the sponge the remaining solution was stored at room temperature and used later in the synthesis process. The soaked sponge was then carefully removed and dried in a vacuum oven (-2.6 kPa) at 110 ºC (Isotemp vacuum oven Model 280A from Thermo Scientific) for 10 min. After drying, the sponge was added to the hydroquinone solution (at different concentrations depending on the desired nanosphere size) for 10 min. The remaining selenous acid from the previous step was added to the sponge after exposition to hydroquinone. The sponge was then washed with nanopure water to retrieve the selenium nanospheres for further characterization or use.

3.2.3 Nanoparticle characterization

Selenium nanoparticles were recovered from the sponge via washing in water and used for characterization. Smaller particles were drop casted onto silicon wafers

directly from solution. Larger particle solutions were centrifuged (14000 rpm for 10 minutes) and suspended in fresh nanopure water prior to drop casting. Scanning electron microscopy (SEM) imaging was performed using JEOL 6500. Dynamic light scattering (DLS) was conducted using a Microtrac NanoFlex particle analyzer to determine the size, zeta potential and polydispersity index of the recovered nanospheres solution. *Energy dispersive X*-ray *analysis* (EDXA) and high resolution transmission electron microscopy (HRTEM) were conducted using a FEI Tecnai G^2 F30 electron microscope. Samples for TEM imaging were prepared by drop-casting 3 µL sample on a carbon copper grid (Carbon square mesh, CU, 200 mesh from Electron Microscopy Sciences). Raman spectroscopy was performed using a Witec alpha300 R confocal Raman microscope with a UHTS300 spectrometer and a DV401 CCD detector with an Omnichrome argon ion laser with 532 nm excitation and 50 mW output power was used. For Raman sample preparation, nanoparticles were centrifuged at 12,000 rpm for 30 min and the pellet was re-suspended in water. Then 20 µL was drop casted on Si substrate and dried at room temperature for subsequent analysis.

3.2.4 Nanoparticle filtration

The separation of micrometric SeNS from smaller SeNS (Figure 17) was performed by membrane filtration. After recovery of SeNS from the sponge via washing in water, solutions were passed through 0.4 µm polycarbonate filter membranes (Whatman Nucleopore Track-Etch Membrane) using an extrusion device (Mini-Extruder Set, Avanti Polar Lipids Inc.).

3.3 Results and Discussion

The main limitations of working in the liquid phase when synthesizing colloidal nanoparticles is the need for stabilizing agents, and the subsequent long-term

stability of the nanoparticles in solution. One way to overcome these limitations is to explore the growth and retrieval of nanoparticles on solid supports. The use of sponges represents an attractive approach due to their increased surface to volume ratio for nanoparticle growth, thus increasing the yield. Also, the sponges offer a confined environment to facilitate diffusion and enhance chemical interactions. Furthermore, the sponge can be used not only for nanoparticle growth but for long-term storage as well. Such advantages overcome the need for nanoparticle preservation through daunting and costly lyophilization processes (Abdelwahed et al., 2006; Alkilany et al., 2014) or nanoparticle storage in solutions prone to changes in pH and unstable aqueous environments (Fang et al., 2009).

3.3.1 Sponge-Supported Synthesis

The first challenge in this work was to find a sponge with a suitable interface that can adsorb selenous acid and allow nanoparticle growth, while offering a weak interaction with the nanoparticles to allow easy retrieval of the nanoparticles in solution. To favor isotropic nanoparticle growth on the sponge fibers and not in solution, we have designed a process that follows two major phases: (1) immobilization of selenous acid on the sponge fibers, and (2) nanoparticle growth on the sponge surface. The immobilization is performed by immersion of the sponge in a 25% sucrose solution. The sponge is then squeezed before being immersed in selenous acid solution and dried in a vacuum oven for 10 min at 110 ºC. These steps are designed to provide a homogeneous sucrose coating to the sponge to allow isotropic immobilization of the selenous acid ions by interaction with the sucrose hydroxyl groups, thus promoting a homogenous growth of nanoparticles. The drying step was intended to remove excess liquid from the sponge and induce the attachment of the sucrose-Se ions into the sponge fibers. After drying, the sponge is immersed in

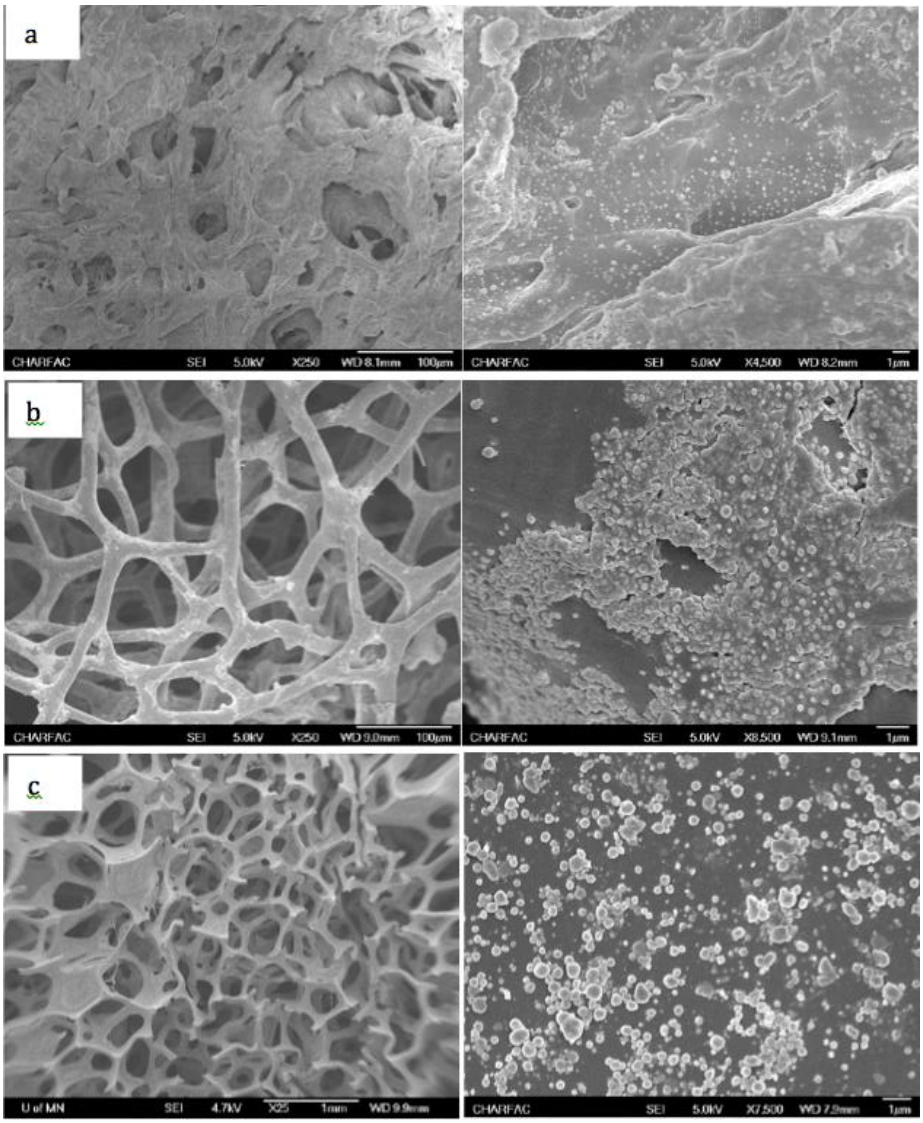

Figure 6. Growth of selenium nanoparticles on different sponges using the same process. (a) Polyvinyl alcohol sponge, (b) natural silk sponge, and (c) polyurethane sponge.

reducing agent solution such as hydroquinone to convert the adsorbed Se ions into elemental selenium (Se^0). Further immersion of the sponge in additional Se ions solution leads to SeNS surface growth on the sponge fibers.

3.3.2 Sponge Properties

To select an adequate sponge as mentioned earlier, we have conducted the synthesis process on many synthetic and natural sponges including polyvinyl alcohol (PVA), polyurethane (PU), silk (composed of fibroin proteins) and honeycomb

(composed of spongin scleroproteins) sponges. Scanning electron microscopy (SEM) images showed that PVA, PU, and silk sponges performed poorly (**Figure 6**).

After synthesis, all sponges changed color to dark brown indicating the growth of nanoparticles. While the PVA sponge showed small nanoparticles with low density, PU and silk sponges showed aggregates. In addition, harvesting the particles from the sponges was unsuccessful due to a strong adsorption to the sponge fibers but also due to low thermal stability of PVA and silk sponges during the hydrothermal process at 110ºC.

The honeycomb sponge revealed remarkable growth of perfectly spherical nanoparticles (**Figure 7**). The SEM images (**Figure 7a** and **7b**) showed that the sponge fibers were completely and densely covered with monodisperse nanospheres. A simple washing of the sponge with room temperature water resulted in an instantaneous release of most of the nanoparticles into solution with very low amount

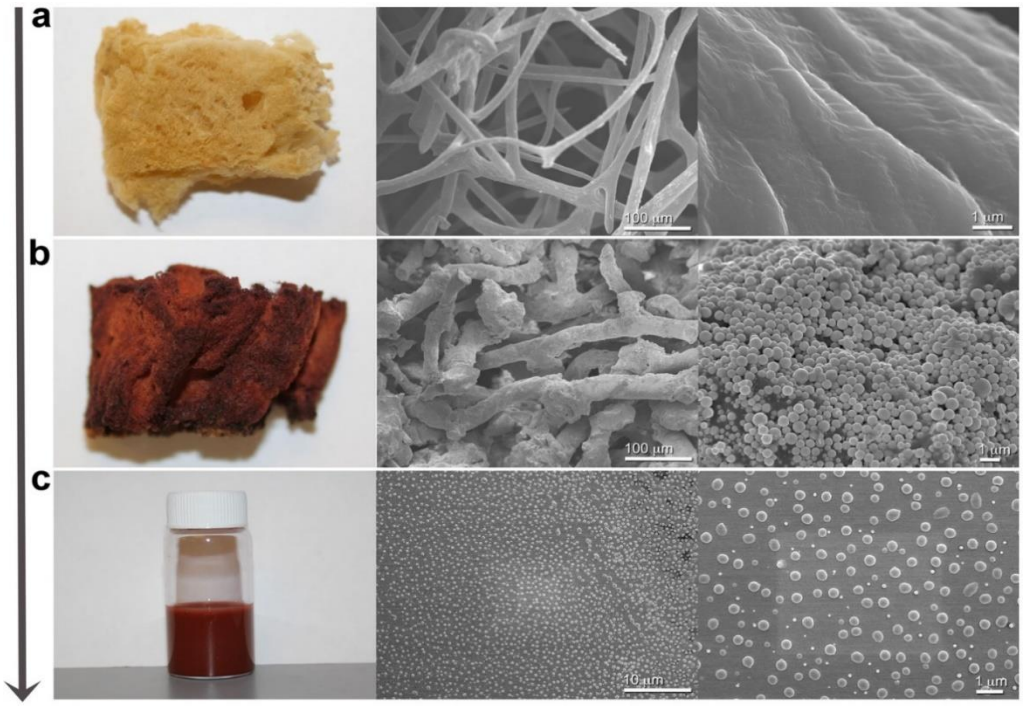

Figure 7. Concept of sponge-supported growth of colloidal SeNS. (a) Photography of polyamide honeycomb sponge and corresponding SEM images. (b) Polyamide honeycomb sponge after growth of SeNS with a combined hydrothermal/chemical reduction process, and corresponding SEM images. (c) Retrieval of SeNS from the sponge into a colloidal solution and corresponding SEM images after deposition on a silicon substrate for visualization purposes.(Snober et al., 2016)

of sucrose fibers (**Figure 7c**). The yield and quality of SeNS can be explained by a combination of morphological, chemical and interfacial properties of the honeycomb sponge but also by the growth mechanism discussed later.

Unlike the PVA, PU and silk sponges that all have water contact angles higher than 110ºC, the honeycomb sponge composed mainly of polyamide shows a hydrophilic surface with a contact angle of 77 º ± 5 º (**Figure 8**).

This hydrophilicity favors the interaction of sucrose and selenous acid with the sponge fibers through intermolecular hydrogen bonds (O-H…Se), and prevents the aggregation of nanoparticles as observed with other sponges. In addition to the interfacial properties, the polyamide composition of honeycomb sponge offers a high heat and chemical resistance and good mechanical properties.(Saper and White, 1958)

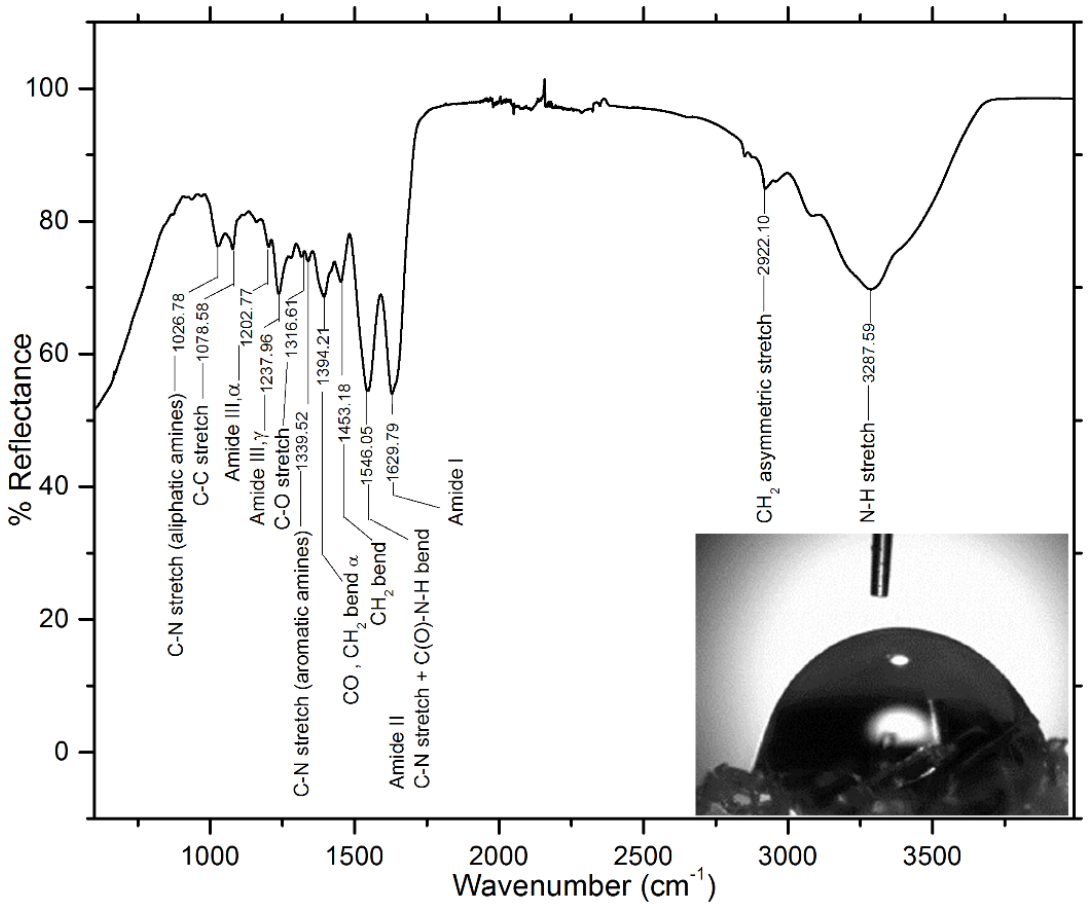

Figure 8. Fourier transform infrared (FTIR) spectrum of honeycomb sponge showing a mainly polyamide composition. The inset depicts a water contact angle of 77º ± 5º for the same sponge.

The yield of SeNS is particularly remarkable and could be explained by the multiple growth mechanisms that will be addressed in the following sections, as well as the 3D matrix of the sponge. The sponge fibers (10-30 µm wide) and their roughness (10-20 nm) provide a high surface to volume ratio, which is of paramount importance as the nanoparticle growth mechanism mostly depends on surface diffusion as we will see in the next sections. Also, the hydrophilicity of the sponge allows absorption of up to 20 ± 3 mL water/g sponge.

3.3.3 Role of Sucrose

As stated previously, sucrose was used in this synthesis to provide a uniform surface for the initial reduction of selenium. To gauge the effect of other saccharides and the impacts of both mono and disaccharides, the synthesis was conducted with four different sugars, namely fructose, glucose, lactose and sucrose. Only treatment

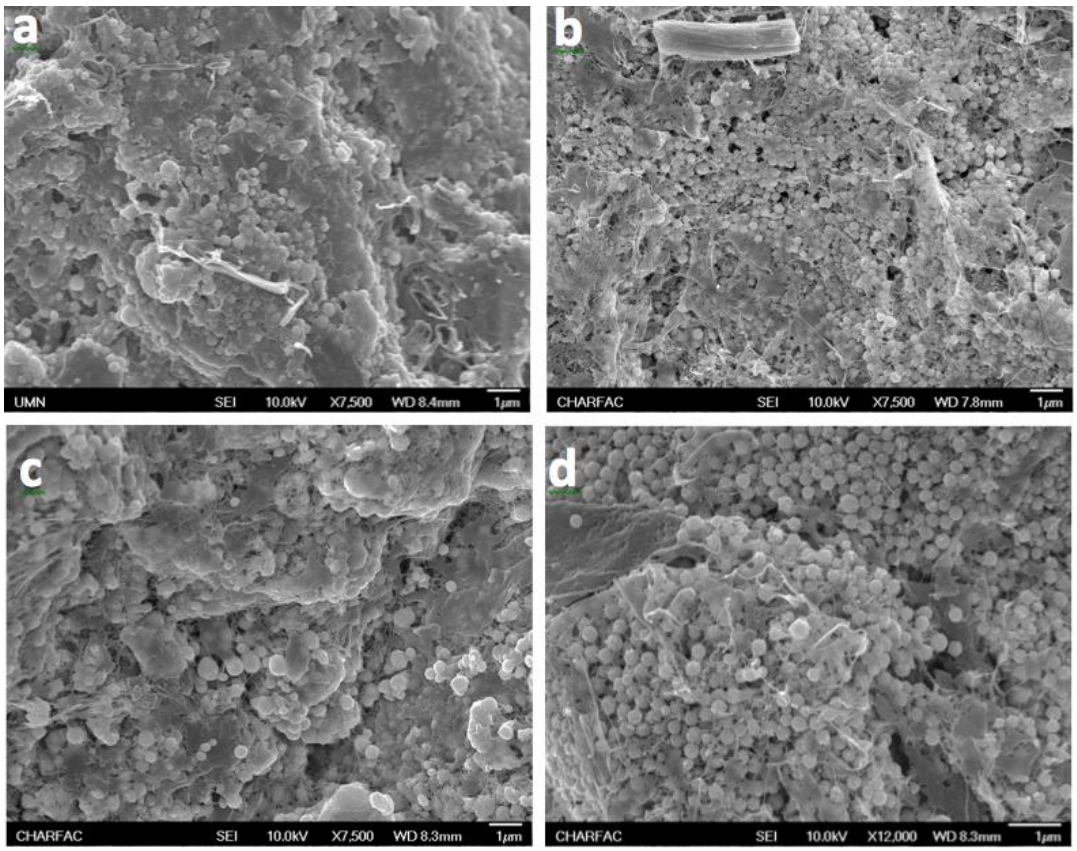

Figure. 9: Scanning electron microscope images of sponge-supported growth of SeNS using different saccharides: (a) lactose, (b) fructose, (c) glucose, and (d) sucrose as a sponge coating before synthesis.

with fructose resulted in particle growth with similar quality than sucrose, regarding particle size, monodispersity and surface coverage (**Figure 9**).

Lactose and glucose yielded fused, non-spherical particles. These results along with the composition of sucrose (a combination of a fructose and glucose units), and lactose (a combination of a glucose and galactose units) could suggest that the efficiency of sucrose in this process may be due to its fructose unit. However, further experimental study needs to be done understand the role completely. An additional experiment was conducted to ascertain the proper level of sucrose loading. Briefly, sponges soaked in varying sucrose concentrations (5%, 10%, 25%, and 50%) were used in the synthesis described above, and the sponges analyzed with SEM imaging. The results depicted in (**Figure 10)** indicate that a sucrose concentration of 5% is sufficient to provide the optimum growth condition for SeNS, and the increase in

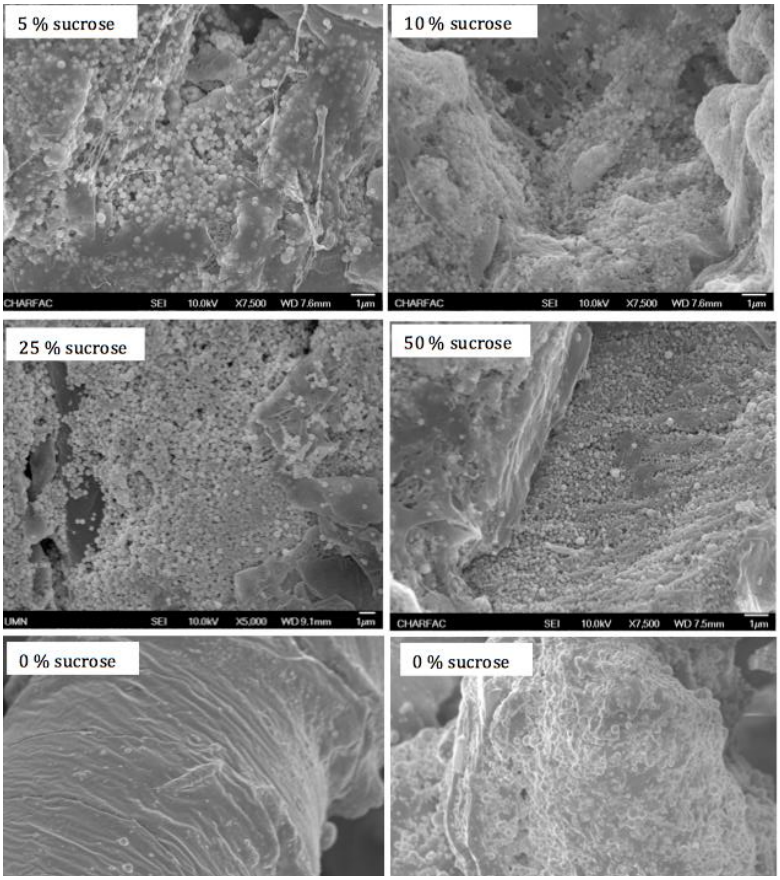

Figure 10. SEM images showing the effect of different sucrose concentrations on the growth of SeNS on the sponge.

sucrose concentration up to 25% does not affect the quality of the nanoparticles. However, nanoparticle retrieval seems to be much easier at a concentration of 25% sucrose. Without any saccharide coating, SeNS appeared in non-uniform patches with a poor yield, high polydispersity, and significant agglomeration.

3.3.4 Growth Mechanism and Size Control of SeNS

In this process, SeNS synthesis involves two major steps: an initial hydrothermal growth, followed by growth through chemical reduction using hydroquinone. **Figure 11** shows the composition of the growth medium during the combined hydrothermal/chemical reduction process. As we can see, three types of nanoparticles can be distinguished: (i) a highly dense network of small SeNS of 5-10 nm, medium-size SeNS or 50-150 nm, and larger particles of 200-1000 nm. When the sponge is observed after the hydrothermal process and without chemical reduction,

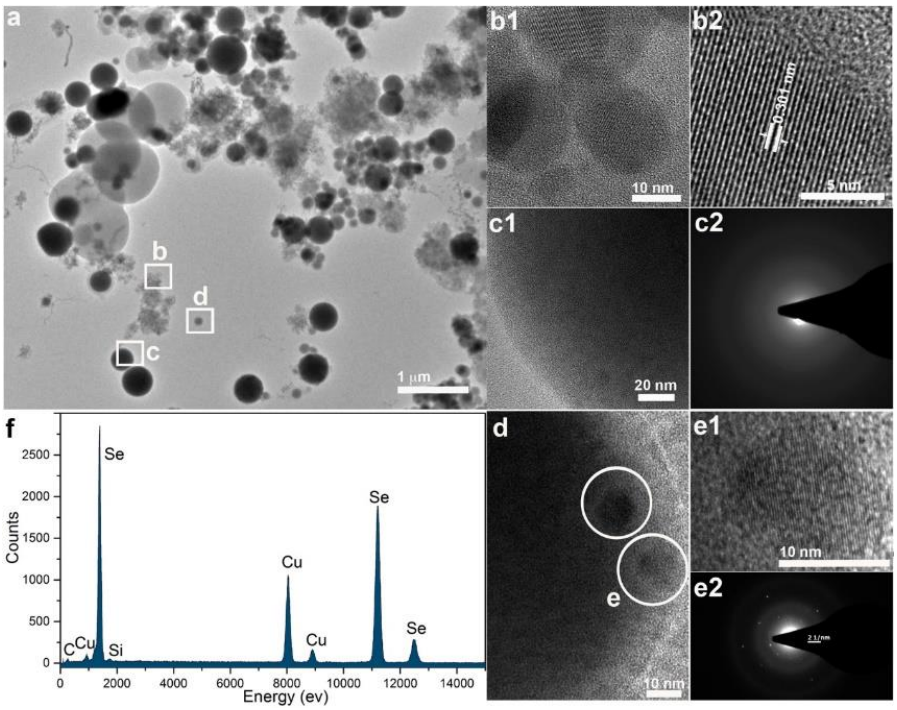

Figure 11. Structure and composition of SeNS synthesized by the combined hydrothermal/chemical reduction process. (a) TEM image of SeNS during growth. Three types of nanoparticles can be identified in the HRTEM images: small crystalline SeNS (b, b1 and b2), large amorphous SeNS (c, c1 and c2), and medium size amorphous SeNS (d). These particles incorporate small crystalline SeNS (e, e1, and e2). (f) EDX spectra showing the composition of the three types of SeNS.

only small and medium-size particles are found. **Figure 11 (b1-d)** also reveals that the small SeNS are crystalline (d (021) = 0.301 nm), while all other particles in the medium are amorphous.

This result is also confirmed by Raman analysis (**Figure 12**). Another unexpected result is shown in **Figure 11d (d1 and d2).** The small crystalline SeNS seem to be internalized by the medium-size particles, which represent the first hint of one of the growth mechanisms. The energy dispersive X-ray (EDX) spectrum demonstrates that all nanoparticles are solely composed of pure selenium (**Figure 11f**). The observed copper and trace carbon and silicon are caused by the TEM grid. The composition of the growth medium provides some insight into the growth mechanism where surface diffusion of different growth species plays a capital role. When the selenous acid soaked, sponge is heated, the selenium ions present in the sponge matrix are reduced to elemental selenium (Se^0). It should be noted that the

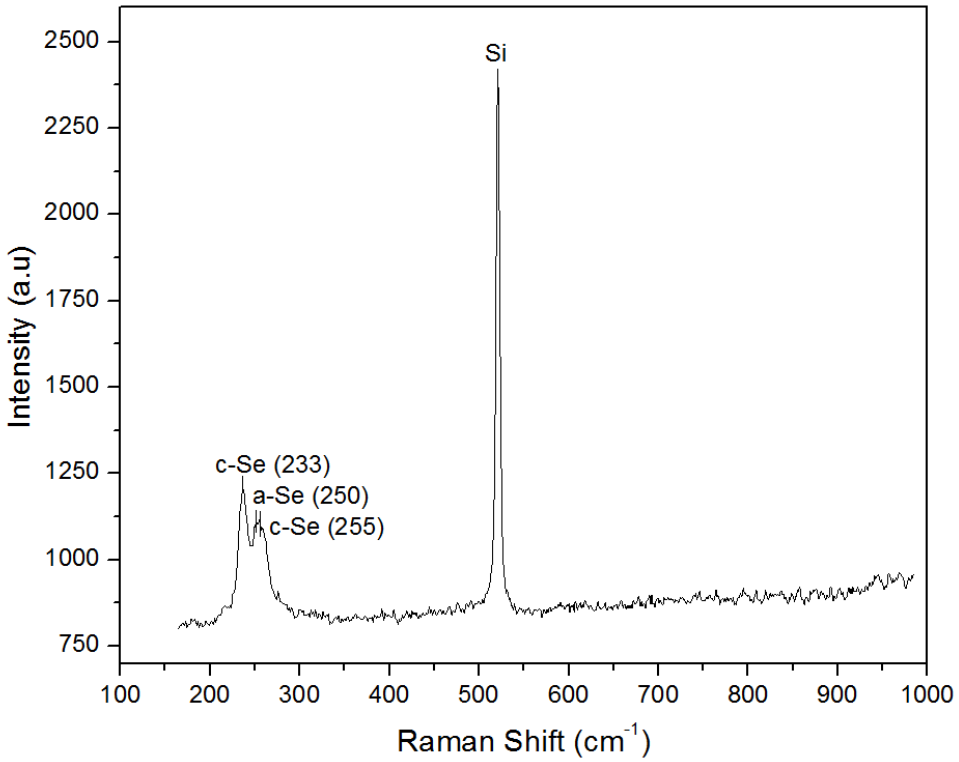

Figure 12. Raman spectroscopy of selenium nanospheres showing two peaks at 233 and 250 cm^{-1} corresponding to crystalline (c) and amorphous (a) Se respectively. A shoulder peak was also observed at 255 which corresponds to c-Se.

reduction is primarily caused by the heating, the mild vacuum conditions were used in this synthesis to expedite evaporation of water from the sponge. The reduced selenium ions then diffuse and crystalize on the surface of the sponge fibers under the effect of heat (110°C) and rapid water evaporation. The surface diffusion results in instantaneous growth of 5-10 nm crystalline SeNS.

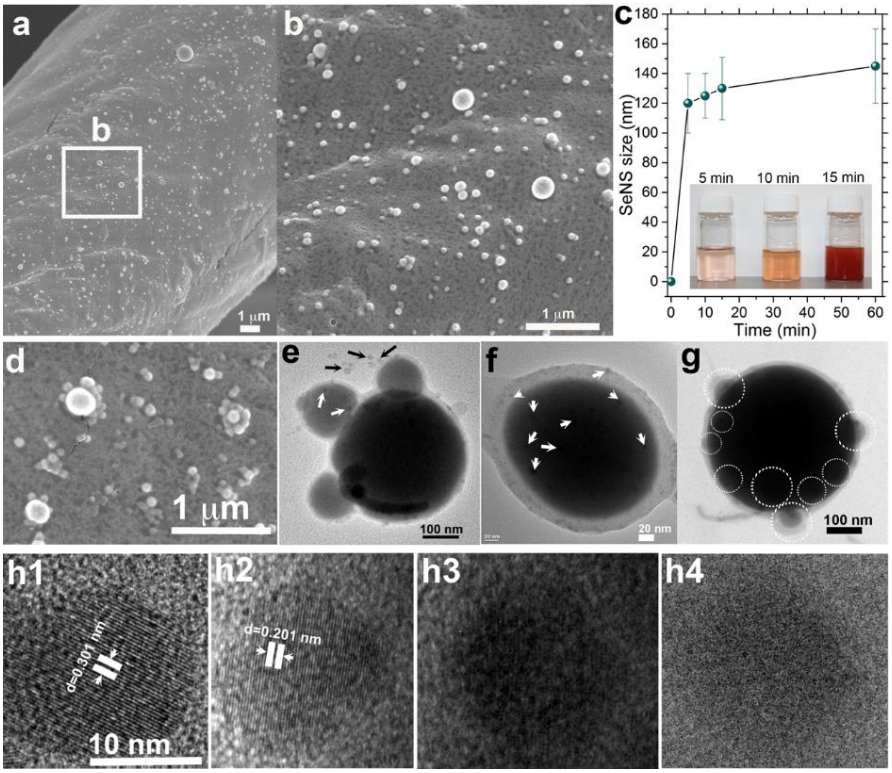

Figure 13. Growth mechanism of SeNS by diffusion-internalization of smaller nanoparticles during the hydrothermal process. (a) and (b) SEM images of the sponge fiber after the growth of SeNS with the hydrothermal process. (c) Evolution of the size of SeNS as a function of the incubation time of the sponge at 110°C. The inset shows the corresponding SeNS solution retrieved from the sponges after incubation at different times. (d) SEM image showing the agglomeration of small SeNS around particles. (e) TEM images show 10 nm crystalline SeNS (arrows) incorporated by 100 nm amorphous SeNS, while 100 nm SeNS are internalized by bigger particles. (f) TEM images of amorphous SeNS internalizing a large number of crystalline SeNS (5-10 nm). (g) TEM image of large amorphous SeNS internalizing smaller amorphous SeNS. (h) HRTEM images showing the change in the crystalline structure or phase of 10 nm crystalline SeNS over time after internalization in bigger amorphous SeNS.

It’s interesting to note that the small crystalline SeNS reach a maximum size of 10-15 nm, which is probably due to diffusion-limited growth. The second set of SeNS observed after the hydrothermal process are around 50-150 nm (**Figure 13a, b**). These particles grow and reach their maximum size within the first 5 minutes of the hydrothermal process. When the sponge is incubated for different times under hydrothermal conditions, the retrieved SeNS solutions exhibit different colors depending on the incubation time (**Figure 13c).**

However, the change in color after different incubation times (5 min, 10 min, 15 min) reflects more a change in nanoparticle concentration and distribution rather than nanoparticle size, as confirmed by SEM images (**Figure 14**).

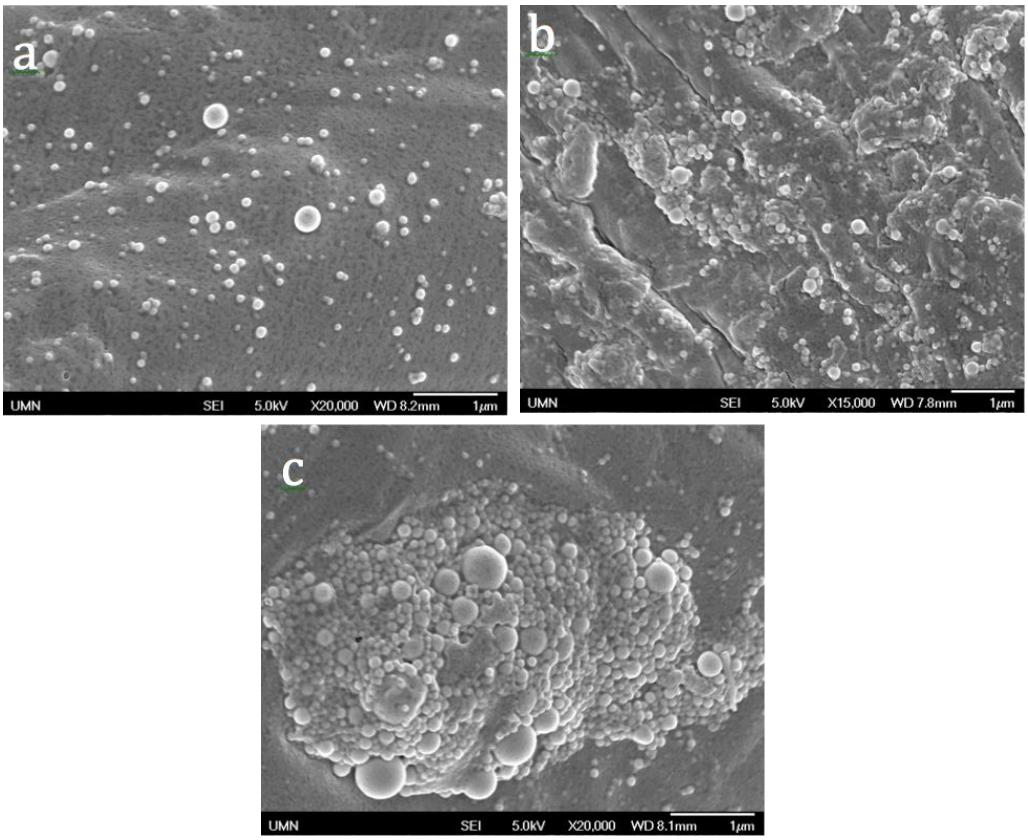

Figure 14. Hydrothermal synthesis of SeNS at 110°C for different incubation time: (a) 5 min, (b) 10 min, and (c) 15 min.

As for the amorphous SeNS with a size range of 50-150 nm, their growth is likely mediated by two concurring mechanisms. First, surface diffusion of elemental selenium under heating results in amorphous agglomeration due to interfacial forces generated by rapid water evaporation. The resulting SeNS then continue their growth up to around 150 nm by internalizing the small crystalline SeNS that come into contact due to surface diffusion. **Figure 11 (d, e, f, g)** reveal that both small crystalline SeNS and medium-size amorphous particles diffuse and get internalized by bigger "phagosome" nanoparticles. This mechanism could explain the high monodispersity of the synthesized nanoparticles, as big particles grow by internalizing small ones. A close look at the internalized small crystalline nanoparticles shows that the particles are not only internalized but also undergo a phase change from crystalline to amorphous within the host particle. **Figure 13 (h1-h4)** represents crystalline SeNS before (h1) and after internalization (h2-h4). Images h1-h4 were taken from nanoparticles localized at different distances from the center of the phagosomal particle. Nanoparticles that are closer to the center are particles that were

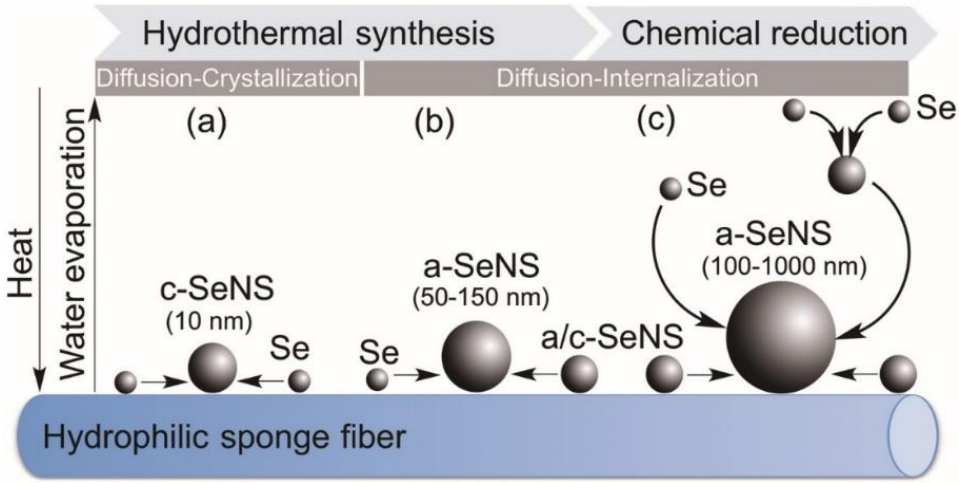

Figure 15. Scheme representing the hypothetic mechanism of sponge-supported synthesis of crystalline (a) and amorphous (b, c) SeNS, during the combined hydrothermal and chemical reduction process. The arrows show the direction of surface diffusion of the nanoparticles or growth species under the effect of heat and water evaporation.

internalized first and thus have a longer residence time inside the phagosomal particle. The HRTEM imaging reveals that the internalization process immediately affects the crystalline structure by decreasing the fringe spacing from d(021)=0.301 nm (**Figure h1**) to d(230)=0.201 nm (**Figure h2**). Over time, the internalized SeNS become amorphous and cannot be distinguished from the surrounding material.

Once the sponge is removed from the vacuum oven (hydrothermal process), the sponge contains mainly small crystalline SeNS and medium-size amorphous SeNS. To allow further growth of the nanopartilces, the sponge is immersed in hydroquinone as a reducing agent, then exposed to a solution of selenous acid. The chemical reduction promotes further binding to the nanoparticles present on the sponge. From this point, SeNS growth on the sponge fibers likely occurs via two main reaction pathways (**Figure 15**).

Selenium ions present in solution can be reduced at the vicinity of the sponge surface and either diffuse and condense on already grown nanoparticles on the surface, or agglomerate in solution into small amorphous particles that will be internalized once they reach the surface. Concurrently, large SeNS can grow by surface diffusion/internalization of medium-size nanoparticles as described earlier. These reaction pathways are non-exclusive, as particles can form via one or many of these processes simultaneously. The chemical reduction not only allows further growth of SeNS but also enables size control from 100 nm to 1000 nm by varying hydroquinone concentration (**Figure 16**).

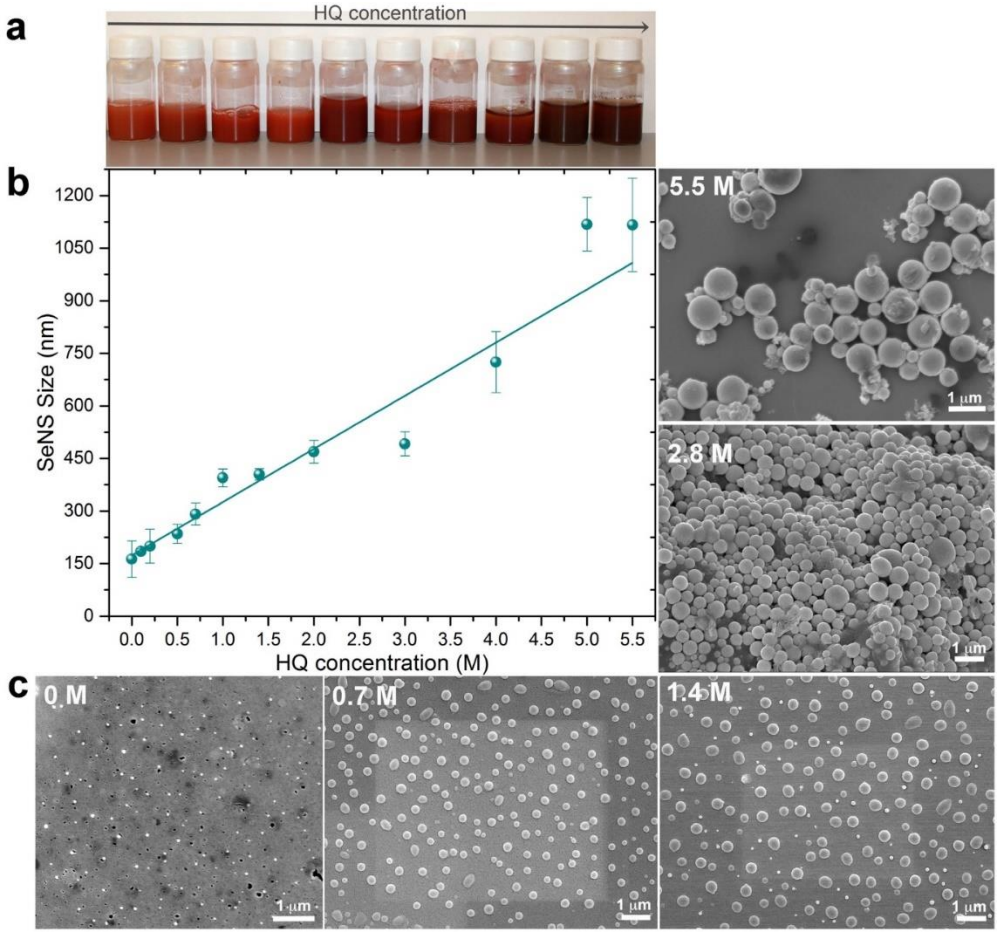

Figure 16. Size control of SeNS grown by the combined hydrothermal/chemical reduction process. (a) Image of the retrieved SeNS obtained from sponges treated with different hydroquinone (HQ) concentrations. (b) Correlation curve of the SeNS size as a function of HQ concentration. (c) SEM images of the corresponding SeNS after retrieval from the sponge and deposition on a silicon substrate.

This is of importance as the catalytic, biological and optical properties of nanoparticles is dependent on their size. Increasing the concentration of HQ in solution resulted in greater reduction and consequently, larger particles on the surface of the sponge. It should be noted that the relationship between HQ concentration and SeNS size is linear with an R^2= 0.93. At concentrations above 3 M, however, the

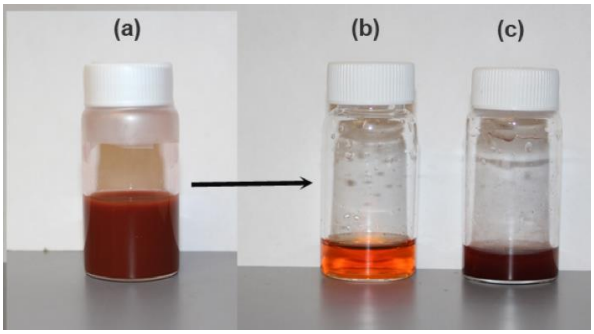

Figure 17. A solution of SeNS obtained with a combined hydrothermal process/chemical reduction at hydroquinone concentration of 5 M (a). The extrusion of solution (a) through a 400 nm filter results in the separation of small SeNS (b) from micrometric SeNS (c).

polydispersity index increases slightly. However, a simple centrifugation or filtration can easily separate the big particles from the rest (**Figure 17**).

When concentrations at 3M and above are not considered the statistical correlation improves slightly (R^2=0.97). This correlation is obtained at an optimum of pH 1.6 for the growth medium. The increase in pH dramatically affects nanoparticle growth and results in low surface coverage (**Figure 18**).

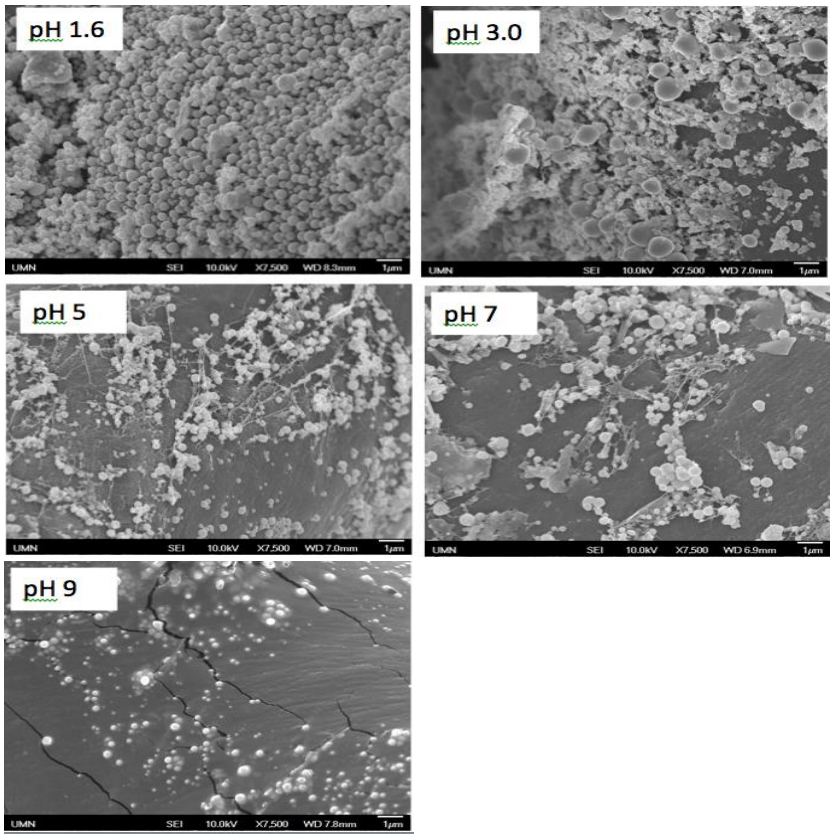

Figure 18. Scanning electron microscope images of sponge-supported growth of at different pH of the growth medium, from pH 1.6 to pH 9.

Since the reduction of selenous acid into elemental selenium also occurs during the hydrothermal process, we have investigated the effect of temperature on the growth and size of SeNS. The SEM images reveal that temperatures of 110-120 ^{o}C represent the optimum conditions for the synthesis of SeNS smaller than 150 nm, without any chemical reduction. A decrease in temperature to 90^{o}C results in the formation of fused nanospheres, while an increase in temperature leads to an increase in nanoparticle size but also in a significant increase in polydispersity (**Figure 19**).

3.3.5 Long-Term Stability of SeNS

The sponge-assisted SeNS exhibited good long-term stability as outlined in **Table 2.** one of the major benefits of the sponge-supported synthesis is that particles can be harvested from the support whenever needed by simple washing with water. Sucrose also promotes stability of the harvested particles as it enters solution when the particles are retrieved from the sponge.

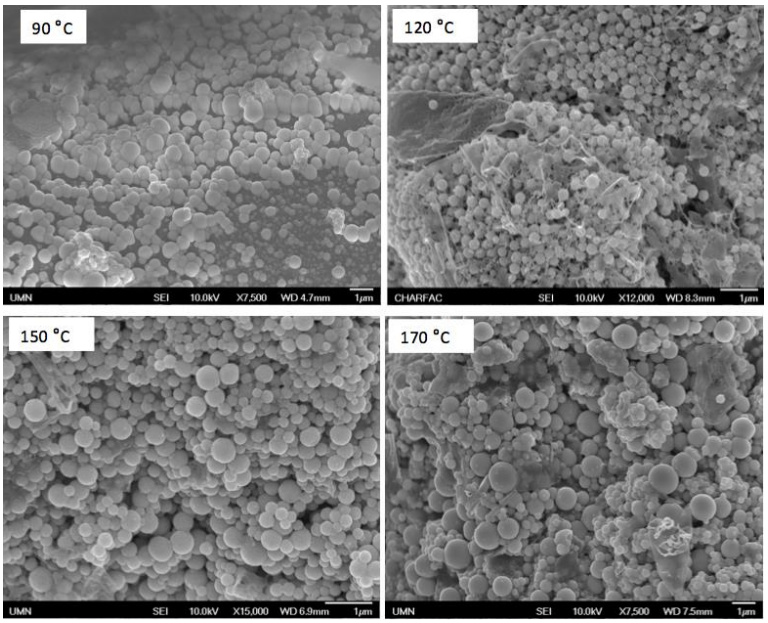

Figure 19. Effect of temperature on the sponge-supported growth of SeNS during the hydrothermal process.

Table 2. Comparison of different synthesis methods of selenium nanospheres

Parameter	**Solution-phase synthesis**(Chen et al., 2009; Gates et al., 2002; Jeong and Xia, 2005; Kumar et al., 2014; Nie et al., 2016),(Shah et al., 2007; Stroyuk et al., 2008; Zhang et al., 2010)	**Microbial-mediated synthesis**(Jain et al., 2015; Oremland et al., 2004; Shirsat et al., 2015)	**Hydrothermal synthesis**(Shin et al., 2007)	**Irradiation- assisted synthesis**(Yu et al., 2016b)	**Sponge-supported synthesis** (this work)
Process time	2 h	12-24 h	N/A	30 min	1 h
Diameter (nm)	5-300 nm	1-500 nm	10-20 nm	5-120 nm	10-1000 nm
PDI	Monodisperse	Polydisperse	Monodisperse	Polydisperse	Monodisperse
Zeta potential	-59 to +59 mV	-25 to +25 mV	-	-	+25 mV
Long term stability at room temperature	1 day to 3 months	Not Published	Not Published	Not Published	> 8 months on the sponge
Structure	Mostly amorphous	Crystalline, amorphous	Crystalline	NA	Crystalline, amorphous

To assess the long-term stability of the SeNS when stored on the sponge, we have compared a SeNS solution obtained from the sponge immediately after synthesis with a SeNS solution obtained from a sponge stored for 8 months (**Table 3**).

The results show that the nanoparticles stored in the sponge for 8 months are remarkably preserved with no change to their size, zeta potential and polydispersity index. The nanoparticle retrieved immediately after synthesis show significant changes in all parameters with noticeable nanoparticle aggregation after 3 months of storage in solution.

Table 3. Comparison of the long-term stability of SeNS after 8 months of storage in the sponge (Sample B) or in solution (Sample C) at room temperature as compared to Sample A (as synthesized SeNS). The results are also compared to the stability of a commercial SeNS solution.

	As synthesized in the sponge	After 8 months in the sponge	After 3 months in solution	As purchased	After 1.5 months
Size (nm)	277± 20 (100%)	291± 26 (96%)	**3,260** (50%) 907 (50%)	565±111 **(6%)** 2,079±768 (14%±7) 139±25 (**50%**) 16±1 (29%)	548±191 (63%) 4,100±2,000 (35 %) 126±1 (2%)
Zeta potential	24 ± 2	26 ± 1	**-17** ± 3	**- 42** ± 1	**88** ± 2
PDI	1.04	1.17	**7.10**	**-**	**-**

More dramatic changes and nanoparticle aggregation are observed for the commercial SeNS after only 1.5 month of storage in solution (**Figure 20**).

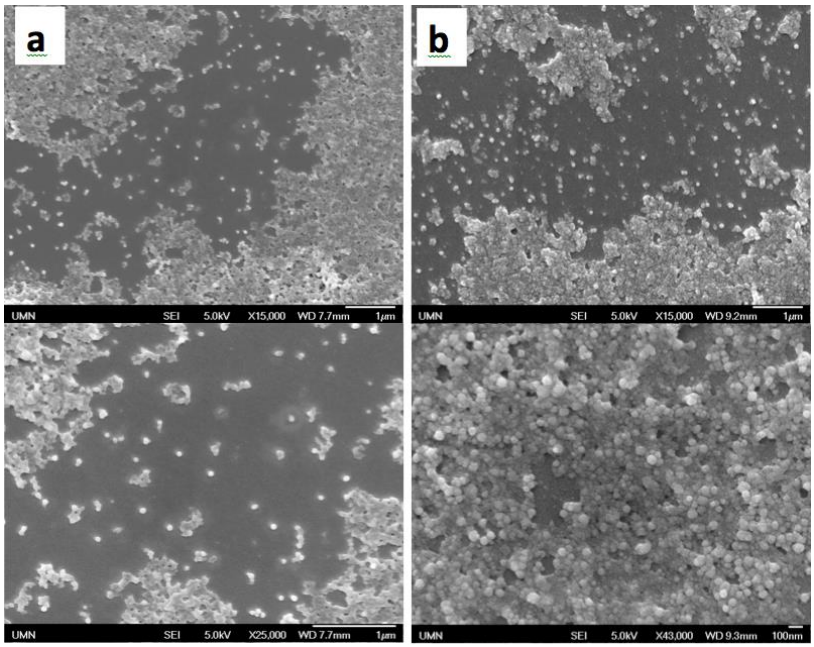

Figure 20. SEM image of commercially available selenium nanospheres. The solution was drop-casted on silicon substrate as it is before (a) and after (b) 1.5 month of storage in solution.

3.3.6 Selenium Nanospheres as Mercury Sorbent

One of the major properties of selenium is its strong interaction and affinity to mercury. To evaluate the ability of selenium nanospheres to sequestrate mercury from water, we mixed SeNS solution with a solution of mercury ions (Hg^{2+}) with different concentrations. The mercury adsorption isotherm showed in **Figure 21** indicates that the adsorption follows a Langmuir model with R^2 equal to 0.94. The adsorbate maximum load or maximum removal capacity of SeNS (Q_e) at equilibrium was calculated from equation 1.

$$Q_e = \frac{C_i - C_f}{m} \times V \qquad \text{Equation 1}$$

Where C_i is the initial concentration of mercury ions in the solution (mg/L), C_f is the final concentration of mercury ions in the solution (mg/L), m is the mass of adsorbent (g), V is the volume of the solution (L), and Q_e is the amount of metal ion adsorbed in milligram per gram of adsorbent at equilibrium (mg/g).

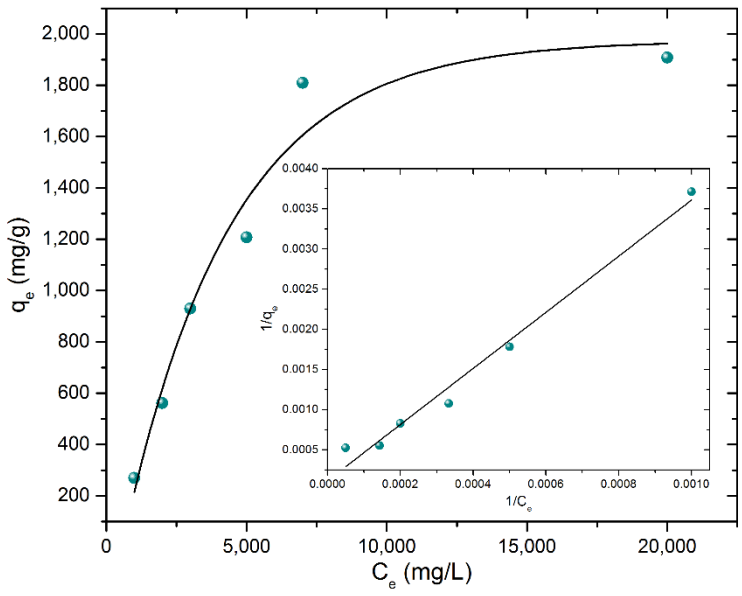

Figure 21. Hg^{2+} adsorption isotherm for selenium nanospheres. The Inset depicts the linear regression obtained by fitting the adsorption isotherm data with the Langmuir adsorption model.

The maximum removal capacity (Q_e) was found to be 1.907 g/g or 1907 mg/g. This value is twice higher than the best results reported for metal-organic frameworks for mercury capture.(Li et al., 2014) In addition, this value means that 74.8 % of selenium atoms interact with mercury (the maximum theoretical load of mercury with a 1:1 stoichiometry is 2540 mg of mercury per gram of selenium), which is a 7-fold improvement as compared to the performance reported in literature for selenium nanoparticles.(Johnson et al., 2008)

The favorability of the interaction between mercury and selenium nanospheres was evaluated by calculating the separation factor (R_L) as indicated in Equation 2.

$$R_L = \frac{1}{1+K_L.C_o} \qquad \text{Equation 2}$$

where the parameter K_L is the Langmuir adsorption constant corresponding to the inverse of the intercept in the linear plot in Figure 21, and C_o refers to initial concentration of adsorbate. The value of R_L was found to be equal to 0.3, which indicates a highly favorable interaction ($0 < R_L < 1$). Values close to zero indicated irreversible interaction, while values above 1 indicates unfavorable interaction. Further studies will focus on analyzing the performance and kinetics of mercury capture by selenium nanospheres in different conditions and their application to environmental and industrial samples.

3.4 CONCLUSIONS

We have introduced a novel method for the concurrent synthesis and storage of colloidal selenium nanospheres directly on a natural honeycomb sponge. The method combines hydrothermal reduction that yields nanoparticles from 10 nm to 150 nm, and a chemical reduction that enables size control of the nanoparticles from 100 nm to 1000 nm. Such control will enable customized production of the desired size to meet the needs of a variety of biomedical, chemical and electronic applications.

Beside the high yield, morphological properties and size tuning over a wide range, the proposed method shows remarkable preservation of nanoparticle properties for over 8 months. Nanoparticle storage and preservation in sponges could represent an alternative to nanoparticle lyophilization that requires cryoprotectants and a time consuming and costly freeze-dry process, or nanoparticle storage in solution using specific coatings or solvents that may interfere with their functionality, functionalization, and biocompatibility. Furthermore, this work report outstanding mercury removal capacity of 1900 mg/g using SeNS, demonstrating the high potential of SeNS as a promising mercury sorbent.

Chapter 4: A Nanoselenium Sponge for Instantaneous Mercury Removal to Undetectable Levels

4.1 Summary

Selective removal of aqueous mercury to levels below 10 $ng.L^{-1}$ or part per trillion (p.p.t) remains an elusive goal for public health and environmental agencies. Here we show that a low-cost nanocomposite sponge prepared by growing selenium (Se) nanomaterials on the surface and throughout the bulk of a polyurethane sponge exhibits an exceptional mercury ion (Hg2+) removal rate, regardless of the pH. The exposure of aqueous solutions containing 10 $mg.L^{-1}$ to 12 $ng.L^{-1}$ Hg2+ to the sponge for a few seconds results in clean water with undetectable mercury levels (detection limit: 0.2 $ng.L^{-1}$). Such performance is far below the acceptable limits in drinking water (2 $\mu g.L^{-1}$), industrial effluents (0.2 $\mu g.L^{-1}$), and the most stringent surface water quality standards (1.3 $ng.L^{-1}$). The sponge shows a unique preference for mercury, does not retain water nutrients, and can significantly reduce the concentration of other heavy metal pollutants. Furthermore, the sponge shows no cytotoxic effect on human cells while exhibiting strong antimicrobial properties. The high affinity of Hg for Se results in irreversible sequestration and detoxification of mercury by the sponge, confirming the suitability for landfill disposal.

4.2. Materials and Methods

All chemicals including selenous acid (98%), sucrose (>99.5%), hydroquinone (99%), tryptic soy broth, tryptic soy agar, yeast mold (YM) broth, YM agar, glutathione peroxidase, nicotinamide adenine dinucleotide phosphate (NADPH), glutathione, sodium azide, hydrogen peroxide, glutathione reductase, and buffers were purchased from Sigma Aldrich (St. Louis, MO, USA). High-density polyurethane (PU) sponges were obtained from a local store. Mercury solution of 1000 mg/L was

purchased from Inorganic ventures AAHG-1. Mercury chloride in solid form was purchased from Sigma Aldrich. All aqueous solutions were prepared in nanopure water. All mercury analyses were done using an atomic absorption spectrometer (Thermo Fischer Scientific iCE 3300, Limit of detection 0.2 $\mu g.L^{-1}$). Mercury samples that showed undetectable levels were sent to the University of Minnesota Research Analytical Laboratory (http://ral.cfans.umn.edu/) and analyzed using a cold vapor atomic fluorescence on a Tekran 2600 (Tekran Instruments Corporation, Limit of detection: 0.2 $ng.L^{-1}$). All mercury analyses referred to in this work are total mercury analyses. For 27 elements analyses, the samples were sent to the same lab and inductively coupled plasma optical emission spectrometry (ICP-OES) was used. Finally, cytotoxicity experiments were performed at the University of Minnesota Institute for Therapeutics Discovery and Development.

4.2.1 Characterization of the polyurethane sponge

The polyurethane sponge was characterized using scanning electron microscopy (SEM) coupled with energy dispersive x-ray analysis (EDX) (JEOL 6500, 6700 SEM) (samples were coated at the characterization facility of University of Minnesota, 10Kev were used), and Fourier transform infrared spectroscopy (Nicollet Series II Magna IR-System FTIR. Average surface roughness and microscopic contact angle were measured using a KLA-Tencor P-7 and an MCA-3 (Kyowa Interface Science Co (Japan)) respectively. Absorption capacity was estimated via water uptake in multiple sponges of uniform size.

4.2.2 Synthesis of selenium nanoparticles on a polyurethane sponge

To obtain a NanoSe sponge with 3 % selenium load, a polyurethane sponge was first soaked in 25% sucrose in nanopure water for 15 min. The sponge was then submerged in a selenous acid solution (1.4 M) for 30 min. After removal of the

sponge the remaining solution was stored at room temperature and used later in the wet chemical synthesis process. The soaked sponge was then carefully removed without squeezing and left in an oven at 100^{o}C (Model SGO1E from Shel Lab) to allow water evaporation, adsorption of selenium on the sponge fibers, reduction of selenium ions to elemental selenium and their subsequent crystallization into selenium nanoparticles of 50-100 nm diameter (growth by a thermal reduction). The time required for complete drying depends on the size and mass of the sponge used, but full drying typically occurred after 2 h. However, it's not needed to dry the sponge completely. Leaving the sponge for 2 min in the oven at 100 ^{o}C was sufficient to initiate the reduction process on the sponge fibers.

Following thermal reduction, the sponge was added to a preheated hydroquinone solution (2.2 M) for 5 min. The remaining selenous acid from the previous step was added to the sponge after exposure to hydroquinone at 65^{o}C to allow further growth of nanoselenium (wet chemical synthesis). The sponge was then quenched in an ice bath for a few minutes and washed with nanopure water to remove excess solution. Quenching the reaction was done to prevent the growth of weakly adhered layers of selenium particles over the primary particles grown directly on the sponge fibers. To obtain a NanoSe sponge with 50 % selenium load, the same procedure was followed with a slight modification involving a change in temperature from 65^{o}C to 75^{o}C.

4.2.3 Cytotoxicity experiments.

Supplemented fibroblast growth medium-2 (FGM-2) media (500 ml, Lonza, Walkersville, MD) was incubated with a NanoSe sponge, bare PU sponge or spent NanoSe sponge (after capture of 10 mg.L^{-1} Hg) at 4^{o}C. Each culture was performed in duplicate making a total of 9 media preparations including a control consisting of

plain medium. Aliquots (10 mL) were taken from each of the 9 media preps at 12, 24, 36 and 48 h and frozen at -20ºC until use. Normal adult human dermal fibroblasts (Lonza) were cultured in supplemented FGM-2 media per supplier's instructions in T-75 flasks at 37ºC, 5 % CO_2. The adherent cells were trypsinized (0.25%) free and washed with FGM-2 medium. Cells (5 x 103) were plated into each well (0.1 mL total volume) of a 96-well plate and returned to 37ºC, 5% CO_2 for different incubation time: 24 h, 48 h and 72 h. After 24 h incubation, the culture medium was removed from each well and replaced with 0.1 ml of fresh FGM-2. Aliquots from the 9 media preparations used for the incubation were thawed and then added to appropriate wells (0.2 mL total volume) to final dilutions of 1/2 (0.5), 1/4 (0.25), 1/8 (0.125) and 1/16 (0.083). The plate was then returned to 37 ºC, 5% CO_2, for an additional 24 h. After the additional 24 h, 0.015 ml 3-(4,5-dimethylthiazol-2-yl)-2,5-diphenyltetrazolium bromide (MTT) dye (CellTiter 96® Non-Radioactive Cell Proliferation Assay, Promega, Madison, WI) was added to each well and the plate was incubated at 37ºC, 5% CO_2. After 1 h, 0.1 ml stop solution was added to each well and the plate was returned to 37ºC, 5% CO_2 for an additional 1 h. The plate was then read in a Molecular Dynamics SpectraMax multi-mode spectrophotometer at 538 nm.

Absorbance units read by the SpectraMax correlate with the number of viable cells present. MTT is reduced by NADPH-dependent oxidoreductase enzymes largely in the cytosolic compartment of the cells and results in the formation of formazan (purple precipitate). Therefore, reduction of MTT and other tetrazolium dyes depends on the cellular metabolic activity due to NADPH flux.

4.2.4 Effect of contact time and adsorption kinetics

Adsorption kinetics experiments were conducted to evaluate the time required to reach the steady state for the removal of Hg by the PU and NanoSe sponges.

Briefly, a sponge (0.3 g) was soaked in 10 mL mercury solution (10 mg/L) for different contact times ranging from 1 s to 3600 s. The solutions were then analyzed for the remaining mercury concentration and the amount of adsorbed mercury. The experimental data were plotted in Figure 25a and linearized following a pseudo-second-order kinetic model.

To evaluate the effect of sponge compression (squeezing) on the sorbent performance, a sponge of 0.6 g was placed in a syringe (BD Biosciences 10mL Leur-Lok Tip). First, the plunger was removed and 2.5 mL of solution containing 10 $mg.L^{-1}$ of mercury was pipetted into the syringe. The plunger was pressed slowly until all the solution was absorbed by the sponge. Upon full absorption, a timer was started until all the solution is removed. After the solution was removed, the timer was stopped and process was repeated until the solution came into contact with sponge again. The process was repeated for each contact time listed above.

4.2.5 Antimicrobial Experiments

The antimicrobial experiments were conducted following the ASTM D2020 protocol. Briefly, spores were harvested from one yeast species (*Candida guilliermondii*) and one mold (*Aspergillus niger*) and ~104 spores were plated on separate potato dextrose agar (PDA) plates. Next, 0.5 cm thick disks were cut from both the NanoSe and PU sponge and autoclaved. Under aseptic conditions the discs were transferred to the plates and incubated at the ideal conditions for each species. Specifically, for Candida guilliermondii the plates were incubated at 25^{o}C for 3 days and for Aspergillus niger the plates were incubated for 5 days at 24^{o}C. Similarly, gram negative bacteria (E. coli spp) and gram positive bacteria (Lactobacillus spp) were diluted to a concentration of 10^5 cells and spread on tryptic soy agar (Lei et al.) plates and MRS agar plates respectively. Again, 0.5 cm thick disks were cut from the

NanoSe sponge and transferred to the plates. The plates were then incubated at 37ºC for 24 h (E. coli spp) and 72 h (Lactobacillus spp).

4.2.6 Effect of pH on mercury adsorption.

The effect of pH on mercury adsorption by the NanoSe sponge was studied by measuring the uptake capacity at different pH conditions. For the experiment, a solution of 10 $mg.L^{-1}$ mercury was prepared from a stock solution of 1000 $mg.L^{-1}$ (Inorganic ventures AAHG-1). Serial dilutions of 50 mL were used to ensure minimal error while preparing dilutions. After preparation of the mercury solution, the pH was adjusted with sodium hydroxide and hydrochloric acid to cover the entire range from 1 to 12. The pH was adjusted using an Accumet AB150 pH meter. The sponges were used as described above for the adsorption kinetics experiment with a contact time of 1 min.

4.2.7 Adsorption isotherm

To study the adsorption behavior of mercury on the sponges, Hg solutions with concentrations ranging from 5000to 35000 $mg.L^{-1}$ were prepared by weighing the desired amount of mercury chloride powder then dissolving it in nanopure water. The pH was then adjusted to 6 in all the samples. Then, 75 mg of the NanoSe or PU sponge was immersed in a vial with 10 mL of the mercury solution. The vials were placed in a rotator (Thermo Scientific Tube Revolver) and mixed for 18 h at 40 rpm. The samples were then analyzed for mercury content as described above.

4.2.8 Application to real-world samples

4.2.8.1 Lake and tap water treatment

To test the efficiency of the NanoSe sponge on real world samples, lake water samples were taken from Como Lake (St. Paul, MN, USA) following the United States Environmental Protection Agency (Stroyuk et al.) Method 1669. For the

sampling, 40 ml VOA EPA certified vials were used. The samples were preserved with 6 M HCl prior to analysis. After collection, lake water and tap water samples were spiked with 12 $ng.L^{-1}$ and 5 $mg.L^{-1}$ of Hg. The spiked solutions were treated with NanoSe sponge and PU sponge with a contact time of 1 min. The samples were then measured for trace mercury.

4.2.8.2 Industrial wastewater treatment

Industrial wastewater released from gold mining activities was provided by an industrial partner. Industrial water without any pre-treatment was used to evaluate the capture efficiency of NanoSe sponge for mercury. Briefly, approximately 0.7 g of NanoSe sponge was placed inside three syringes. Then, 3 mL of industrial wastewater was passed through the syringes with a contact time of about 2 min for each syringe. The procedure used was the same as mentioned in the adsorption kinetics experiment. The same process was performed by using a bare PU sponge. The treated wastewater was then analyzed to determine the concentration of 28 different elements including mercury.

4.2.9 Toxicity of the Se-Hg complex: enzyme activity experiment

To investigate the toxicity of the complex Se-Hg, spent NanoSe sponges (containing 10 $mg.L^{-1}$ Hg) were placed into a 10 mL syringe before being exposed to a glutathione peroxidase (GPx) solution. The enzyme solution was then retrieved and the activity analyzed according to the protocol described by Esworthy et al (Esworthy et al., 2001). Briefly, a volume of 100 µL of 50 U/ml GPx was mixed with 630 µL sodium phosphate buffer (50 mM, pH 7.0), 100 µL glutathione (Qiu et al.) (10 mM), 100 µL NADPH (2 mM), 10 µL sodium azide (1.125 mM), and 10 µL of glutathione reductase (GR) (100 U/mL). The mixed enzyme solution was then added to the sponge in the syringe for a total contact time of 2 minutes. The enzyme solution was

then collected from the sponge. The enzyme reaction was initiated by adding 50 µL of 5 mM H_2O_2 as the enzyme substrate. The decrease in NADPH was measured using a UV spectrophotometer (Shimadzu UV-1800) at 340 nm for 7.5 min and was used to evaluate GPx activity. Control experiments include bare PU sponge, and untreated NanoSe sponge. The enzyme reaction assay was also evaluated after contact with a Hg solution (10 $mg.L^{-1}$) as well as selenium nanoparticle solution. After exposition to Hg or Se solution, the enzyme solution was centrifuged and suspended in buffer before performing kinetic analysis.

4.2.10 Leaching Experiments

The US-EPA methods 1311 and 1312 were used to evaluate the leaching risk of the spend NanoSe. Method 1311, known as the Toxicity Characteristic Leaching Protocol (TCLP), models the leaching behavior of a particular waste material under municipal landfill conditions. Briefly, Hg treated sponges were cut into small pieces with a diameter less the 1 mm and placed in an extraction fluid consisting of glacial acetic acid and sodium hydroxide (pH 4.93). This solution was rotated end over end on a rotator (Thermo Scientific Tube Revolver) at 30 rpm for 18 hours. Next, method 1312, the Synthetic Precipitation Leaching Procedure (SPLP), models leaching characteristics of a waste material in the natural environment under acidic rain conditions. Again, Hg treated sponges were cut into small pieces, added to an extraction fluid (60/40 weight percent sulfuric and nitric acids with pH 4.20) and then rotated for 18 h at 30 rpm. After the 18 h treatment, all solutions were separated from the sponge pieces, acidified to a pH< 2 with nitric acid and analyzed for Hg.

4.2.11 Sorbent Regeneration

In order to assess the recyclability/reusability of the sponges, Hg treated sponges were treated with a variety of regeneration agents. The spend PU and NanoSe

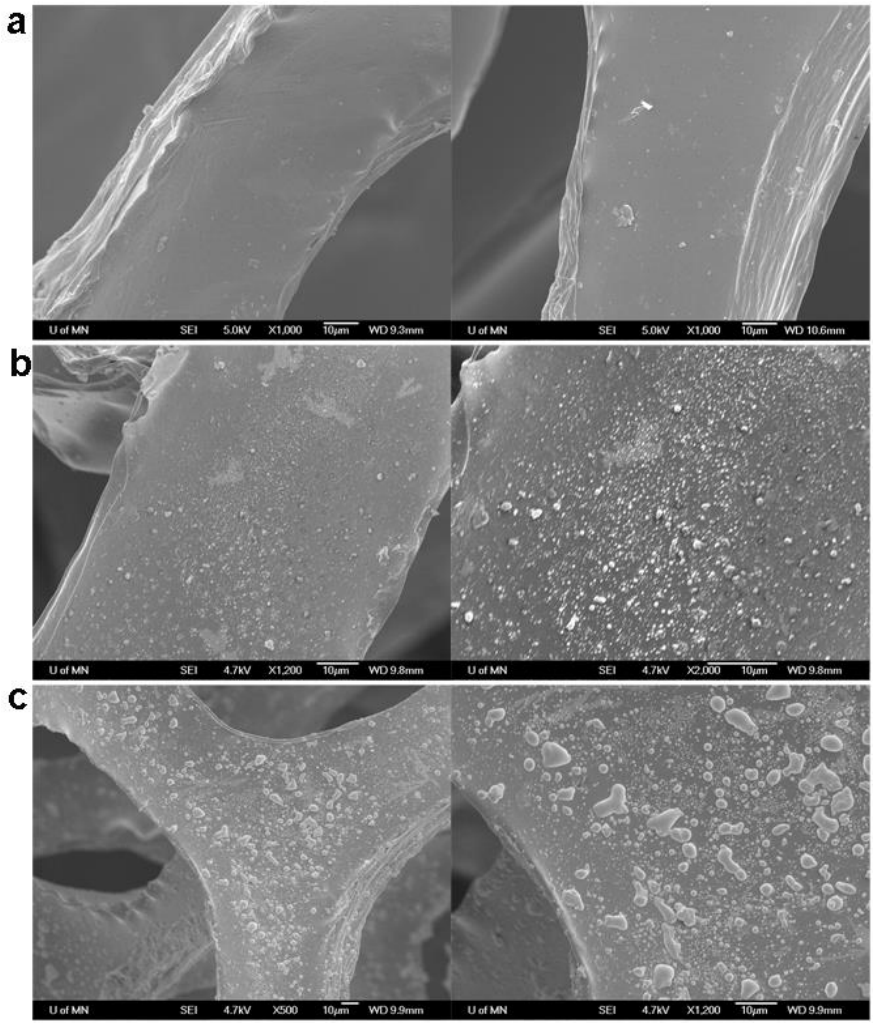

Figure 22. Scanning electron microscopy (SEM) images of PU sponges before (a) and after dip-coating in a solution of pre-synthesized selenium nanoparticles (b), or dip-coating in a solution during the growth of selenium nanoparticle at room temperature. The figures show low coverage, anisotropic nanoparticles and aggregates and inhomogeneous distribution.

sponges (containing 10 mg.L^{-1} Hg) were treated for 1 h in a glass beaker with a 10 mL mixture of 0.25 M thiourea and 1M hydrochloric acid. Additionally, regeneration was attempted under acidic (10 mL 12 M HCl) and basic (10 mL NaOH at pH 12) conditions.

4.3 Results and Discussion

4.3.1. Preparation of NanoSe sponges

Our initial experiments to coat the sponge with selenium nanoparticles were performed by either soaking the sponge in a pre-synthesized SeNP solution (dip-coating) or immersing the sponge in the growth solution during the synthesis

following known protocols (Kumar et al., 2014) As expected, the results depicted in **Figure 22** show a poor and inhomogeneous coverage of the sponge by anisotropic selenium nanoparticles and aggregates.

Additionally, the nanoparticles exhibit high desorption from the sponge after washing. To avoid these drawbacks, we decided to grow selenium nanostructures directly on the sponge fibers by soaking the sponge in selenous acid and then drying it at 100°C to allow both water evaporation and adsorption of the selenium atoms on the sponge, their subsurface diffusion as well as their thermal reduction to elemental selenium. Further growth was initiated by immersing the sponge in hydroquinone solution at 65°C to generate the desired nanostructures including nanoparticles,

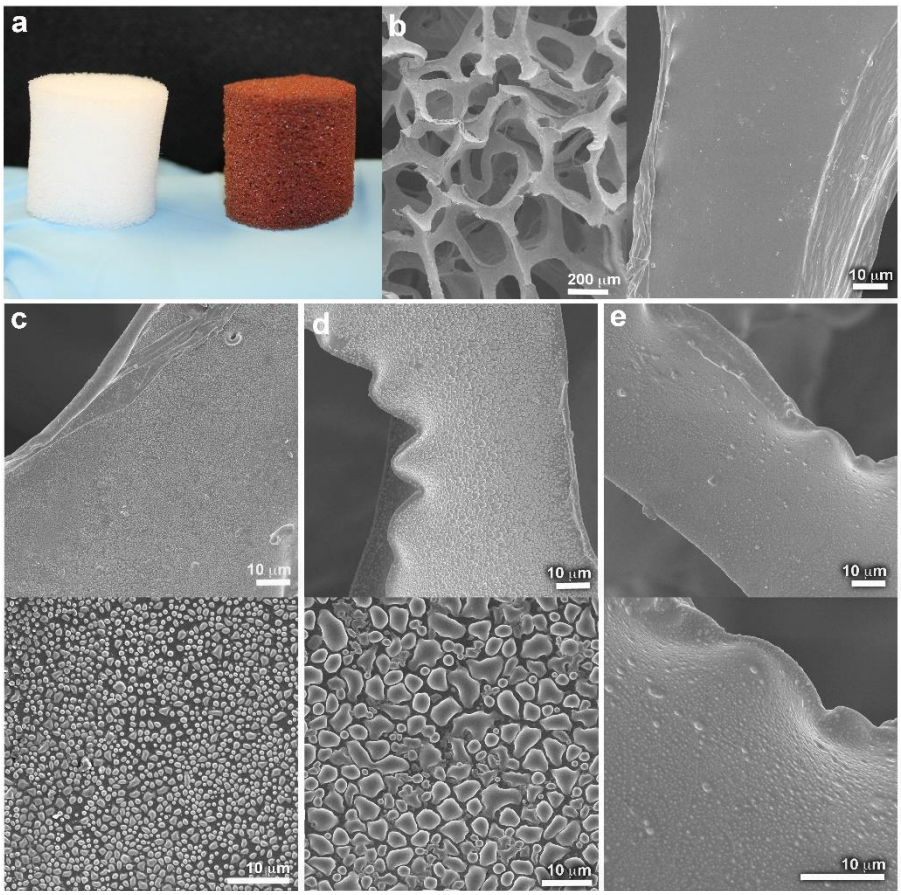

Figure 23. Images of the PU and NanoSe sponges. a) Photography of the PU sponge before (white) and after the growth of nanoselenium (red). b) SEM image of the PU sponge. The NanoSe sponge can contain selenium nanoparticles (c), selenium nanodomes (d) or selenium nanofilms (e).

nanodomes and nanofilms (**Figure 23**).

The variety of morphologies obtained is likely due to the fact that both the thermal and chemical reduction steps occur at temperatures higher than the glass transition temperature of amorphous selenium 31± 0.5°C.(Eisenberg, 1963) At temperatures over 31°C, selenium is in a rubbery state,(Su et al., 2010) and the deformation behavior of amorphous selenium near its glass transition temperature can lead to amorphous domes or thin nanoselenium layers. It should be noted that selenium nanoparticles were successfully grown on other supports, including activated carbon (**Figure 24)**, but these materials were not used due to their failure to retain selenium particles in the support structure, or their inability to maintain

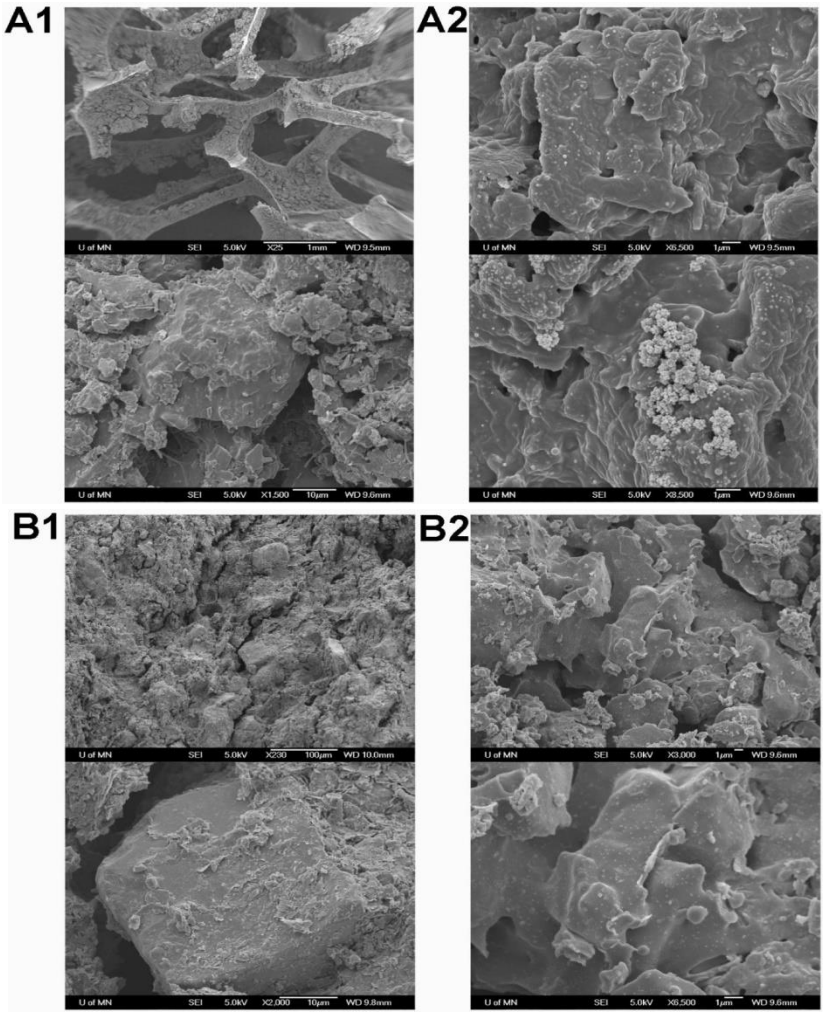

Figure 24. Activated carbon filter without (A1) and with (A2) selenium nanoparticles. Activated carbon pellet without (B1) and with (B2) selenium nanoparticles.

structural stability during the synthesis process.

4.3.2 Adsorption kinetics and isotherm

One of the major parameters of mercury sorbents is the contact time, which largely defines the adequate flow rate for sample cleaning and the subsequent cost of the process. The impact of contact time on Hg^{2+} removal is investigated by immersing the sponge in the mercury solution for a period ranging from 1 s to 60 min (**Figure 25 a, b**). The results show that Hg^{2+} adsorption can reach an equilibrium state after 1 s for the PU sponge with a maximum removal rate of around 84%.

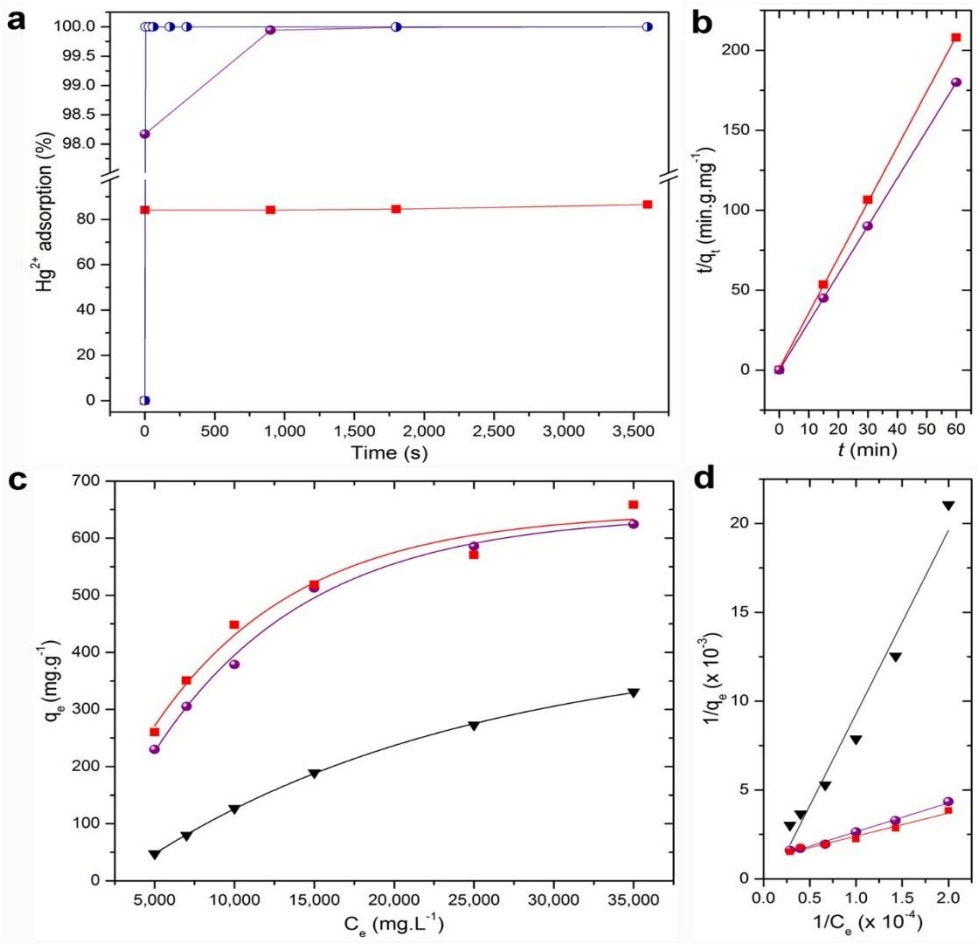

Figure 25. Adsorption process and kinetics for PU and NanoSe sponges. a) Adsorption kinetics of Hg^{2+} by PU (red squares) and NanoSe sponges (purple circles) at an initial Hg^{2+} concentration of 10 mg. L^{-1}. The blue circles represent the kinetics of adsorption by the NanoSe sponge when pressure is applied to the sponge using a syringe. b) Plots of the pseudo-second order kinetics for Hg^{2+} adsorption. The corresponding linear regression of the NanoSe sponge under pressure overlaps with that of the NanoSe sponge (purple). c) Adsorption isotherm of Hg^{2+} for PU and NanoSe sponges, and (d) the corresponding linear regression fitted using the Langmuir adsorption model. The black triangles represent the isotherm of the NanoSe sponge when loaded with 50 % selenium.

Within the same time frame (1 s), the NanoSe sponge removes over 98% of mercury. This rate improves to 99.94% after 15 min and reaches undetectable levels (< 0.2 $ng.L^{-1}$) after 1 hour. When pressure is applied to the sponge by using a syringe or simply squeezing the sponge, removal of mercury to undetectable levels is reached after only 1 to 5 s with a NanoSe sponge loaded with 3% w/w selenium (labeled NanoSe3). The same result is obtained with a NanoSe sponge loaded with 50% w/w selenium (labeled NanoSe50). This remarkable kinetics are due to the high affinity of selenium towards mercury as previously explained. Also, these results suggest that a major limiting factor for Hg^{2+} sorption by the sponge is likely molecular diffusion in the porous structure. Squeezing the sponge generates a pressure gradient and deforms the sorbent structure, thus allowing faster diffusion and enhanced Hg/Se interactions. As a result, the required contact time for mercury removal is dramatically decreased.

The affinity of the NanoSe sponge for mercury can be evaluated by the distribution coefficient (K_d) defined as:

$$K_d = \frac{(C_0 - C_f)}{C_f} \times \frac{V}{m} \qquad (1)$$

where C_0 is the initial Hg^{2+} concentration, C_f is the final equilibrium Hg^{2+} concentration in solution.(Do, 1998) Since the removal rate for NanoSe sponge reaches undetectable levels, the concentration of 0.2 $ng.L^{-1}$ was taken as C_f as it represents the limit of detection of the cold vapor atomic fluorescence equipment used for mercury detection. V is the volume of the solution in mL, and m is the mass of sorbent in g. While the K_d value for the PU sponge is relatively low (1.33×10^2 $mL.g^{-1}$), the value of K_d for NanoSe sponge is 1.67×10^9 $mL.g^{-1}$, two orders of magnitude higher than the best values reported for Hg^{2+} sorbents so far.(Li et al., 2014) Sorbents with K_d around 10^7 $mL.g^{-1}$ are usually considered excellent.

The changes in mercury adsorption over time exhibit an excellent fit with a pseudo-

second-order kinetic model (equation 2), with a correlation coefficient of 0.999 and 1 for the PU and the NanoSe sponge respectively (**Figure 25b**):

$$\frac{t}{q_t} = \frac{1}{k_2 q_e^2} + \frac{t}{q_e} \qquad (2)$$

where q_t (mg. g^{-1}) is the amount of Hg^{2+} adsorbed at time t (min), k_2 (g.mg^{-1}.min^{-1}) is the rate constant of pseudo-second order adsorption, and q_e (mg. g^{-1}) is the amount of adsorbed Hg^{2+} at equilibrium. The rate constants were calculated to be 10.96 g.mg^{-1}.$min^{-1}$and 713.81 g.mg^{-1}.min^{-1} for PU and NanoSe sponge respectively. The extremely high constant rate for NanoSe sponge reveals that the adsorption is two orders of magnitude faster than the one obtained with the state of the art mercury sorbents.(Li et al., 2014)

To determine the adsorption process and the sponge uptake capacity for Hg^{2+} ions, adsorption experiments were performed with initial mercury concentrations ranging from 5000 mg.L^{-1} to 35000 mg.L^{-1} (**Figure 25c**). Linear Langmuir, Freundlich and BET adsorption isotherm models were used to fit the experimental data of Hg^{2+} adsorption. The adsorption isotherm was found to follow a Langmuir model with respective correlation coefficients of 0.97, 0.99, and 0.96 for the PU, NanoSe3 and NanoSe50 sponges (**Figure 25d**). The mercury maximum uptake capacity at equilibrium state was calculated from the mass balance (equation 3).

$$q_e = \frac{C_i - C_f}{m} \times V \qquad (3)$$

Where q_e is the amount of metal ion adsorbed in milligram per gram of adsorbent at equilibrium or maximum uptake capacity (mg.g^{-1}), C_i is the initial concentration of Hg^{2+} in the solution (mg.L^{-1}), C_f is the final concentration of Hg^{2+}in the solution (mg.L^{-1}), m is the mass of adsorbent (g), V is the volume of the solution (L).

The maximum uptake capacity (q_e) was calculated to be respectively 654 mg.g^{-1} and 624 mg.g^{-1} for the PU and NanoSe sponges, which is higher or similar to the best sorbents commercially available. This uptake capacity means that if a lake of the size of a football field and up to 15 feet deep is contaminated with mercury at the US-EPA limit, it would require a sponge the size of a basketball to adsorb all the mercury.

The study of the uptake capacity of PU and NanoSe sponges reveals two major observations. The first is that despite the slow adsorption, the bare PU sponge

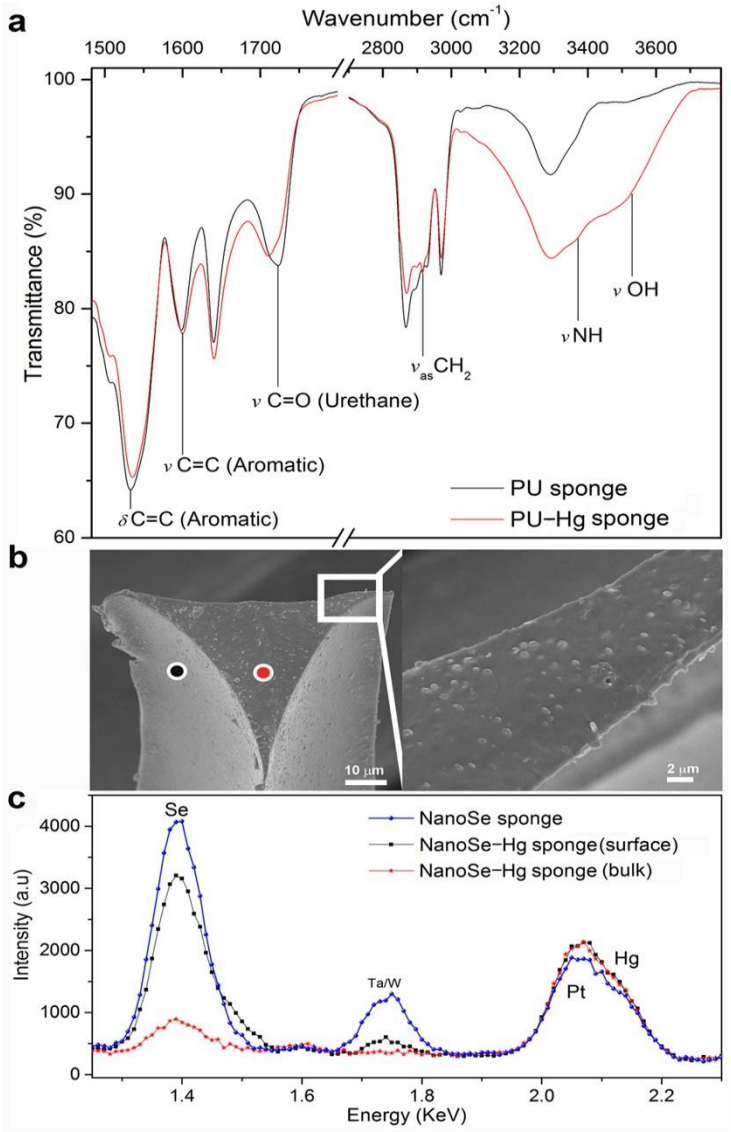

Figure 26. Hg^{2+} binding interactions with the PU and NanoSe sponges. a) FTIR spectra of the PU sponge before and after Hg^{2+} adsorption. b) SEM image of a cross-section of the NanoSe sponge fibers showing internal growth of selenium nanoparticles throughout the bulk material of the PU fiber. The red and black spots show the localization of the energy-dispersive X-ray spectroscopy analysis shown in section (c).

exhibits strong mercury uptake capacity, which is expected as polyurethane is known to capture a wide variety of water contaminants.(Braun and Farag, 1978) Fourier transform infrared spectroscopy (FTIR) analysis showed that PU captures mercury through interaction with its functional groups, including amine, hydroxyl and carbonyl groups (**Fig. 26a**). The FTIR spectra also suggest that the aromatic groups are involved in this adsorption possibly through π-interactions, thus confirming previous reports.(Lannes et al., 2016).

The second observation is that the modification of the size or shape of selenium nanomaterials did not show any noticeable change in uptake capacity, suggesting that the surface-to-volume ratio does not play a major role in the uptake capacity of selenium nanomaterials. This result can be explained by the fact that mercury can undergo subsurface penetration and bulk diffusion to populate internal sites. SEM imaging of the sponge fiber cross-sections reveals that selenous acid penetrates inside the PU sponge fibers resulting in internal growth of selenium nanoparticles (**Figure 26b**).

Energy-dispersive X-ray spectroscopy (EDX) analysis of the same cross-sections confirmed the presence of selenium inside the material but also revealed the presence of mercury, thus confirming bulk diffusion of both Se and Hg (**Figure 26c**). Mercury bulk diffusion can occur inside the PU fibers even when they are coated with a NanoSe thin film, confirming a previous report on Hg diffusion in selenium nanoparticles. The bulk diffusion of Se inside the PU fibers could be enhanced by the relatively high temperatures of the thermal reduction (100^{o}C), and chemiclal reduction (65^{o}C) of nanoselenium. The bulk diffusion of Hg in nanoselenium during water cleaning is likely promoted by the fact that amorphous selenium has a relatively

low glass transition temperature, and thus possesses greater segmental mobility and high diffusivity (Fink, 2013)

Based on these results, we hypothesized that the mercury uptake capacity would be likely more affected by the change in sorbent mass than a change in its surface area. Consequently, increasing the concentration of nanoselenium in the sponge is expected to improve the mercury uptake capacity. To increase the amount of selenium nanomaterials in the sponge, we adjusted the temperature during the chemical synthesis step. We have found that the amount of selenium nanomaterials increases with increasing temperature from 3% w/w (at 65°C) to 50% w/w (at 75°C), which enables a precise control of the selenium content in the sponge.

It is worth noting that the presence of selenium nanomaterials at a concentration of 3% w/w on the PU sponge slightly decreases the uptake capacity as compared to bare PU sponge (**Figure 25c**). To further verify this result, a NanoSe sponge with 50% w/w selenium was produced and tested. As shown previously in Figure 24c, the increase in selenium load from 3% w/w to 50% w/w results in an unexpected, significant drop in the mercury uptake capacity by 50%. A major factor that could explain this drop is that the increase in selenium concentration also results in a significant reduction of the free volume and hence a decrease in the water uptake capacity of the sponge. It can be easily noticed that with 50% Se, the sponge significantly loses its compressibility. In addition, this also means that the bulk diffusion of mercury in selenium is likely limited to a certain depth into the material. From an application standpoint, these results indicate that 3% of selenium in the PU sponge is sufficient to induce extremely rapid adsorption of mercury while maintaining high uptake capacity.

4.3.3 pH Stability, selectivity and application to real-world samples

The implementation of new mercury sorbents to real-world samples such as surface, rain, ground and industrial wastewater requires the sorbent to be stable in different pH conditions and be selective against interfering compounds. The effect of pH on the capture of mercury ions (10 $mg.L^{-1}$) was investigated over a pH range of 1-12. As shown in **Figure 27**, the sponge exhibits optimum performance over the entire pH range.

A close look at the graphic shows that the mercury uptake capacity slightly drops from 100% (undetectable levels) to 99.9% at pH below 1 or higher than 8. This slight variation is likely caused by the ionic strength and does not seem to have any correlation with Hg^{2+} chemical forms in solution as described in literature.(Billinge et al., 2005; Walcarius and Delacôte, 2005) This is due to the fact that nanoselenium

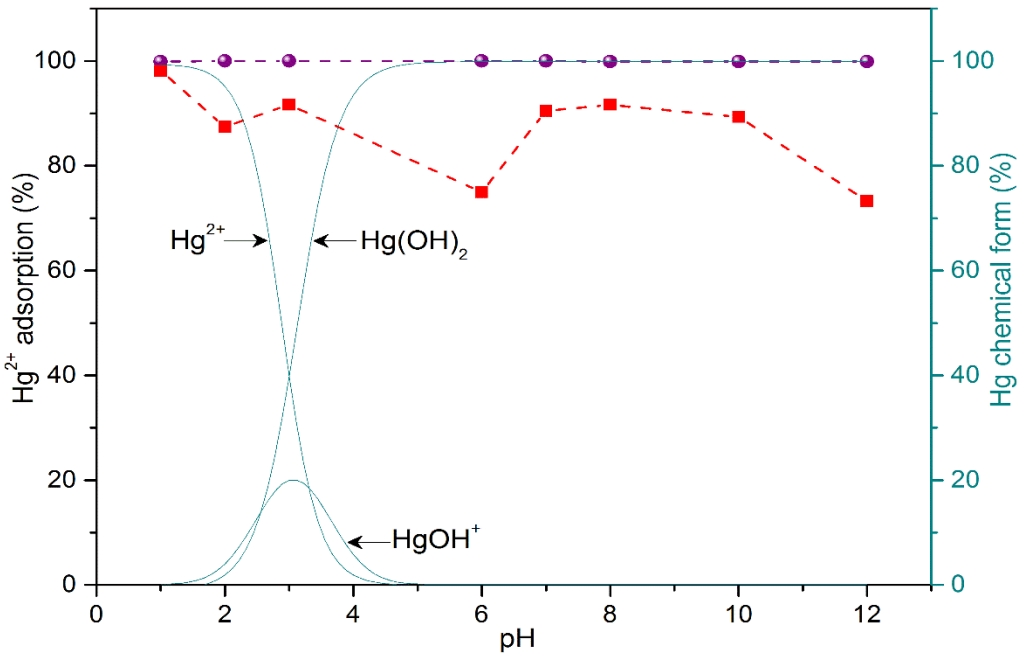

Figure 27. Effect of pH on Hg^{2+} adsorption for PU (red square) and NanoSe (purple circle) sponges. The continuous lines (right axis) show the calculated distribution of the main Hg^{2+} chemical species depending on the pH, reproduced from literature.(Walcarius and Delacôte, 2005)

likely covers most of the polyurethane functional groups, thus becoming more stable. Unlike the NanoSe sponge, a bare PU sponge shows highly variable performance

depending on the pH, due to the presence of multiple negatively and positively charged moieties as shown in **Figure 26a**.

To evaluate the selective affinity of the NanoSe sponge and the effect of interfering ions, we have analyzed the content of tap water and lake water for 20 different chemical elements before and after exposure to the PU and NanoSe sponge for 60 min (**Figure 28**). The results show that both sponges did not retain any water nutrient including P, S, K^{+}, Mg^{2+}, Na^{+} and Ca^{2+}, which is important when treating drinking or surface water.

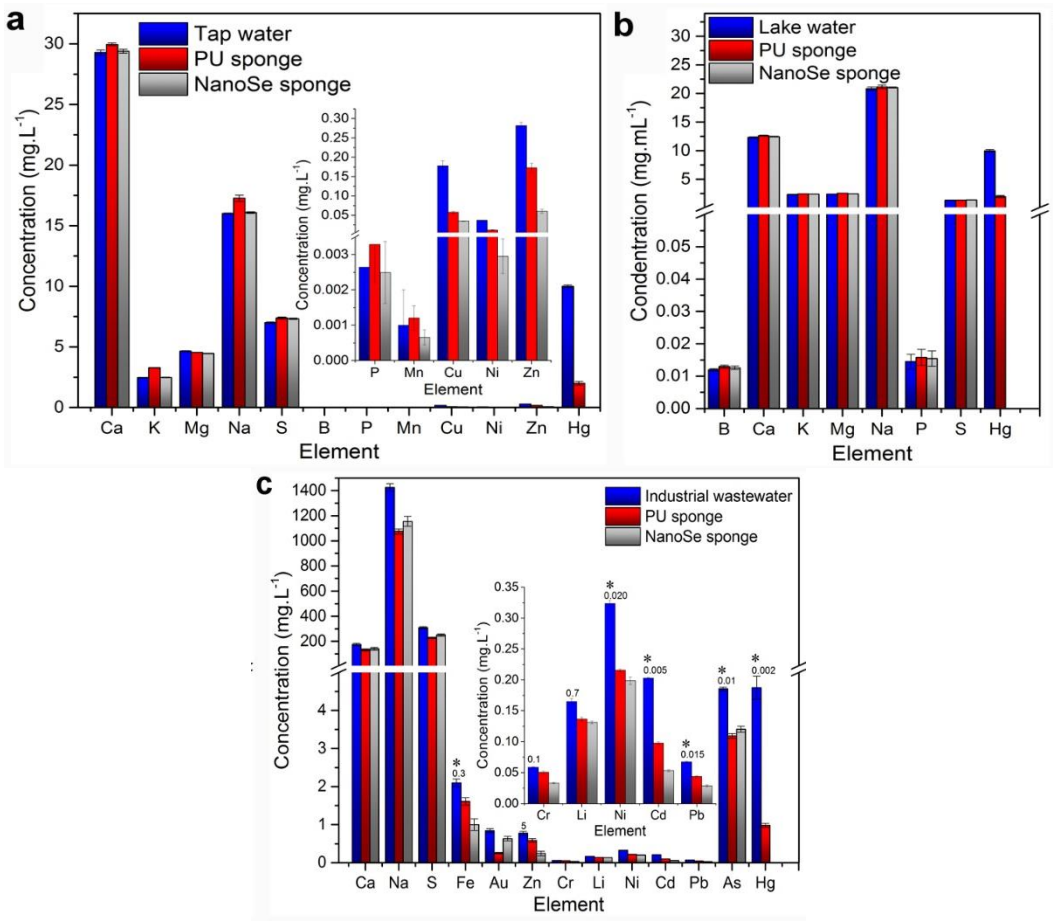

Figure 28. Selectivity of Hg2+ adsorption for PU and NanoSe sponges. The same analysis was performed with drinking water (a) lake water and (b) and industrial wastewater (c) from a mining site. The stars in the diagram (c) indicate that the element is present at concentrations higher than the US-EPA limit, which is provided by a number above the stars. In lake and tap water samples, the sample was spiked with 10 mg.L-1 mercury.

Only three other transition metal pollutants, namely Zn, Cu and Ni showed a significant decrease by 78%, 81% and 90% respectively when using the NanoSe sponge.

It's worth noting here that the mercury removal capacity of the NanoSe sponge was not affected by the presence of these three elements even at extremely low mercury concentrations, showing the high selective affinity towards mercury.

To further demonstrate the applicability of the NanoSe sponge for mercury sequestration in real samples, we have analyzed tap and lake waters spiked with 5 $mg.L^{-1}$ and 12 $ng.L^{-1}$ mercury. Given the ultralow concentrations of mercury used, sample collection, storage and analysis followed ultraclean protocol according to the US-EPA Method 1669. Both samples showed no detectable mercury after treatment with the sponge. The results demonstrate not only the ability to clean environmental samples with no pretreatment, but also the ability to capture extremely low concentrations of aqueous mercury, which opens up new avenues in cleaning rain and surface waters.

The application of the NanoSe sponge for the treatment of industrial wastewater was also evaluated. Wastewater from a mining site was obtained from an industrial partner and analyzed before and after treatment with both the PU and NanoSe sponges. This is a major experiment as industrial wastewater is characterized by a high ionic strength and is usually contaminated by a variety of heavy metals and other pollutants resulting from industrial processes. **Figure 28c** shows the elemental composition of the wastewater before and after treatment with the sponges. The figure focuses on heavy metal contaminants and components that are found at concentrations higher than regulatory limits in drinking water. 10 mL of wastewater was passed through a column containing 0.3 g of either PU or NanoSe sponges without

compression. When using only one sponge column with a contact time of 60 seconds, the PU sponge reduced mercury concentration by 69%, from 4.39 $mg.L^{-1}$ to 1.34 $mg.L^{-1}$, while the NanoSe sponge reduced it by over 80%, from 4.90 $mg.L^{-1}$ to 0.94 $mg.L^{-1}$.

In similar conditions, the treatment of tap and lake water with the NanoSe sponge yielded water with undetectable mercury levels within 5 seconds as seen previously. Unlike drinking and surface water, wastewater treatment showed lower performance due to its high ionic composition. In fact, the concentrations of some cations such as sodium (1,425 $mg.L^{-1}$), potassium (91 $mg.L^{-1}$) and calcium (175 $mg.L^{-1}$) are respectively 100, 32 and 6 times the concentrations found in tap water. In addition, the analyzed wastewater contains a high concentration of sulfur (309 $mg.L^{-1}$) that can potentially compete for mercury capture. It is also contaminated by other toxic pollutants at levels higher than the regulatory standard limits, including arsenic (4.5 $mg.L^{-1}$) which is known to interact with selenium,(Zeng et al., 2005) silver (0.3 $mg.L^{-1}$), and a number of other toxic metals (**Figure 28c**). While the interaction of mercury with selenium is strongly favored over all other interactions, the crowded chemical composition of wastewater will likely reduce the diffusion rate of mercury and slow down the interaction with selenium due to multiple ligand exchange interactions. To overcome this problem, we have treated the wastewater with three columns containing NanoSe sponges and increased the total contact time to 5 min under continuous compression. The results show that mercury concentration was successfully reduced to undetectable levels (below 0.2 $ng.L^{-1}$). In addition to removing mercury, the NanoSe sponge reduces the concentration of other toxic pollutants and contaminants by 20 to 96%, including arsenic (23%), cadmium (73%),

lead (57%), nickel (39%), copper (75%), silver (96 %), zinc (69%), gold (25%), iron (52%), and chromium (43%) (**Figure 28c**).

4.3.4 Cytotoxicity and antimicrobial properties

Antimicrobial properties of selenium are well known and documented.(Phong et al., 2016) This is of major importance when the NanoSe sponge is used in aqueous or humid environments, where biofouling can be a serious problem. To assess the antimicrobial activity of the NanoSe sponge, we have performed antimicrobial experiments by either exposing a microbial plate growth to the sponge or immersing the sponge in the microbial growth solution**.** As shown in **Figure 29a**, the NanoSe

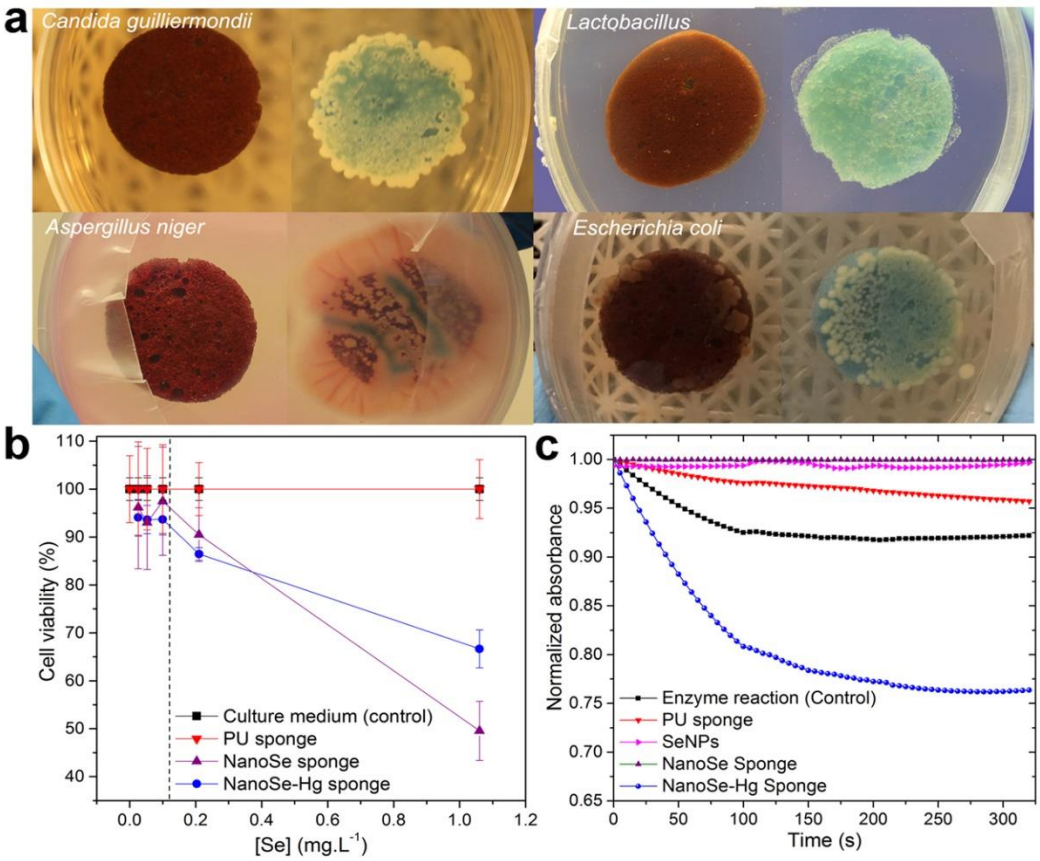

Figure 29. Antimicrobial properties and cytotoxicity of PU (blue) and NanoSe (red) sponges. **a)** antimicrobial tests using molds (*C. guilliermondi*), yeast (*A. niger*), gram-positive bacteria (*Lactobacillus*) and gram-negative bacteria (*E. coli*). For visualization purposes, a blue PU sponge was used in this experiment instead of a white PU sponge.
b) Cytotoxicity of PU and NanoSe sponges on mammalian cells after 72 hours of exposure. **c)** Effect of the PU and NanoSe sponges, SeNPs and NanoSe sponge laded with mercury on the catalytic activity of the enzyme glutathione peroxidase.

sponge exhibits strong antifungal properties against *Aspergilus niger* (mold), *Candica guilliermondii* (yeast) and antibacterial properties against *Lactobacillus*. The growth of *E. coli* seems to be less affected by the NanoSe sponge, in agreement with recent literature.(Phong et al., 2016)

The potential use of the sponge to clean surface waters requires the sponge to be biocompatible and have minimal effect on aquatic life. The NanoSe sponge toxicity could be caused by a potential release of selenium. This risk was studied by exposing a mildly washed sponge to mammalian cells. The sponge was incubated with cell culture medium for 24, 48 and 72 hours. The sponge-exposed medium was then diluted at various concentrations before using it for human fibroblasts cell growth. The diagrams in **Figure 29b** reveals that the sponge has no effect on cell viability when the released selenium concentrations are below 0.1 mg.L^{-1}. The decrease in cell viability becomes noticeable at selenium concentrations of 1.0 mg.L^{-1}

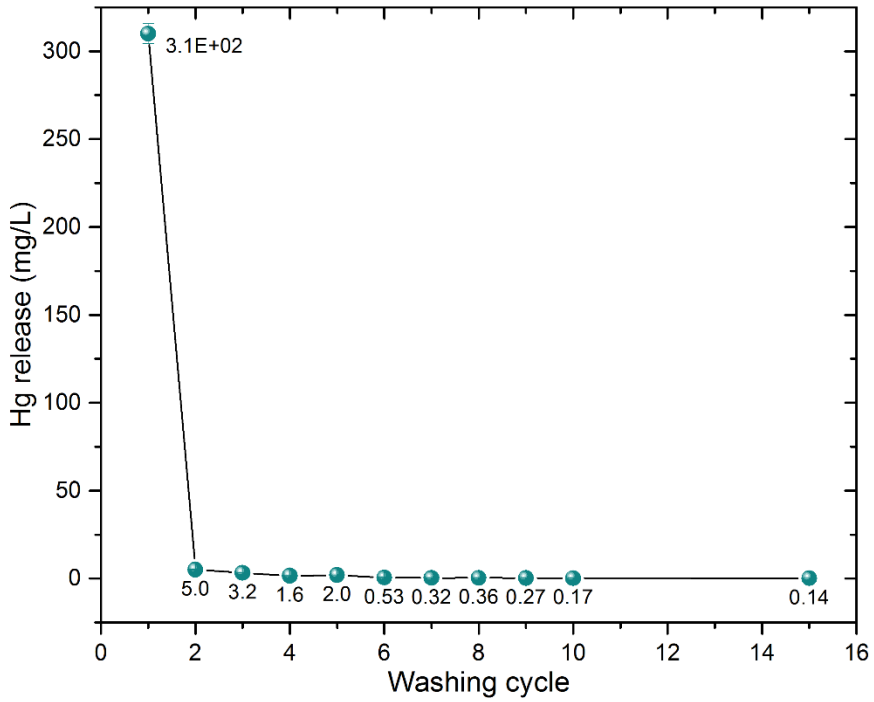

Figure 30. Washing of the NanoSe sponge. After the growth of selenium nanomaterials on the PU sponge, the NanoSe sponge is washed with water. Each washing cycle correspond to immersion of the sponge in nanopure water and hand-squeezing it once. The first washing cycle bring the released selenium down from 300 ppm to 5 ppm. The large release corresponds to the loosely bound selenium nanoparticles that might have grown in solution during the wet chemical synthesis step. The following cycle can reduce the leached selenium to 0.14 ppm, far below the cytotoxic

after exposure for 72 h. The **Figure 30** shows that the sponge can be effectively and easily washed to drop the released selenium concentrations to values around 0.14 $mg.L^{-1}$, below the toxic concentrations.

In addition to the evaluation of the biocompatibility of the NanoSe sponge, we have also investigated the cytotoxicity of the mercury-loaded sponge or specifically of the Se-Hg complex. **Figure 29b** shows that cell viability obtained after exposure to the spent NanoSe sponge (loaded with 10 ppm mercury) is significantly superior to that obtained with an unused NanoSe sponge, indicating that the formation of the complex Se-Hg reduces the cytotoxicity of Se on the fibroblasts rather than increasing it. To confirm the non-toxicity of the Se-Hg complex, we have evaluated the performance of specific enzymes before and after exposure to used NanoSe sponges.

As mentioned earlier, one of the proven routes of mercury poisoning is the irreversible interaction of mercury with biogenic selenium-dependent enzymes such as thioredoxin reductase and glutathione peroxidase.(Branco et al., 2012) **Figure 29c** shows different levels of enzyme activity of glutathione peroxidase following exposure to a PU sponge, and to a NanoSe sponge before and after complexation with mercury. The results show that the activity can be totally inhibited when the enzyme is exposed to selenium nanoparticles (SeNPs) or NanoSe sponge. The PU sponge seems to slow down the reaction but the enzyme remains active. However, when the enzyme is exposed to a NanoSe sponge that was already used to capture 10 $mg.L^{-1}$ of mercury, the enzyme exhibited a remarkable 3-fold increase in activity as compared to the normal enzyme reaction. This result suggests that not only the complex Se-Hg does not have an inhibitory effect, but it may also enhance the enzyme reaction. More work is needed to clarify this unexpected behavior.

4.3.5 Sorbent Regeneration, Leaching and disposal

One of the main questions that newly developed sorbents face is the suitability for regeneration or disposal as this represents a significant factor in determining the final cost of the technology and meeting regulatory requirements. The experiments showed that the sponge releases below 6% of the 10 $mg.L^{-1}$ adsorbed mercury when exposed to harsh chemical treatments conventionally used for sorbent regeneration from mercury, including the use of thiourea and sodium hydroxide,(Liu et al., 2014; Sohrabi, 2014) or 12 M hydrochloric acid.(Li et al., 2014) Detailed results are shown in **Table 4.** These results along with those obtained with the leaching experiments described below demonstrate the irreversibility of the mercury capture by the NanoSe sponge.

Table 4. Regeneration of the spent NanoSe sponge using different chemical treatments.

Treatment	**Adsorbed Hg concentration ($mg.L^{-1}$)**	**Leached Hg concentration ($mg.L^{-1}$)**
12 M HCl for 12 h on NanoSe sponge	10	0.529
12 M HCl for 12 h on PU sponge	10	0.653
0.25 M thiourea, 1 M HCl for 1 h on nSe sponge	10	0
NaOH (pH 12)	10	0.00426

To evaluate the non-hazardous nature of the mercury sponge after use, and the suitability for waste disposal, the leaching risk of the sponge waste was assessed using US-EPA established protocols. Mercury and selenium extraction from waste sponges were performed using both the Toxicity Characteristic Leaching Procedure (TCLP), used to simulate sanitary landfill conditions, and the Synthetic Precipitation Leaching Procedure (SPLP), used to evaluate the leaching potential of land-disposed wastes under acid rainfall. The results show that a sponge loaded with 10 $mg.L^{-1}$ mercury

released only 2 ± 0.2 μg.L^{-1} mercury with both TCLP and SPLP, much below the US-EPA regulatory limits for waste disposal (Maximum Concentration of Contaminants for Toxicity Characteristic) of 200 μg.L^{-1}.

Similar results were obtained for the PU sponge without selenium (**Table 5).** Since the sponge was also loaded with 5 ± 0.5 mg selenium, the leaching experiment was performed on selenium as well. The results show a release of 0.5 mg.L^{-1} Se, which is below the US-EPA limit of 1 mg.L^{-1}. These results indicate that the NanoSe sponge is non-hazardous and can be disposed of by landfilling.

Table 5. Leachability testing of PU and NanoSe sponges using the Toxicity Characteristic Leaching Procedure (TCLP) and Synthetic Precipitation Leaching Procedure (SPLP).

Method	Adsorbed Hg concentration (mg.L^{-1})	Se content in the NanoSe sponge (mg.L^{-1})	Leached Hg concentration (mg.L^{-1})	Leached Se concentration	US-EPA limits (Leachate criterion)
TCLP on NanoSe sponge	10	5.45	0.00229	0.5	Hg: 0.2 mg.L^{-1} Se: 1 mg.L^{-1}
TCLP on PU sponge	10	NA	0.00795	NA	
SPLP on NanoSe sponge	10	4.28	0.00180	0.5	Hg: 0.040 mg.L^{-1} Se: 0.800 mg.L^{-1}
SPLP on PU sponge	10	NA	0.00713	NA	

4.4 Conclusions

This report summarizes the development and evaluation of a nanocomposite (nanoselenium-polyurethane) sponge for instantaneous removal of aqueous mercury to undetectable levels. The new sorbent technology is based on direct growth of selenium nanomaterials on a polyurethane sponge above the glass transition temperature of amorphous selenium. The results suggest that nanoselenium grows not only on the surface of the sponge fibers but also in the bulk material, and that mercury

undergoes subsurface and bulk diffusion to interact with internal sites in the sorbent material, resulting in remarkable removal kinetics, uptake capacity (624 $mg.g^{-1}$) and irreversible mercury binding with a distribution coefficient of 1.67 x 10^9 $mL.g^{-1}$, two orders of magnitude higher than the state of the art mercury sorbents. The sponge shows a promising performance in both removal rate and contact time, by removing mercury from drinking, lake and industrial wastewater to levels below the detection limit (<0.2 $ng.L^{-1}$) within a few seconds to 5 minutes, regardless of the pH conditions.

This is of major importance as it enables wastewater cleaning without pretreatment and with faster effluent flow rates than is currently possible. In addition to removing mercury, the NanoSe sponge significantly reduces the concentration of other toxic heavy metals including lead, arsenic, cadmium, chromium, and copper. The spent sponge containing the complex Se-Hg showed no relevant cytotoxicity towards human fibroblasts and no inhibition of the activity of selenium-dependent enzymes, suggesting that nanoselenium not only captures mercury but also detoxifies it. The demonstrated removal capacity, along with the non-cytotoxicity and antimicrobial properties of the sponge will open new opportunities to clean rain, surface and groundwater and reduce mercury cycling at multiple stages. Since mercury binding to selenium is remarkably strong, the NanoSe sponge cannot be chemically regenerated with conventional treatments, but it can be safely disposed by landfilling after compaction to a small disposal volume.

Chapter 5: Application of Nanomaterials for Food Safety Testing

Apart from the focus of the dissertation. During the Ph.D. studies, I have spent 20% of the time in doing different projects initiated by myself or in collaboration with other team members. Among these projects, I have worked on the use of nanomaterials in food safety. As a result of this work, I co-authored a research article in Nano Letters, "Single Pathogen and Zeptomolar Detection with the Naked Eye using Liposome-Amplified Plasmonic Immunoassay"(Bui et al., 2015) and a review article in Biosensors and Bioelectronics, "Paper-based chemical and biological sensors: Engineering aspects"(Ahmed et al., 2016)

5.1 Summary

We introduce an enzyme-free plasmonic immunoassay with a binary (all-or-none) response. The presence of a single pathogen in the sample results in a chemical cascade reaction leading to a large red-to-dark blue colorimetric shift visible to the naked eye. The immediate and amplified response is initiated by a triggered breakdown of cysteine-loaded nanoliposomes and subsequent aggregation of plasmonic gold nanoparticles. Our approach enabled visual detection of a single-digit live pathogen of Salmonella, Listeria and E.coli O157 in water and food samples. Furthermore, the assay allowed a naked-eye detection of target antibody concentrations as low as 6.7 attomolar (600 molecules in 150 μL); 6 orders of magnitude lower than conventional Enzyme-Linked ImmunoSorbent Assay (ELISA).

5.2 Introduction

The ability to detect a single pathogen with the naked eye remains an elusive goal with broad implications in food safety, biodefense and clinical diagnostics at the early stage of infection. Current technologies rely on sample enrichment via cell

culture or nucleic acid-based tests.(Cho et al., 2014; Pollok et al., 2015) For a large number of diagnostic applications in food safety, biodefense and healthcare, the primary need is to determine the presence or absence of a pathogen or toxin in the sample regardless of its concentration. When a single *Listeria*, human immunodeficiency virus, anthrax or ricin molecule is detected, adequate treatment or preventive response will be immediately implemented with no prior need for quantification. When quantification is not the major requirement, then immunoassays can be designed so that they provide a maximum response to any concentration of the target analyte down to a single pathogen, herein referred to as binary or all-or-none response immunoassays.

Various immunoassay solutions have been proposed to overcome the picomolar limit of detection (LOD) of ELISA.(Lequin, 2005; Swierczewska et al., 2012) Although these assays achieved LOD ranging from the femtomolar (10^{-15} M) to the attomolar (10^{-18} M),(Chen et al., 2011; de la Rica and Stevens, 2013; Kosaka et al., 2014; Rissin et al., 2010) they often require spectroscopic equipment or imaging systems for detection and thus lose the benefit of naked-eye readout offered by ELISA. To enable visual detection of ultralow concentrations with colorimetric assays, a number of strategies have been proposed over the last few years. The best results have been achieved using plasmonic colorimetry, where the color generation is caused by the change in the optical properties (absorbance) of plasmonic nanostructures such as gold or silver nanoparticles.(Anker et al., 2008) The change in absorbance, *i.e.* color, of the nanoparticle solution can be caused by a modification of their size, shape, distribution or metal composition.(Willets and Van Duyne, 2007) In 2011, Qu et al. achieved a LOD of 150 fM (10^{-15} M) of human immunodeficiency virus by using antibody-conjugated CuO nanoparticles in a sandwich immunoassay,

and by inducing the aggregation of gold nanoparticles using Cu-catalyzed click chemistry.(Qu et al., 2011) The next year, the detection limit was further improved beyond the attomolar level (10^{-18} M) by de la Rica et al., demonstrated by the detection of a viral protein and a cancer biomarker.(de la Rica and Stevens, 2012) In their approach, de la Rica et al. used catalase as a biocatalytic enzyme in a conventional ELISA setting to affect the crystal growth of gold nanoparticles (AuNPs), thus inducing a color change in the solution. Although it achieved remarkable detection limits, this method is limited by the chemical instability of hydrogen peroxide in solution and by the dependence on enzyme kinetics, which requires up to 1 h for the generation of the colorimetric signal.

Here, we report an enzyme-free colorimetric immunoassay that pushes the LOD with the naked eye to the attomolar level (10^{-18} M) with instantaneous signal generation and amplification and a clearly defined color shift. The assay demonstrates for the first time a naked eye detection of a single-digit bacteria in food samples, thus overcoming the need of extensive cell culture and plating. This approach builds on our previous work on understanding and controlling AuNPs aggregation using molecular cross linkers,(Abbas et al., 2013; Abbas et al., 2012; Gandra et al., 2012) and on recent advancement in preparing and using loaded liposomes for a variety of applications including drug delivery and enzyme catalysis.(Aili et al., 2010; Lichtenberg and Barenholz, 2006; Ngo et al., 2008; Tabaei et al., 2013) In order to achieve single-digit pathogen detection capabilities with colorimetric tests, we have combined plasmonic colorimetry with a novel molecular signal amplification leading to a Liposome-Amplified Plasmonic Immunoassay (LAPIA) shown in **Figure 31**.

Traditionally, immunoassays begin by capturing the target pathogen on a solid surface using specific antibodies in a sandwich immunocomplex format. In ELISA

methods, the immunocomplex is conjugated to an enzyme that catalyzes either a chromogenic substrate (conventional ELISA),(Swierczewska et al., 2012) or a substrate that affects the growth of gold nanoparticles (plasmonic ELISA).(de la Rica and Stevens, 2012) In our approach, no enzyme is needed. The immunocomplex is directly labeled with cysteine-loaded liposomes (Cys-liposome) using a biotin-streptavidin linkage. AuNPs solution is then added to the assay, followed by the addition of a hydrolysis agent or a buffered surfactant such as PBST (1X PBS buffer with Tween-20 0.05%). In the presence of a pathogen, the surfactant induces immediate hydrolysis of the liposomes, leading to the release of encapsulated cysteine molecules. Due to their high affinity to gold surface, the thiol groups of cysteine will bind to the nanoparticles, while the free amine and carboxyl groups bind to other cysteine molecules via intermolecular hydrogen bond. The amine groups can also directly interact with the gold surface.(Acres et al., 2014) By playing the role of a crosslinker, cysteine induces rapid aggregation of AuNPs. Since assembled nanoparticles exhibit light absorbance at higher wavelengths, the aggregation is reflected by a rapid and highly distinctive color shift of the solution from red to dark-blue, which allows naked-eye assessment. The significance of the color shift depends on the degree of nanoparticle aggregation, which in turn depends on the concentration of cysteine crosslinkers(Abbas et al., 2013).

The main challenge was then to design a reaction system in which the presence of a single pathogen induces maximum aggregation of the nanoparticles. This is achieved by two major features of the LAPIA test: first, the detection mechanism is not limited by enzyme kinetics since no enzyme is used here, and second, each specific antibody is labeled via biotin-streptavidin linkage with one liposome. Each liposome of around 100 nm diameter could contain millions of

cysteine molecules. Using liposomes of 400 nm can further increase this number. However, 100 nm liposomes are used here due to their superior stability in solution, minimum fusion and better encapsulation efficiency.(Sabın et al., 2006; Winterhalter and Lasic, 1993).

5.3 Materials and Methods

Gold (III) chloride trihydrate, trisodium citrate dehydrate, sodium phosphate saline buffer (PBS), Chloroform, bovine serum albumin (BSA), rabbit IgG serum, Anti-rabbit IgG and streptavidin were purchased from Sigma-Aldrich (USA), L-cysteine was obtained from Research Products International Corp. (USA). L-α-phosphatidylcholine and modified phosphoethanolamine were acquired from Avanti

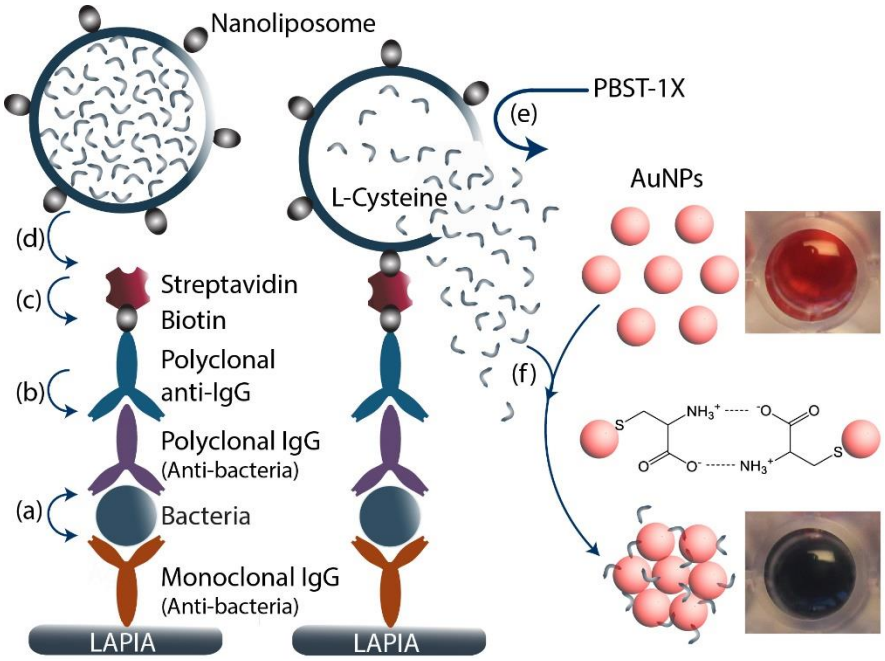

Figure 31. Schematic of the Liposome-Enhanced Nanoparticle Aggregation Immunoassay (LAPIA). One bacterium, molecule or antigen can rapidly trigger a chemical cascade leading to a chromogenic aggregation of AuNPs. The reaction proceeds in different steps: **(a)** Capture of the target (biomarker, pathogen, toxin) using sandwich immunoassay, (**b**) After washing steps, biotinylated secondary antibody (polyclonal anti-IgG) is allowed to interact with the immunocomplex. (**c**) After incubation and washing, streptavidin is added to interact and bind to biotinylated IgG, (**d**) After washing steps, Biotin-conjugated Liposomes containing cysteine are added to the medium followed by AuNPs solution, **(e)** Addition of PBS-Tween 1X to the medium causes the breakdown of the liposomes and the release of cysteine, leading to immediate aggregation of gold nanoparticles and color shift from red to dark-blue (**f**).

Polar Lipids (USA). 20X PBS Tween-20 solution was purchased from Thermo Scientific Inc. (USA) and diluted to 1X concentration containing 10 mM PBS with 0.05% Tween-20 (PBST 1X). Uranyl acetate is obtained from Ted Pella Inc. (USA).

5.3.1 Preparation of the bacterial suspensions

Three foodborne pathogens: *Escherichia coli* O157:H7 (American Type Culture Collection, (ATCC) 43895), *Salmonella typhimurium* (ATCC14028S), and *Listeria monocytogenes* Scott A (ATCC 19115) strains were used as sample model and pathogen manipulation is performed in biosafety laboratory level 2 (BSL-2). The cultures were stored at -80°C in tryptic soy broth (TSB) (Neogen, USA) with 10% (w/v) glycerol until use. The strains were stroked on tryptic soy agar (TSA) (Neogen, USA) media and incubated overnight. These plates were then used to inoculate TSB broth overnight. The suspensions were adjusted to 0.2 absorbance units at 600 nm using Genesys Visible Spectrophotometer 20 (Thermo Scientific Spectronic, USA). The suspension was then decimally diluted to different concentrations in physiological saline solution (0.85% NaCl, pH7.2 ± 0.2). The concentration of different diluted suspensions was confirmed by plating on five TSA plates (200 µl per each) and incubating 24 hours before counting the number of colonies.

5.3.2 Preparation of cysteine-loaded liposomes (Cys-liposome and Cys-liposome-biotin)

L-cysteine-loaded liposomes were prepared using a reverse-phase evaporation method (An et al., 2009; Gomes et al., 2006; Roberts et al., 1996). Briefly, 5 mg of L-α-phosphotidylcholine was dissolved in 1 mL chloroform solution. The solvent was evaporated to form a thin layer of PC under nitrogen flow and vacuum for 15 min to ensure complete evaporation. The obtained thin film of PC was rehydrated with 5 mL of 50 mM L-cysteine solution in nanopure water to obtain 1 mg/mL final

concentration of liposomes. Multilamellar liposomes were formed by whirling until the solution became cloudy and sonicated for 1 min at room temperature. The vesicular solution was then passed through a 100 nm, 200 nm or 400 nm polycarbonate filter using a mini-extruder (Avanti Inc., USA) to produce homogenous suspensions of uniform liposome size. Liposome solution was later dialyzed with nanopure water to remove any non-encapsulated cysteine molecules using a dialysis cassette (G2, 3,500 MWCO, Thermo Scientific Inc.) for at least 1.5 hours. The final solution was stored at 4^{o}C until use. Produced liposomes can be stable for 2–3 weeks at 4^{o}C.

The preparation of Cys-liposome-biotin was performed using a mixture of L-α-phosphotidylcholine (PC), cholesterol, and phosphoethanolamine-conjugated biotin (PE-PEG2000-biotin) with a molar ratio of 70:10:20 respectively, was dissolved in a chloroform solution. The obtained thin film after solvent evaporation was dissolved in cysteine solution as previously described to obtain a final concentration of 1 mg/mL liposome suspension. The rest of the procedure is similar to the one used for the Cys-liposomes. The physical characteristics (size, zeta potential) of the produced liposomes and synthesized gold nanoparticles are determined using dynamic light scattering particle analyzer and Stabino particle charge titration analyzer (from Microtrac, USA).

5.3.3 Synthesis of gold nanoparticles (AuNPs)

All glassware used for AuNPs synthesis were cleaned in Nochromix solution followed by Aqua Regia (3 parts HCL + 1 part HNO_3) according to a standard laboratory procedure. The synthesis of citrate-stabilized gold nanoparticles (AuNPs) was based on a modification of Turkevich's method(Enustun and Turkevich, 1963; Grabar et al., 1995; Turkevich et al., 1951). Briefly, 100 mL solution of 1 mM

HAuCl4 was boiled under stirring and uniform temperature until the formation of bubbles is observed. The solution was then heated for another 25 min. Then, 10 mL of preheated trisodium citrate (38.8 mM) was quickly added to the boiling HAuCl4 solution. During this process, the solution turns colorless for a moment followed by a transition from violet to dark ruby/red. The solution was heated for another 5 min before cooling down to room temperature. The final reddish solution of AuNPs was stored at room temperature and covered with aluminum foil. The size of AuNPs was characterized to be 3212 ± 25 nm in diameter using transmission electron microscopy (TEM, FEI Technai T12).

5.3.4 Sandwich LAPIA test for the detection of rabbit IgG

The experimental schematic for sandwich LAPIA testing was illustrated in Figure 31. A Sarstedt flat-bottom microtest plate 96-well (Sarstedt Inc., USA) was coated with 150 µL of goat anti-rabbit IgG (5 µg/mL) in carbonate buffer (pH 9.6) and stored overnight at 4^{o}C. The plate was then washed 3 times with washing buffer (1X PBS Tween-20) before exposition to a blocking buffer (5% BSA in 10 mM PBS buffer, pH 7.4) for 2 h at room temperature, followed by washing 3 times using a washing buffer. After plate coating with antibodies, 150 µL of each diluted polyclonal rabbit IgG solution (from 6.7 x 10-7 M to 6.7 x 10-18 M) was transferred to the plate according to plate layout and incubated for 1h at room temperature.

After washing 3 more times, 100 µL of biotinylated polyclonal anti-rabbit IgG diluted in 1% PBS-BSA buffer solution was transferred to the plate and incubated for 1h at room temperature. Similar to the previous step, the plate was washed 3 times followed by the addition of 100 µL streptavidin solution (1.25 µg/mL) diluted in 1% PBS-BSA buffer at pH 7.4. The plate was incubated for another 30 min at room temperature, and then washed twice with washing buffer, and twice with 10 mM PBS

(pH 7.4) to remove any remaining Tween-20 in the plate. The plate was then incubated for 30 min at room temperature with 50 µL of Cys-liposome-biotin solution diluted in PBS buffer at pH 7.4. After incubation, the plate was gently washed twice by adding 150 µL PBS buffer (10 mM, pH 7.4) to each well in order to remove the non-bound or weakly bound liposomes.

After washing the plate, 100 µL of AuNPs solution at pH 7.25 was added to each well followed by the addition of 15–20 µL of 1X PBST buffer (pH 7.4). Color change from red to dark-blue can be immediately observed in a positive sample. Quantitative analysis of the color shift is realized by reading optical density (OD) values at 655 nm using a microplate reader (iMark, Bio-Rad, USA) and by UV-visible spectroscopy (Shimadzu 1800 spectrophotometer) to evaluate the aggregation degree (%). The aggregation degree is represented by the ratio of the peak area of the absorption band at 650 nm (caused by aggregated AuNPs) and the band at 520 nm caused by single AuNPs. While microplate readers are convenient for conventional ELISA based on enzyme colorimetry and substrate absorbance at a single wavelength, plasmonic colorimetry is more accurately monitored by UV-visible absorption spectrometry. This is due to the fact that the absorption band maximum caused by AuNPs aggregation shifts towards higher wavelengths (from 600 nm to around 650 nm) during the aggregation process. This dynamic change of the aggregation degree can only be recorded by a spectrometer with wavelength scanning.

5.3.5 Conventional sandwich ELISA for the detection of rabbit IgG

The procedure for conventional ELISA was performed in a similar manner to LAPIA method with the use of streptavidin conjugated horseradish peroxidase (STV-HRP) enzyme (Thermo Scientific Inc.). The biocatalysis of the substrate, 3,3’,5,5’-teramethylbenzidine (TMB) into a colored product was detected using microplate

reader at 450 nm. The color generated by TMB substrate is initially blue, and then turns yellow after adding the stop solution.

5.3.6 Sandwich LAPIA test for the detection of foodborne pathogens

Three live pathogens, Escherichia coli O157:H7, Salmonella typhimurium, and Listeria monocytogenes, were used as models for the LAPIA immunoassay. Bacterial suspensions were diluted to different concentrations in physiological saline solution. 96-well polystyrene plates (Sarstedt Inc., USA) were modified with 100 µL goat anti-mouse IgG antibodies (Fc specific), and diluted to concentration of 3 µg/mL in carbonate buffer (100 mM, pH 9.6). After washing three times with washing buffer, the plates were blocked with blocking buffer (5% BSA in 10 mM PBS buffer, pH 7.4) for 2 h at room temperature. Then, 100 µL (2 µg/mL) of mouse monoclonal anti-E.coli O157:H7, anti-Salmonella typhimurium, or anti-Listeria monocytogenes (Abcam, USA) was added and incubated for 1 h at room temperature or overnight at 4ºC. After washing again three times, different pathogen suspensions were diluted in 1% PBS-BSA at pH 7.4 with a volume ratio of 1:1, and then added to the plate.

After 1 h incubation at 37ºC and washing three times, 100 µL of polyclonal anti-E. coli O157 (2 µg/mL), anti-Salmonella an anti-Listeria (4 µg/mL), diluted in blocking buffer, was added to the plates and incubated for 1 hour at 37ºC. The plates were then washed three times and 100 µL of biotinylated IgG diluted 1:1000 in blocking buffer, was added and incubated for 1 hour at 37ºC. After another washing cycle, 100 µL (2 µg/mL) of streptavidin in blocking buffer was added and incubated for another 30 min at room temperature. Then, the plates were washed twice with washing buffer, and twice with 10 mM PBS, pH 7.4 to remove any Tween 20 remaining in the plate. The plates were then incubated with 50 µL of Cys-liposome-biotin solution (diluted to 1:1 volume ratio in PBS buffer, pH 7.4) for 30 min at room

temperature. After a final washing cycle with PBS buffer to remove the non-bound liposomes, colorimetric detection was performed following the same procedure previously described for IgG detection with AuNPs aggregation.

5.3.7 Detection of foodborne pathogens in food samples

To study the impact of food matrices on the detection of pathogens using LAPIA test, selected food samples were exposed to known concentrations of a specific foodborne bacterium. Briefly, milk and apple juice were used as purchased and were respectively inoculated with E.coli and Salmonela. Ground beef (25g) was mixed in 25 mL PBS buffer at pH 7.4, and then the suspension was filtered through polycarbonate membrane (0.2 µm) and the filtered solution inoculated with Listeria before use. All food samples were exposed to known concentrations of pathogens, which were later determined by cell plating in 1% diluted PBS-BSA buffer solution, with a volume ratio of 5:5:2 for bacterial suspension, food matrix, and diluted buffer solution respectively. The LAPIA test was performed using the same procedure mentioned previously.

5.4 Results and Discussion

5.4.1 Optimization of the assay

In order to translate this new concept into a working colorimetric assay, we first studied the effect of the different assay components on nanoparticle aggregation and determined the optimum conditions for a stable assay mixture. These conditions ensure that AuNPs aggregation (color shift) is only caused by the presence of the target analyte or pathogen and not by any other side reaction or component present in the assay. Since the stability of AuNPs greatly depends on their zeta potential and the pH of the solution, we have prepared mixtures of AuNPs and Cys-liposome at different pH values in order to identify the optimum pH range for LAPIA tests. The

synthesized AuNPs solution exhibits a pH of 5.9 and the mixture of AuNPs with Cys-liposome yields a pH of 6.2 with a zeta potential of -60 mV. **Figure 32a** shows that spontaneous aggregation of AuNPs is observed when pH of AuNPs is below 6.5 and quickly reaches maximum aggregation at pH 4.9 since the ionic strength changed the liposome conformation and its stability.(Sułkowski et al., 2005; Yin and Faustman, 1993) Above pH 6.5, AuNPs remain stable. A control containing the same mixture without cysteine did not yield any aggregation, indicating that low pH caused hydrolysis of the liposomes and the release of cysteine thus causing the aggregation.

As a result, we determined the optimum pH of the mixture in LAPIA test to be in the range of 7.0-8.5, which also corresponds to the pH range where cysteine is mostly in a zwitterionic state (**Figure 33**). Therefore, the pH of the synthesized AuNPs has to be adjusted to the optimum range before use. For instance, when AuNPs solution is adjusted to pH 7.25, the assay mixture shows a very high stability and only the hydrolysis of Cys-liposome by PBST leads to aggregation (**Figure 32b**). The transmission electron micrographs in **Figure 32c and 32d** and **Figure 33** confirm the breakdown of the liposomes by PBST and the subsequent aggregation of AuNPs by cysteine crosslinkers. This aggregation results in the appearance of a second band between 600 nm and 700 nm in the UV-visible absorption spectra of the nanoparticles, which explains the color shift from red to dark-blue (**Figure 32e)**.

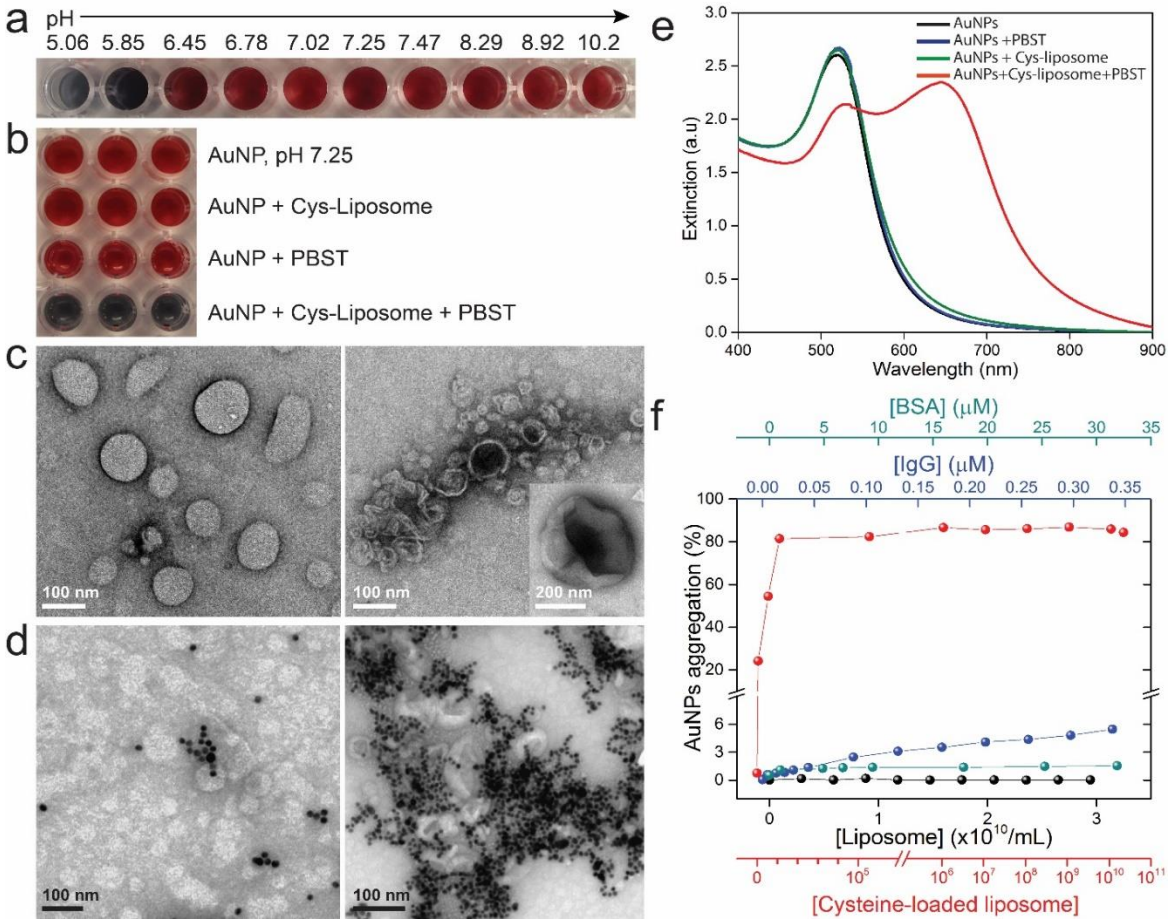

Figure 32. Characterization and optimization of the LAPIA test. **(a)** Optical photograph of AuNPs aggregation at different pH values in the presence of cysteine-loaded liposomes (Cys-liposomes) without PBST. The mixture is stable at pH > 6.7. **b)** Photograph showing the aggregation of AuNPs upon introduction of PBST 1X. The PBST breaks liposomes and releases cysteine resulting in total aggregation of AuNPs and visible color change from red to dark blue. The addition of PBST without Cys-liposomes does not cause aggregation. **(c)** TEM images of intact liposomes (left) and lysed liposomes after exposition to PBST (right). The Inset shows a higher magnification image of Cys-liposome after hydrolysis by PBST. **(d)** TEM images of AuNPs (pH 7.25) with Cys-liposome solution, before (left) and after (right) adding PBST. **(e)** UV-vis absorption spectra of single AuNPs in the absence and presence of Cys-liposome and PBST solution (black, blue, green). Single AuNPs are characterized by a single absorption peak at around 520 nm. The addition of PBST caused the appearance of a second band between 600 and 700 nm with a maximum at around 650 nm, characteristic of aggregated or assembled nanoparticles. **(f)** Effect of BSA, IgG and non-loaded liposomes on the stability of AuNPs. At concentrations used in typical bioassays, the aggregation is less than 2%. The addition of Cys-liposome and PBST cause total AuNPs aggregation (>80%), regardless of the concentration of the liposomes. The number of Cys-liposomes plotted in the graphic is the number needed to cause the aggregation of 100 μL AuNPs solution.

Since the proteins used in a typical immunoassay can also cause aggregation of AuNPs to some extent, we investigated the effect of different concentrations of IgG and BSA, used respectively as a recognition element and a blocking agent. The experiment was performed at pH 7.5 in a mixture containing AuNPs, Cys-liposome and the protein of interest. Figure 32f shows that BSA has negligible effect on AuNPs stability even at high concentrations, while IgG proteins cause a very low aggregation (<1%) at the usual concentrations used in immunoassays (< 5 µg/mL).

Once the optimum conditions for the assay stability have been determined, we conducted measurements to evaluate the minimum number of liposomes required to induce maximum nanoparticle aggregation. AuNPs solution was mixed with variable concentrations of Cys-liposome, and PBST was added to trigger cysteine release, followed by UV-visible absorption spectroscopy and optical density (OD) measurement to estimate AuNPs aggregation.

The results indicate that around 1000 Cys-liposomes are sufficient to cause a visible aggregation of 25% of 100 µL AuNPs, which is still significantly higher than the background signal (< 1%) (**Figure 32f and Figure 34)**. Although each antigen-

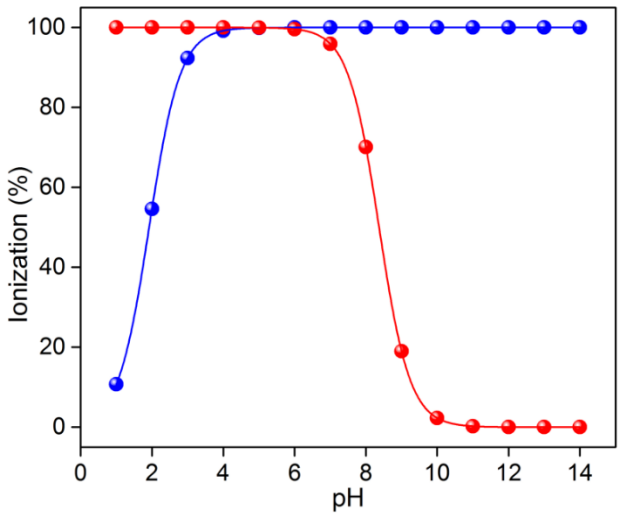

Figure 33. Effect of pH on the ionization degree (%) of L-cysteine in water, based on its acidic (pK1 = 1.92) and basic (pK2 = 8.37) pKa values.

antibody immunocomplex can be labeled via biotin-streptavidin linkage with up to 3 liposomes (streptavidin has 4 binding sites for biotin), it is unlikely that more than one liposome will bind to the immunocomplex due to steric hindrance. As a result, the LOD with the naked eye (nLOD) is expected to be around 17 aM. Such performance also means that a single-digit pathogens that would normally bind multiple liposomes through different epitopes would be able to cause significant aggregation and visible colorimetric shift. These predictions will be evaluated through the detection of IgG and three major foodborne pathogens.

To confirm the unprecedented sensitivity of the LAPIA concept and the ability to provide all-or-none response at the attomolar level, rabbit IgG is used as a target analyte in a sandwich immunoassay on a 96-well microtest plate (**Figure 35a and 35b**). Cys-liposomes were prepared with biotin-functionalized lipids to enable their binding to biotin-labeled antibodies via streptavidin molecules as described earlier.

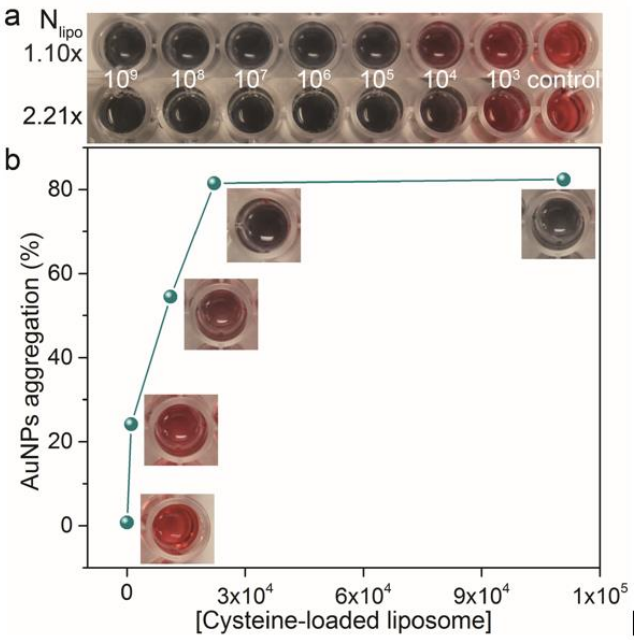

Figure 34. (a) Optical photograph of LAPIA test showing the effect of different concentrations of Cys-liposome on the aggregation of AuNPs. Liposome hydrolysis was caused by adding 20 µL PBST solution. (b) Correlation plot showing the aggregation degree as a function of Cys-liposome concentration. The number of Cys-liposome was calculated based on their hydrodynamic diameter size and lipid concentration as mentioned above. AuNPs solution, adjusted to pH 7.25 using NaOH 0.5 M and 100 µL was added to each well followed by 40 µL of biotinylated Cys-liposome.

The results show that visible colorimetric shift is obtained for all concentrations down to 6.7 aM, corresponding to around 600 IgG molecules in each microwell of 150 µL, which is in agreement with the expected LOD from **Figure 34**. The slight difference between the experimental value (6.7 aM) and the theoretical one (17 aM) is likely due the difficulties related to evaluating the exact number of liposomes in solution, which is used to calculate the theoretical value.

To optimize the conditions of the IgG detection, the experiment was also performed using different liposome sizes (100 nm and 200 nm) (**Figure 35b**). The results reveal similar reactions for the 100 and 200 nm liposomes, with the 100 nm liposomes exhibiting a slightly better performance. Larger liposomes (400 nm) showed fluctuating and less reproducible colorimetric changes. This unexpected result could be explained by the fact that smaller liposomes offer less steric hindrance

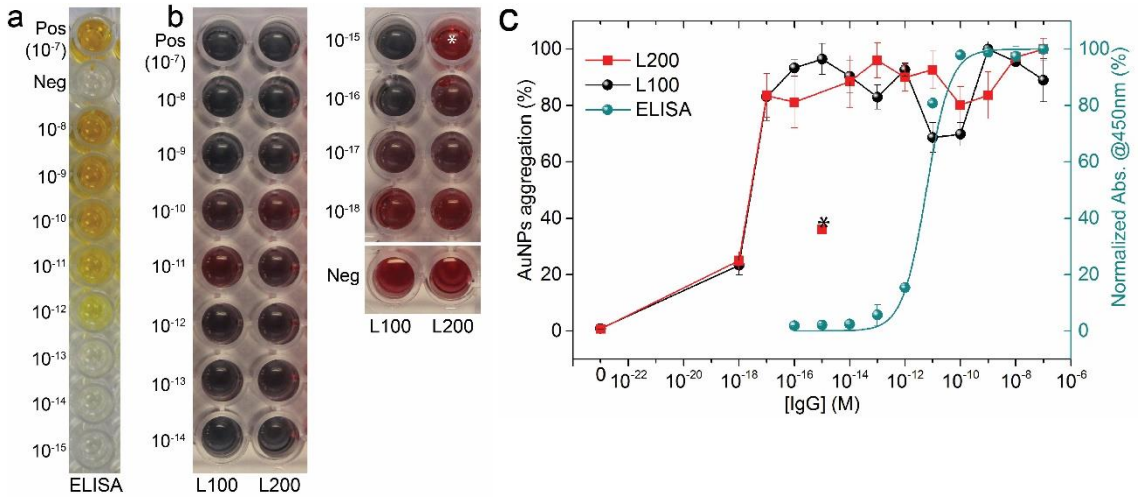

Figure 35. Naked-eye detection of rabbit IgG proteins at different concentrations. **(a)** Conventional ELISA. The yellow color is caused by the biocatalysis of 3',5,5'-tetramethyl-benzidine (TMB) by Horseradish peroxidase enzymes. The detection limit is at the picomolar level (10^{-12} M). **(b)** LAPIA test. The assay was performed using 100 nm (L100) and 200 nm (L200) liposomes. All tests showed maximum color shift from red to dark blue at extremely low concentrations down to 6.7 x 10^{-17} M. A concentration of 6.7 x 10^{-18} causes 25 % aggregation and can still be distinguished from the control. **(c)** Comparison of the colorimetric response of conventional ELISA and LAPIA tests at different target IgG concentrations. The percentile of AuNPs aggregation in LAPIA test is represented with respect to negative control by measuring the optical density at 655 nm. The colorimetric signal of ELISA was recorded at 450 nm. The microwell and corresponding data point indicated with a star represent a false negative. Neg: negative control, Pos: positive control. The concentrations are indicated in molarity (M).

and more flexibility for liposome interaction with the streptavidin-labeled antibodies.

Also, the 400 nm liposomes are likely less stable as revealed by the change in the zeta potential from -36 mV to -26 mV (**Table 6**). These results also suggest that the cysteine concentration encapsulated in 100 nm liposomes is sufficient to induce significant AuNPs aggregation at the attomolar level.

Table 6. Characteristics of the produced liposomes and AuNPs, as measured by dynamic light scattering and TEM, respectively.

Sample	Particle size (nm)	Zeta potential (mV)	pH
AuNPs	12 ± 2	-68.1	5.9
Liposome-cysteine-PEG-biotin (100 nm)	82 ± 20	-36	4.0
Liposome-cysteine-PEG-biotin (200 nm)	242 ± 10	-30	3.9
Liposome-cysteine-PEG-biotin (400 nm)	355 ± 18	-26	4.1

Hence, 100 nm liposomes have been used in the following experiments. It should be worth noticed that the washing conditions (washing buffer, washing pressure) could strongly influence on the final results of LAPIA as well as steric hindrance of larger liposomes.

5.4.2. Test on real-world samples

The demonstration of live pathogen detection with the LAPIA test was performed on three of the most common pathogenic foodborne bacteria, namely *Escherichia coli* O157:H7, *Salmonella typhimurium*, and *Listeria monocytogenes*.

The microbial suspensions were diluted to different concentrations down to single-digit bacteria (**Figure 36a and 36b**). As expected, all bacterial concentrations yielded a maximum colorimetric shift demonstrating a binary or all-or-none response. For ultralow concentrations of 3±1 bacteria per mL, the whole volume of 3 mL from the final dilution is used for cell plating (1 mL) and for the LAPIA test (2 mL). Each 1 mL sample was diluted in 1% PBS-BSA buffer and distributed on 8 microwells of 250 µL each. **Figure 36b** reveals that only 1 to 3 microwells showed maximum colorimetric shift, with each well containing 1 to 2 bacteria, in agreement with the number of bacteria found in the corresponding cell culture plate.

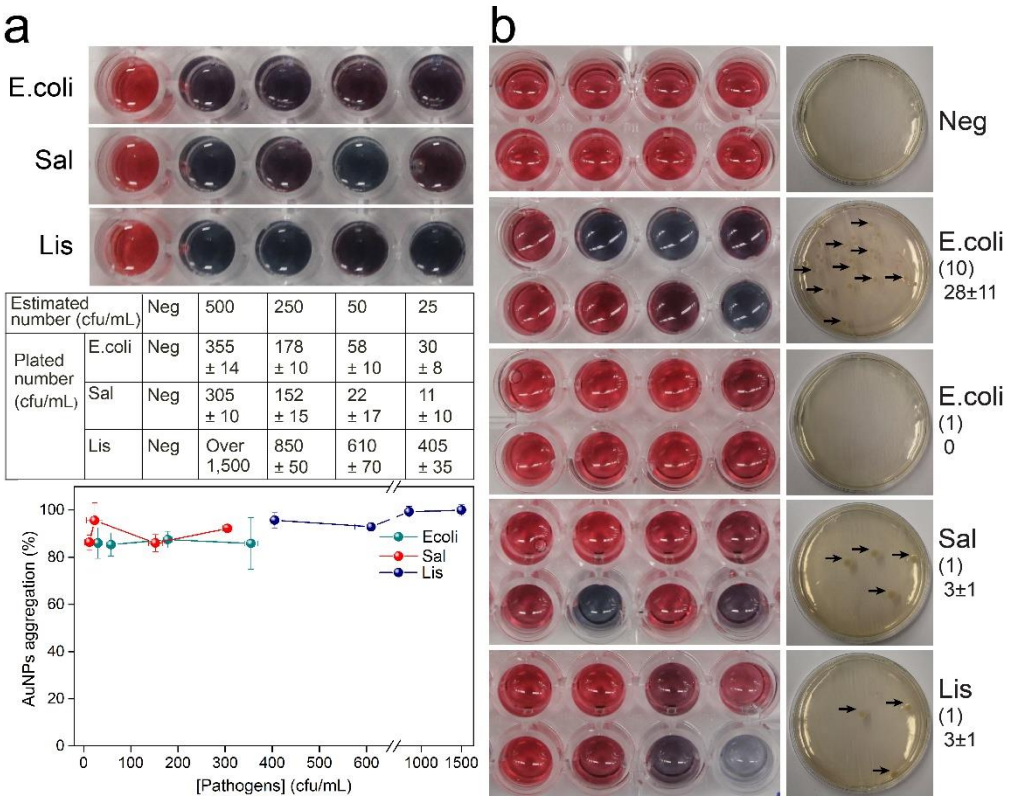

Estimated number (cfu/mL)		Neg	500	250	50	25
Plated number (cfu/mL)	E.coli	Neg	355 ± 14	178 ± 10	58 ± 10	30 ± 8
	Sal	Neg	305 ± 10	152 ± 15	22 ± 17	11 ± 10
	Lis	Neg	Over 1,500	850 ± 50	610 ± 70	405 ± 35

Figure 36. **(a)** Naked-eye detection of foodborne bacteria using LAPIA concept. Optical photographs of LAPIA plates for the detection of *Escherichia coli* O157:H7, *Salmonella typhimurium*, and *Listeria monocytogenes*, labeled respectively E.coli, Sal and Lis (top). The bacteria were diluted and detected in water at different concentrations. The table represents the estimated and counted number of bacteria using cell plating (middle). The graphic shows all-or-none response for all concentrations with maximum aggregation of AuNPs (absorbance measured at 655 nm) (bottom). **(b)** LAPIA test detection of foodborne pathogens at single-digit numbers (left) which was confirmed with cell plating (right). At low bacteria numbers (<4 bacteria), only 2 to 3 out of 8 microwells showed positive response, indicating the detection of 1 or 2 bacteria in each well. The estimated (bracketed) and plated bacteria numbers showed consistent results with the LAPIA test

This experiment demonstrates the naked eye detection of a single-digit pathogens in all-or-none response mode. The visible aggregation of AuNPs in the presence of a single-digit pathogens is due not only to the fact that each bacterium can bind multiple Cys-liposomes, but also the accumulation of liposomes in a small volume around the bacterium results in increased local concentration of released cysteine, which causes rapid aggregation of the surrounding AuNPs.

This initial and local aggregation induces a change in the zeta potential of the solution leading to more nanoparticle instability and aggregation without the involvement of cysteine molecules. The detection of the foodborne pathogenic bacteria was performed again by preparing three microtest plates. Each plate was functionalized with antibodies specific to one bacterium, and then exposed to a sample containing the two other bacteria. **Figure 37** shows the absence of colorimetric change indicating the high selectivity of the assay and absence of cross-reactivity.

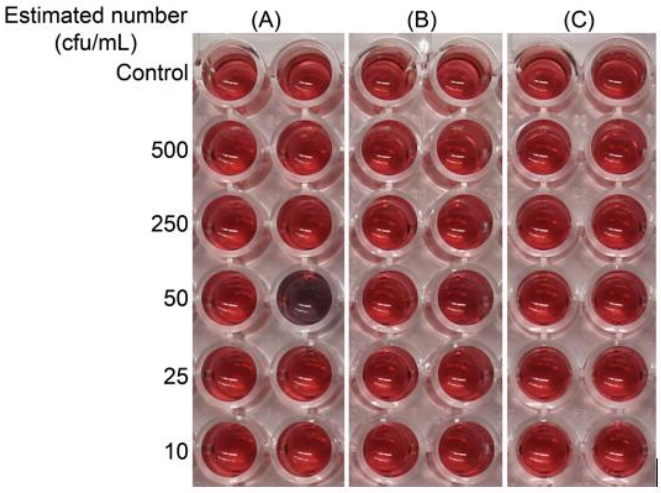

Figure 37. Optical images of LAPIA plate showing the cross-reactivity in the detection of foodborne bacteria. Three microplates were coated with monoclonal anti-*E.coli* (A), anti-*Salmonella* (B) and anti-*Listeria* (C). After the washing step, different concentrations of foodborne bacteria suspensions diluted in PBS-BSA 1% buffer solution, were added to the microplates. Specifically, *Salmonella typhimurium*, *Listeria monocytogenes* and *E.coli* O157:H7, were respectively incubated in microplates A, B and C. The detection was performed as previously described. The results clearly show high selectivity and absence of cross-reactivity on in the LAPIA test (the "blue spot" in (A) showed the false positive result in the LAPIA test).

To further confirm the detection abilities of the assay in real-world samples, the same pathogens, *i.e. E.coli*, *Salmonella* and *Listeria* were respectively detected at different concentrations in milk, ground beef and apple juice with no prior treatment of the sample as shown in **Figure 38**.

5.5 Conclusion

In conclusion, we have demonstrated a naked-eye detection of a single-digit pathogens using plasmonic colorimetry of gold nanoparticles combined with signal amplification via cysteine-loaded liposomes. The lowest analyte concentration analyzed and detected with a visible color shift is 6.7 attomolar, which is the lowest reported naked eye LOD without using enzymes or visualization equipment. Concentrations higher than 67 attomolar can be detected with a maximum colorimetric shift indicating an all or none response. As proposed here, the assay is suitable for analytical and diagnostic purposes where a binary (Yes or No) response is

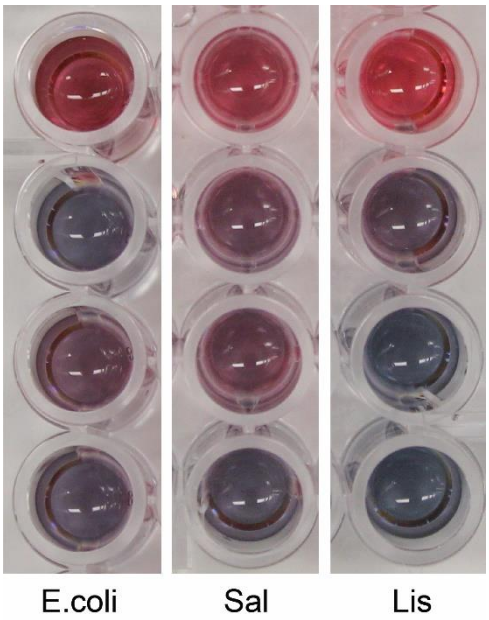

Samples	Pathogens concentration (Estimated:Plated)		
E.coli in milk	1000:2073 (± 37)	100:203 (± 32)	10:28 (± 11)
Sal in apple juice	1000:1880 (± 57)	100:157 (± 24)	10:16 (± 8)
Lis in ground beef	1000:1960 (± 23)	100:250 (± 14)	10:65 (± 8)

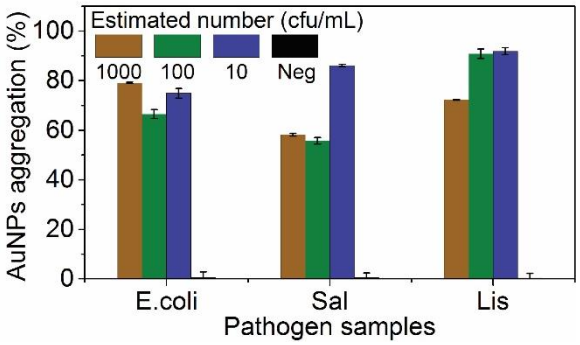

Figure 38. LAPIA test for the detection of *E.coli*, *Salmonella*, and *Listeria* in milk, apple juice, and ground beef respectively. The photograph of the assay showed positive reaction for the 3 bacteria (top). The number of bacteria in each test was estimated and confirmed with cell plating (middle). The graphic shows the ratio of AuNPs aggregation based on absorption measurements at 655 nm (bottom).

needed regardless of the concentration of the analyte. This includes pathogen detection in food safety, toxin detection in biodefense, or early detection of infectious agents and identification of minute amounts of biomarkers at the primary stage of disease development where the concentrations are at the sub-femtomolar ($<10^{-15}$ M) level.(Etzioni et al., 2003; Thaxton et al., 2009) LAPIA concept is applicable for any target analyte as long as its recognition element (antibody, aptamer, complimentary DNA, receptor) is available. The concept can also be adapted to enable quantification by adjusting the number of liposomes used or their cysteine payload.

6. General Conclusions

In conclusion, this research has been successful in achieving the outlined objectives. An international patent (International Patent # PCT/US2016/056850 (Oct 14, 2016)) has been filed for this study. The study has led us to two important findings which have also resulted in two publications and three patent applications.

The first (Chapter 3) described the development of a new method for the synthesis of selenium nanoparticles in a size range of 10nm-1000nm using a sponge as a solid support. In addition, this study also proposed a new approach for long-term storage of nanoparticles on the sponge to prevent aggregation. The nanoparticles can be retrieved when needed by simple washing of the sponge.

The second finding (Chapter 4) describes a way to produce a nanosorbent sponge technology for efficient removal of mercury. The study showed that nanoSe sponge can remove aqueous mercury to undetectable levels even in the presence of high concentrations of other interfering heavy metals and salts as found in industrial wastewater. Furthermore, the study also revealed that selenium nanoparticles are not only grown on the surface of sponge fibers but also inside the fibers. This phenomenon resulted in a remarkable uptake capacity and adsorption kinetic of mercury on the sponge due to bulk diffusion of mercury. Safety evaluation studies also validated the non-hazardous nature and safe disposal of the used sponge after mercury capture.

As a result, this project has opened new perspectives to make sorbents for water and air cleaning in a cost-effective way. Several projects are now initiated based on this work's results, including:

- Application of the proposed concept for mercury removal to the vapor phase. This may also face some potential problems related to high gas temperatures and/or the interference of gas components such as oxides of sulfur and nitrogen (SO_x and NO_x). As an alternative solution, the laboratory is currently working to grow selenium nanomaterials on more thermostable porous materials, including ceramic filters.
- Production of multi-pollutant sponge by using different metal nanoparticle-based sponges such as Nano iron and nanocopper to capture a wide variety of pollutants.

7. Bibliography

- Abbas, A., Kattumenu, R., Tian, L., Singamaneni, S., 2013. Langmuir 29, 56-64.
- Abbas, A., Tian, L., Kattumenu, R., Halim, A., Singamaneni, S., 2012. Chemical Communications 48, 1677-1679.
- Abdelwahed, W., Degobert, G., Stainmesse, S., Fessi, H., 2006. Advanced Drug Delivery Reviews 58, 1688-1713.
- Acres, R.G., Feyer, V., Tsud, N., Carlino, E., Prince, K.C., 2014. The Journal of Physical Chemistry C 118, 10481-10487.
- Adeleye, A.S., Conway, J.R., Garner, K., Huang, Y., Su, Y., Keller, A.A., 2016. Chemical Engineering Journal 286, 640-662.
- Ahmed, S., Bui, M.-P.N., Abbas, A., 2016. Biosensors and Bioelectronics 77, 249-263.
- Aili, D., Mager, M., Roche, D., Stevens, M.M., 2010. Nano Letters 11, 1401-1405.
- Al-Saleh, I., Elkhatib, R., Al-Rouqi, R., Abduljabbar, M., Eltabache, C., Al-Rajudi, T., Nester, M., 2016. International Journal of Hygiene and Environmental Health.
- Alkilany, A.M., Abulateefeh, S.R., Mills, K.K., Bani Yaseen, A.I., Hamaly, M.A., Alkhatib, H.S., Aiedeh, K.M., Stone, J.W., 2014. Langmuir 30, 13799-13808.
- An, S.Y., Bui, M.P., Nam, Y.J., Han, K.N., Li, C.A., Choo, J., Lee, E.K., Katoh, S., Kumada, Y., Seong, G.H., 2009. J Colloid Interface Sci 331, 98-103.
- Anker, J.N., Hall, W.P., Lyandres, O., Shah, N.C., Zhao, J., Van Duyne, R.P., 2008. Nat Mater 7, 442-453.
- Ariga, K., Ishihara, S., Abe, H., Li, M., Hill, J.P., 2012. Journal of Materials Chemistry 22, 2369-2377.
- Atwood, D.A., Zaman, M.K., 2006. Mercury Removal from Water. In: Atwood, D.A. (Ed.), Recent Developments in Mercury Science, pp. 163-182. Springer Berlin Heidelberg, Berlin, Heidelberg.
- Bao, P., Chen, Z., Tai, R.-Z., Shen, H.-M., Martin, F.L., Zhu, Y.-G., 2015. Journal of Proteome Research 14, 1127-1136.
- Bellanger, M., Pichery, C., Aerts, D., Berglund, M., Castaño, A., Čejchanová, M., Crettaz, P., Davidson, F., Esteban, M., Fischer, M.E., Gurzau, A.E., Halzlova, K., Katsonouri, A., Knudsen, L.E., Kolossa-Gehring, M., Koppen, G., Ligocka, D., Miklavčič, A., Reis, M.c., Rudnai, P., Tratnik, J.S., Weihe, P., Budtz-Jørgensen, E., Grandjean, P., 2013. Environmental Health 12, 1-10.
- Bhatnagar, A., Sillanpää, M., 2011. Chemical Engineering Journal 168, 493-504.
- Billinge, S.J.L., McKimmy, E.J., Shatnawi, M., Kim, H., Petkov, V., Wermeille, D., Pinnavaia, T.J., 2005. Journal of the American Chemical Society 127, 8492-8498.
- Bolong, N., Ismail, A.F., Salim, M.R., Matsuura, T., 2009. Desalination 239, 229-246.
- Branco, V., Canário, J., Lu, J., Holmgren, A., Carvalho, C., 2012. Free Radical Biology and Medicine 52, 781-793.
- Braun, T., Farag, A.B., 1978. Analytica Chimica Acta 99, 1-36.
- Bui, M.-P.N., Ahmed, S., Abbas, A., 2015. Nano Letters 15, 6239-6246.
- Byrne, H.E., Mazyck, D.W., 2009. Journal of Hazardous Materials 170, 915-919.

- Chaudhary, S.M., S. K., 2014. Journal of Nanoscience and Nanotechnology 14, 1658-1674.
- Chen, L., Zhang, J., Zhu, Y., Zhang, Y., 2015. RSC Advances 5, 79874-79881.
- Chen, S., Svedendahl, M., Duyne, R.P.V., Käll, M., 2011. Nano Letters 11, 1826-1830.
- Chen, Z., Shen, Y., Xie, A., Zhu, J., Wu, Z., Huang, F., 2009. Crystal Growth & Design 9, 1327-1333.
- Cho, I.-H., Radadia, A.D., Farrokhzad, K., Ximenes, E., Bae, E., Singh, A.K., Oliver, H., Ladisch, M., Bhunia, A., Applegate, B., Mauer, L., Bashir, R., Irudayaraj, J., 2014. Annual Review of Analytical Chemistry 7, 65-88.
- Clarkson, T.W., Vyas, J.B., Ballatori, N., 2007. American Journal of Industrial Medicine 50, 757-764.
- Crini, G., 2005. Progress in Polymer Science 30, 38-70.
- Crump, K.L., Trudeau, V.L., 2009. Environmental Toxicology and Chemistry 28, 895-907.
- de la Rica, R., Stevens, M.M., 2012. Nat Nano 7, 821-824.
- de la Rica, R., Stevens, M.M., 2013. Nat. Protocols 8, 1759-1764.
- Do, D.D., 1998. Adsorption Analysis: Equilibria and Kinetics:(With CD Containing Computer Matlab Programs). World Scientific.
- Dong, H., Quintilla, A., Cemernjak, M., Popescu, R., Gerthsen, D., Ahlswede, E., Feldmann, C., 2014. Journal of Colloid and Interface Science 415, 103-110.
- Dwivedi, S., AlKhedhairy, A.A., Ahamed, M., Musarrat, J., 2013. PLoS ONE 8, e57404.
- Eisenberg, A., 1963. Journal of Polymer Science Part B: Polymer Letters 1, 177-179.
- Enustun, B.V., Turkevich, J., 1963. Journal of the American Chemical Society 85, 3317-3328.
- Esworthy, R.S., Chu, F.F., Doroshow, J.H., 2001. Analysis of Glutathione-Related Enzymes. Current Protocols in Toxicology. John Wiley & Sons, Inc.
- Etzioni, R., Urban, N., Ramsey, S., McIntosh, M., Schwartz, S., Reid, B., Radich, J., Anderson, G., Hartwell, L., 2003. Nat Rev Cancer 3, 243-252.
- Fang, C., Bhattarai, N., Sun, C., Zhang, M., 2009. Small (Weinheim an der Bergstrasse, Germany) 5, 1637-1641.
- Faulconer, E.K., von Reitzenstein, N.V.H., Mazyck, D.W., 2012. Journal of Hazardous Materials 199–200, 9-14.
- Fernandes Azevedo, B., Barros Furieri, L., Peçanha, F.M., Wiggers, G.A., Frizera Vassallo, P., Ronacher Simões, M., Fiorim, J., Rossi de Batista, P., Fioresi, M., Rossoni, L., Stefanon, I., Alonso, M.J., Salaices, M., Valentim Vassallo, D., 2012. Journal of Biomedicine and Biotechnology 2012, 949048.
- Fink, D., 2013. Transport processes in ion-irradiated polymers. Springer Science & Business Media.
- Forootanfar, H., Adeli-Sardou, M., Nikkhoo, M., Mehrabani, M., Amir-Heidari, B., Shahverdi, A.R., Shakibaie, M., 2014. Journal of Trace Elements in Medicine and Biology 28, 75-79.
- Fraser, B., 2016. Nature 534, 162.
- Gandra, N., Abbas, A., Tian, L., Singamaneni, S., 2012. Nano Letters 12, 2645-2651.

- Gardner, R.M., Nyland, J.F., 2016. Immunotoxic Effects of Mercury. In: Esser, C. (Ed.), Environmental Influences on the Immune System, pp. 273-302. Springer Vienna, Vienna.
- Gates, B., Mayers, B., Cattle, B., Xia, Y., 2002. Advanced Functional Materials 12, 219-227.
- Gomes, J.F., Sonnen, A.F., Kronenberger, A., Fritz, J., Coelho, M.A., Fournier, D., Fournier-Noel, C., Mauzac, M., Winterhalter, M., 2006. Langmuir 22, 7755-7759.
- Grabar, K.C., Freeman, R.G., Hommer, M.B., Natan, M.J., 1995. Analytical Chemistry 67, 735-743.
- Grey, D., Garrick, D., Blackmore, D., Kelman, J., Muller, M., Sadoff, C., 2013. Philosophical Transactions of the Royal Society A: Mathematical, Physical and Engineering Sciences 371.
- Griffith, C.S., Luca, V., 2004. Chemistry of Materials 16, 4992-4999.
- Guo, L., Huang, K., Liu, H., 2016. Journal of Nanoparticle Research 18, 1-10.
- Habashi, F., 1978. Environmental Science & Technology 12, 1372-1376.
- Huang, L., Tong, X., Li, Y., Teng, J., Bai, Y., 2015. Journal of Chemical & Engineering Data 60, 151-160.
- Hurt, R.H., Hamburg, S.P., Sarin, L., Kulaots, I., 2013. Nanostructured sorbent materials for capturing environmental mercury vapor. Google Patents.
- Jain, R., Jordan, N., Weiss, S., Foerstendorf, H., Heim, K., Kacker, R., Hübner, R., Kramer, H., van Hullebusch, E.D., Farges, F., Lens, P.N.L., 2015. Environmental Science & Technology 49, 1713-1720.
- Järup, L., 2003. British Medical Bulletin 68, 167-182.
- Jeong, U., Xia, Y., 2005. Advanced Materials 17, 102-106.
- Johnson, N.C., Manchester, S., Sarin, L., Gao, Y., Kulaots, I., Hurt, R.H., 2008. Environmental Science & Technology 42, 5772-5778.
- Jozef M. Pacyna, P.M., Kyrre Sundseth, Elisabeth G. Pacyna, Ermelinda harper, Karin Kindbom, Ingvar Wangberg, Damian Panasuik, 2008.
- Kabiri, S., Tran, D.N.H., Azari, S., Losic, D., 2015. ACS Applied Materials & Interfaces 7, 11815-11823.
- Karatza, D., Lancia, A., Musmarra, D., Zucchini, C., 2000. Experimental Thermal and Fluid Science 21, 150-155.
- Khalid, A., Tran, P.A., Norello, R., Simpson, D.A., O'Connor, A.J., Tomljenovic-Hanic, S., 2016. Nanoscale 8, 3376-3385.
- Khan, M.A.K., Wang, F., 2009. Environmental Toxicology and Chemistry 28, 1567-1577.
- Kosaka, P.M., PiniV, Ruz, J.J., da Silva, R.A., González, M.U., RamosD, CallejaM, TamayoJ, 2014. Nat Nano 9, 1047-1053.
- Kumar, A., Sevonkaev, I., Goia, D.V., 2014. Journal of Colloid and Interface Science 416, 119-123.
- Lamborg, C.H., Hammerschmidt, C.R., Bowman, K.L., Swarr, G.J., Munson, K.M., Ohnemus, D.C., Lam, P.J., Heimburger, L.-E., Rijkenberg, M.J.A., Saito, M.A., 2014. Nature 512, 65-68.
- Lannes, A., Manceau, A., Rovezzi, M., Glatzel, P., Joly, Y., Gautier-Luneau, I., 2016. Dalton Transactions 45, 14035-14038.
- Lata, S., Samadder, S.R., 2016. Journal of Environmental Management 166, 387-406.
- Lee, K., 2012. Nanosorbents and methods of use thereof. Google Patents.

- Lequin, R.M., 2005. Clinical Chemistry 51, 2415-2418.
- Li, B., Zhang, Y., Ma, D., Shi, Z., Ma, S., 2014. Nat Commun 5.
- Lichtenberg, D., Barenholz, Y., 2006. Liposomes: Preparation, Characterization, and Preservation. Methods of Biochemical Analysis, pp. 337-462. John Wiley & Sons, Inc.
- Liu, T., Che, J.-X., Hu, Y.-Z., Dong, X.-W., Liu, X.-Y., Che, C.-M., 2014. Chemistry – A European Journal 20, 14090-14095.
- Lu, C., Chiu, H., Liu, C., 2006. Industrial & Engineering Chemistry Research 45, 2850-2855.
- Lu, C., Liu, C., Rao, G.P., 2008. Journal of Hazardous Materials 151, 239-246.
- Lu, C., Su, F., 2007. Separation and Purification Technology 58, 113-121.
- Luo, C., Xu, Y., Zhu, Y., Liu, Y., Zheng, S., Liu, Y., Langrock, A., Wang, C., 2013. ACS Nano 7, 8003-8010.
- M. Schmidt, W.S.a.K.W.B., 1973. Comprehensive Inorganic Chemistry. The Chemistry of Sulphur, Selenium, Tellurium and Polonium, p. ii. Pergamon.
- Ma, B.-Q., Mulfort, K.L., Hupp, J.T., 2005. Inorganic Chemistry 44, 4912-4914.
- Malhotra, S., Welling, M.N., Mantri, S.B., Desai, K., 2015. Journal of Biomedical Materials Research Part B: Applied Biomaterials, n/a-n/a.
- Martha H., K., illiam H., M., Laurel, D., Rosalina, R., 1997. Mercury study report to Congress. p. 207. United States Environmental Protection Agency.
- Mayers, B.T., Liu, K., Sunderland, D., Xia, Y., 2003. Chemistry of Materials 15, 3852-3858.
- Monson, B., Heiskary, S., 2008. Water Mercury Concentrations in Minnesota Lakes. Minnesota Pollution Control Agency.
- Mukherjee, S., Shang, C., Chen, X., Chang, X., Liu, K., Yu, C., Fang, Y., 2014. Chemical Communications 50, 13940-13943.
- Nam, S., Tratnyek, P.G., 2000. Water Research 34, 1837-1845.
- Ngo, A.T., Karam, P., Fuller, E., Burger, M., Cosa, G., 2008. Journal of the American Chemical Society 130, 457-459.
- Nie, T., Wu, H., Wong, K.-H., Chen, T., 2016. Journal of Materials Chemistry B 4, 2351-2358.
- Oremland, R.S., Herbel, M.J., Blum, J.S., Langley, S., Beveridge, T.J., Ajayan, P.M., Sutto, T., Ellis, A.V., Curran, S., 2004. Applied and Environmental Microbiology 70, 52-60.
- Orth, W.S., Gillham, R.W., 1996. Environmental Science & Technology 30, 66-71.
- Peng, D., Zhang, J., Liu, Q., Taylor, E.W., 2007. Journal of Inorganic Biochemistry 101, 1457-1463.
- Peng, X., Wang, L., Zhang, X., Gao, B., Fu, J., Xiao, S., Huo, K., Chu, P.K., 2015. Journal of Power Sources 288, 214-220.
- Phong, A.T., Neil, O.B.-S., Eric, C.R., Namfon, P., Dhee, P.B., Andrea, J.O.C., 2016. Nanotechnology 27, 045101.
- Pollok, S., Weber, K., Bauer, M., Popp, J., 2015. Modern Techniques for Pathogen Detection. Wiley-VCH Verlag GmbH & Co. KGaA.
- Prasad, K.S., Vaghasiya, J.V., Soni, S.S., Patel, J., Patel, R., Kumari, M., Jasmani, F., Selvaraj, K., 2015. Applied Biochemistry and Biotechnology 177, 1386-1393.
- Qiu, S., Xue, M., Zhu, G., 2014. Chemical Society Reviews 43, 6116-6140.

- Qu, W., Liu, Y., Liu, D., Wang, Z., Jiang, X., 2011. Angewandte Chemie International Edition 50, 3442-3445.
- Ralston, N., 2008a. Nat Nano 3, 648-648.
- Ralston, N., 2008b. Nat Nano 3, 527-528.
- Ramos, J.F., Webster, T.J., 2012. International Journal of Nanomedicine 7, 3907-3914.
- Richard Helmer, I.H., 1997. Water Pollution Control - A Guide to the Use of Water
- Quality Management Principles In: United Nations Environment Programme, W.H.O., Water Supply & Sanitation Collaborative Council (Ed.), p. 526. St Edmundsbury Press, Bury St Edmunds, Suffolk Great Britain
- Rissin, D.M., Kan, C.W., Campbell, T.G., Howes, S.C., Fournier, D.R., Song, L., Piech, T., Patel, P.P., Chang, L., Rivnak, A.J., Ferrell, E.P., Randall, J.D., Provuncher, G.K., Walt, D.R., Duffy, D.C., 2010. Nat. Biotechnol. 28, 595-599.
- Roberts, E.J., Rowland, S.P., 1973. Environmental Science & Technology 7, 552-555.
- Roberts, M.A., Locascio-Brown, L., Maccrehan, W.A., Durst, R.A., 1996. Anal Chem 68, 3434-3440.
- Rossner, A., Snyder, S.A., Knappe, D.R.U., 2009. Water Research 43, 3787-3796.
- Sabın, J., Prieto, G., Ruso, J.M., Hidalgo-Álvarez, R., Sarmiento, F., 2006. Eur. Phys. J. E 20, 401-408.
- Sanchez, F., Sobolev, K., 2010. Construction and Building Materials 24, 2060-2071.
- Saper, J., White, W.E., 1958. Nature 181, 285-286.
- Sawyer, J., 2012. Mercury removal from water. Google Patents.
- Shah, C.P., Kumar, M., Bajaj, P.N., 2007. Nanotechnology 18, 385607.
- Shin, Y., Blackwood, J.M., Bae, I.-T., Arey, B.W., Exarhos, G.J., 2007. Materials Letters 61, 4297-4300.
- Shirsat, S., Kadam, A., Naushad, M., Mane, R.S., 2015. RSC Advances 5, 92799-92811.
- Siantar, D.P., Schreier, C.G., Chou, C.-S., Reinhard, M., 1996. Water Research 30, 2315-2322.
- Snober, A., John, B., Ke, X., Abdennour, A., 2016. Nanotechnology 27, 465601.
- Sohrabi, M.R., 2014. Microchimica Acta 181, 435-444.
- Sonkusre, P., Singh Cameotra, S., 2015. Colloids and Surfaces B: Biointerfaces 136, 1051-1057.
- Stolzoff, M., Webster, T.J., 2016. Journal of Biomedical Materials Research Part A 104, 476-482.
- Stone, M.E., Cohen, M.E., Liang, L., Pang, P., 2003. Dental Materials 19, 675-679.
- Stroyuk, A.L., Raevskaya, A.E., Kuchmiy, S.Y., Dzhagan, V.M., Zahn, D.R.T., Schulze, S., 2008. Colloids and Surfaces A: Physicochemical and Engineering Aspects 320, 169-174.
- Su, C., LaManna, J.A., Gao, Y., Oliver, W.C., Pharr, G.M., 2010. Journal of Materials Research 25, 1015-1019.
- Suh, M.P., Park, H.J., Prasad, T.K., Lim, D.-W., 2012. Chemical Reviews 112, 782-835.

- Sułkowski, W.W., Pentak, D., Nowak, K., Sułkowska, A., 2005. Journal of Molecular Structure 744–747, 737-747.
- Swierczewska, M., Liu, G., Lee, S., Chen, X., 2012. Chemical Society Reviews 41, 2641-2655.
- Tabaei, S.R., Rabe, M., Zetterberg, H., Zhdanov, V.P., Höök, F., 2013. Journal of the American Chemical Society 135, 14151-14158.
- Tansel, B., 2008. Recent Patents on Chemical Engineering 1, 17-26.
- Thaxton, C.S., Elghanian, R., Thomas, A.D., Stoeva, S.I., Lee, J.-S., Smith, N.D., Schaeffer, A.J., Klocker, H., Horninger, W., Bartsch, G., Mirkin, C.A., 2009. Proceedings of the National Academy of Sciences 106, 18437-18442.
- Tonini, D.R., Gauvin, D.A., Soffel, R.W., Freeman, W.P., 2003. Environmental Progress 22, 167-173.
- Tran, P.A., Sarin, L., Hurt, R.H., Webster, T.J., 2009. Journal of Materials Chemistry 19, 2653-2659.
- Tran, P.A., Webster, T.J., 2011. Selenium nanoparticles inhibit Staphylococcus aureus growth. Int J Nanomedicine, pp. 1553-1558.
- Turkevich, J., Stevenson, P.C., Hillier, J., 1951. Discussions of the Faraday Society 11, 55-75.
- UNEP, 2013. UNEP, 2013. Global Mercury Assessment 2013: Sources, Emissions, Releases
- and Environmental Transport. UNEP Chemicals Branch, Geneva, Switzerland. UNEP.
- Veeck, A.C., White, D.J., Whisenhunt, D.W., Xu, J., Gorden, A.E.V., Romanovski, V., Hoffman, D.C., Raymond, K.N., 2004. Solvent Extraction and Ion Exchange 22, 1037-1068.
- Walcarius, A., Delacôte, C., 2005. Analytica Chimica Acta 547, 3-13.
- Walcarius, A., Mercier, L., 2010. Journal of Materials Chemistry 20, 4478-4511.
- Wang, H., Zhang, J., Yu, H., 2007. Free Radical Biology and Medicine 42, 1524-1533.
- Wang, Q., Mejía Jaramillo, A., Pavon, J.J., Webster, T.J., 2015. Journal of Biomedical Materials Research Part B: Applied Biomaterials, n/a-n/a.
- Willets, K.A., Van Duyne, R.P., 2007. Annual Review of Physical Chemistry 58, 267-297.
- Winterhalter, M., Lasic, D.D., 1993. Chemistry and Physics of Lipids 64, 35-43.
- Xiang, N., Zhao, R., Zhong, W., 2009. Cancer Chemotherapy and Pharmacology 63, 351-362.
- Yee, K.-K., Reimer, N., Liu, J., Cheng, S.-Y., Yiu, S.-M., Weber, J., Stock, N., Xu, Z., 2013. Journal of the American Chemical Society 135, 7795-7798.
- Yin, M.C., Faustman, C., 1993. Journal of Agricultural and Food Chemistry 41, 853-857.
- Yu, B., Liu, T., Du, Y., Luo, Z., Zheng, W., Chen, T., 2016a. Colloids and Surfaces B: Biointerfaces 139, 180-189.
- Yu, B., You, P., Song, M., Zhou, Y., Yu, F., Zheng, W., 2016b. New Journal of Chemistry 40, 1118-1123.
- Zeng, H., Uthus, E.O., Combs Jr, G.F., 2005. Journal of Inorganic Biochemistry 99, 1269-1274.
- Zhang, J., Wang, H., Yan, X., Zhang, L., 2005. Life Sciences 76, 1099-1109.
- Zhang, W.-x., 2003. Journal of Nanoparticle Research 5, 323-332.

- Zhang, Y., Wang, J., Zhang, L., 2010. Langmuir 26, 17617-17623.
- Zhong, C., Deng, Z., Wang, R., Bai, Y., 2015. Crystal Growth & Design 15, 1602-1610.